

**STUDY OF UNIAXIAL COMPRESSION PROCESS
FOR AA7075 ALUMINUM ALLOY**

**STUDY OF UNIAXIAL COMPRESSION PROCESS FOR
AA7075 ALUMINUM ALLOY**

By XIAO LIANG, B.Eng, M.Eng.

A Thesis Submitted to the School of Graduate Studies in Partial Fulfillment
of the Requirements for the Degree of Master of Applied Science

McMaster University © Copyright by Xiao Liang, February 2018

MASTER OF APPLIED SCIENCE (2018)

McMaster University

(Mechanical Engineering)

Hamilton, Ontario

TITLE:

STUDY OF UNIAXIAL COMPRESSION
PROCESS FOR AA7075 ALUMINUM ALLOY

AUTHOR:

XIAO LIANG, B.Eng, M.Eng
(Hunan University, China;
McMaster University, Canada)

SUPERVISOR:

Professor Mukesh K. Jain
Department of Mechanical Engineering
McMaster University

NUMBER OF PAGES: xxv, 178

Abstract

An experimental and complementary FE modeling study was conducted to characterize the room and elevated temperature uniaxial compressive deformation behavior of AA7075-T6 and O-temper materials. The experiments consisted of testing cylindrical and cubic specimens prepared from a rolled and heat-treated plate stock of AA7075 alloy. The tests were conducted in the lower range of elevated temperatures up to 300 °C, at several different test speeds in rolling and transverse orientations, as well as under isothermal and non-isothermal test conditions. The test results were analyzed in terms of true stress-strain responses of the two tempers under the above experimental conditions. The deformed test specimens were also observed for surface features and deformed microstructures in the interior of the specimen under the above experimental conditions. A suitable strain rate and temperature dependent constitutive hardening law, in the form of modified Voce-Kocks law, was developed and coded as a UMAT subroutine in ABAQUS FE code to simulate the uniaxial compression experiments and compare the experimental and model results. In general, good general agreement was obtained between experiments and model predictions. A suitable fracture criterion, in the form of Tresca fracture model, was also implemented as a VUMAT subroutine in ABAQUS FE code to simulate the uniaxial compression experiments and predict fracture mode and other characteristics. Once again, good general agreement was obtained between room temperature fracture shapes and model predictions. The experimental and model results collectively provide a broad-based understanding of the effect of temperature, strain rate, material anisotropy, temperature field on material flow

and deformed shapes of cylinders and cubic specimens, the nature of deformation (predominantly shear along two intersecting shear directions) and fracture (predominantly shear). The constraints to deformation at the corners in the cubic specimen yielded rather complex curvature development in deformed cubes. The non-isothermal rapid heating of test specimens using electrical resistance heating and subsequent compression of the specimen provided results similar to the isothermal case. However, the electrical resistance method offers a cost-effective process to form smaller high quality components in forming modes such as hot upsetting.

Acknowledgements

First and foremost, I would like to express my deepest gratitude and respect to my supervisor, Dr. Mukesh K. Jain, a respectable, responsible and resourceful scholar, who has provided me with encouragement, support and valuable guidance through every stage of my master study.

I would also like to thank Dr. Michael Bruhis and Dr. Beth McNally for giving me valuable advice and assistance in conducting various experiment tests.

I would also like to thank several research technicians in machine shop: Mr. Michael Lee, Mr. Ron Lodewyks, Mr. John Colenbrander and Mr. Mark MacKenzie for giving the assistance in various experimental specimen preparations.

I would also like thank Mr. Doug Culley for giving the assistance and guidance in Microstructure observation, etc.

I would also like to thank my colleagues Dr. Zhutian Xu, Dr. Mostafa Atia and Mr. Mehdi Sichani in my lab for their help with experimental work and FE simulation.

Lastly, I forever grateful to my parents their love, support and encouragement and to my friends for their company and for bringing joy and hope in my life over the years.

Table of Contents

Abstract	iv
Acknowledgements	vi
Table of Contents	vii
List of Figures	xiii
List of Tables	xxii
Nomenclature	xxiv
Chapter 1. Introduction	1
1.1. Background	1
1.2. Project objectives	6
1.2.1. Experimentally study of large axisymmetric compressive deformation behavior of AA7075-T6 aluminum alloy under isothermal conditions	6
1.2.2. Assessment of material constitutive models for strain rate and temperature dependent plastic deformation of AA7075-T6 alloy in uniaxial compression.....	7
1.2.3. Numerical study of plastic deformation behavior of AA7075-T6 alloy in uniaxial compression (i.e., simple upsetting)	7
1.2.4. Experimental study of AA7075 aluminum in simple uniaxial compression under non-isothermal conditions	8
1.3. Thesis structure	8
Chapter 2. Literature Review	10
2.1. Experimental aspects of simple upsetting process	10

2.1.1. Stress and strain states and strain paths in simple upsetting.....	10
2.1.2. Typical deformation stages in uniaxial compression of cylindrical specimens	13
2.1.3. Process parameters in simple upsetting	14
2.1.3.1. Specimen geometry.....	15
2.1.3.2. Strain rate (or test speed)	17
2.1.3.3. Test temperature.....	18
2.1.4. Other factors affecting uniaxial compression behavior of aluminum alloys....	19
2.1.5. A summary of studies on AA7075, and another common alloy AA2024 at elevated temperatures using uniaxial compression tests	21
2.1.5.1. AA7075 aluminum alloy composition and processing.....	21
2.1.5.2. AA7075 alloy temper states.....	21
2.1.5.3. AA7075 strain hardening characteristics	23
2.1.5.4. Strain rate sensitivity.....	24
2.1.6. Microstructure and texture evolution during elevated temperature uniaxial compressive deformation of 7xxx aluminum alloys.....	27
2.1.6.1. Grain size evolution	27
2.1.6.2. Texture evolution	29
2.1.7. Fracture characteristics during elevated temperature simple upsetting of 7xxx aluminum alloys	31

2.2. Strain rate and temperature dependent constitutive material models of plastic deformation of 7xxx series aluminum alloys.....	34
2.3. Analytical modeling.....	38
2.4. Finite element modeling of uniaxial hot compression test	42
2.5. Non-isothermal hot compression studies on AA7xxx alloys.....	43
2.6. Hot compression studies on non-cylindrical shapes of work piece	45
2.7. Summary	46
Chapter 3. Experimental Methodology.....	48
3.1. Introduction.....	48
3.2. Test materials	49
3.3. Machining of test cylindrical specimens.....	49
3.4. Heat treatment of test specimens	52
3.5. Isothermal uniaxial compression tests	53
3.5.1. Mechanical test system.....	53
3.5.2. Test parameters.....	55
3.5.3. Test procedure	56
3.5.3.1 Installation of compression platen and centering of the specimen	56
3.5.3.2. Computer set-up, control and data acquisition.....	56
3.5.3.3. Heating of the environmental chamber and sample testing	58

3.5.3.4. Data analysis	59
3.6. Non-isothermal uniaxial compression tests	60
3.6.1. Test system	61
3.6.2. Test parameters	63
3.6.3. Test procedure	64
3.6.3.1. Installation of the test specimen in the test jig	64
3.6.3.2. Heating system set-up	64
3.6.3.3. Mechanical testing conditions	65
3.6.3.4. Temperature measurement experiments	66
3.7. Optical metallography of test specimens	67
Chapter 4. FE Simulation Methodology for Isothermal Uniaxial Compression Tests	70
4.1. Introduction	70
4.2. Material modeling	72
4.2.1. Yield criterion	72
4.2.2. Constitutive hardening law	74
4.2.3. Ductile fracture models	81
4.2.3.1. GTN ductile damage model	81
4.2.3.2. Tresca fracture model	82
4.3. Analysis type	83
4.4. FE model geometry	85

4.5. Contact definition.....	86
4.6. Model boundary conditions	88
4.7. Meshing.....	89
4.8. Summary	92
Chapter 5. Results and Discussion.....	93
5.1. Isothermal uniaxial compression experiments.....	93
5.1.1. Effect of temperature	94
5.1.2. Effect of speed	97
5.1.3. Effect of orientation.....	99
5.1.4. Effect of temper	101
5.1.5. Effect of test specimen geometry	102
5.1.6. Pattern of flowlines and barrelling characteristics of test specimens	105
5.2. Non-isothermal test results	113
5.2.1. Temperature versus time curves	113
5.2.2. Effect of test speed	115
5.2.3. Effect of applied current	117
5.2.4. Effect of specimen geometry	118
5.2.5. Pattern of flowlines, barrelling and fracture characteristics of non-isothermal test specimens	119
5.3. Microstructures of deformed isothermal and non-isothermal compression test specimens	124

5.3.1. Effect of temperature	125
5.3.2. Effect of speed	127
5.3.3. Effect of specimen orientation.....	130
5.3.4. Effect of temper	131
5.3.5. Effect of test specimen geometry	134
5.4. Results from FE simulations of uniaxial compression experiments	135
5.4.1. Assessment of constitutive material hardening laws for uniaxial compression of AA7075-T6 alloy	137
5.4.1.1. Johnson-Cook model	137
5.4.1.2. Arrhenius model.....	139
5.4.1.3. Modified V-K model.....	144
5.4.2. Material anisotropy	156
5.4.3. Modeling of ductile fracture	158
5.4.3.1. GTN ductile damage model	159
5.4.3.2 Tresca fracture model.....	161
5.5. Summary	163
Chapter 6. Conclusions	166
Chapter 7. Suggestions for Future Work	171
References.....	174

List of Figures

Figure 1.1. A simple representation of isothermal uniaxial compression test before and after compression (Wang et al., 2017)	3
Figure 1.2. True stress-true strain curves of AA7075-T6 at 220 °C at different strain rates	4
Figure 1.3. True stress-true strain curves of AA7075 at several elevated temperatures.....	4
Figure 2.1. The procedure in the cylindrical compression test.	11
Figure 2.2. Reference axes for an element at the equatorial free-surface of a barrelled compression specimen	11
Figure 2.3. Relationship between the principle strains at the equatorial surface of compression specimens with (a) unlubricated (b) lubricated platens	12
Figure 2.4. Axisymmetric compressive plastic deformation process of simple upsetting of cylinders	14
Figure 2.5. The cylindrical specimen geometry of various ratio of diameter and initial height.....	16
Figure 2.6. Geometry and fracture phenomena in the flanged upsetting.....	16
Figure 2.7. Geometry and fracture phenomena in the tapered upsetting	17
Figure 2.8. True stress and true strain curves of 2124-T851 Al at 380 °C in different strain rate.....	18

Figure 2.9. True stress-true strain curves of AA7075 at several elevated temperatures (Strain rate is 0.078 s^{-1}).....	19
Figure 2.10 Temperature-time history of above tempers.....	22
Figure 2.11 Strain rate sensitivity parameter (m) plotted as function of temperature for AA7075 alloy (Jenab and Taheri 2014).....	25
Figure 2.12. Strain rate sensitivity parameter (m) plotted as function of temperature for AA7075-T6 alloy	26
Figure 2.13. The process of dynamic recrystallization during hot compression of aluminum alloys	29
Figure 2.14. Stress-strain shapes for AA7075 alloy.	36
Figure 2.15. The geometrical details of the analytical model.....	39
Figure 2.16. Calculated strain paths and comparison with the experimental (the line represent calculation data and the circle represent experimental data).....	41
Figure 2.17. Flow stress of 7150 aluminum alloy during non-isothermal hot compression with the temperature decreasing from $425 \text{ }^\circ\text{C}$ to $325 \text{ }^\circ\text{C}$ with interval of 10 s : (a) $\dot{\epsilon} = 0.01 \text{ s}^{-1}$, (b) $\dot{\epsilon} = 0.1 \text{ s}^{-1}$, (c) $\dot{\epsilon} = 1 \text{ s}^{-1}$ and (d) comparison among non-isothermal stresses with isothermal continuous and multistage stresses.	44
Figure 2.18. True stress and strain response of AA5182-O at strain rate (a) 1 s^{-1} , (b) 10^{-2} s^{-1} and (c) 10^{-4} s^{-1} along rolling direction	45
Figure 3.1. A schematic of RD and TD specimens machined from the plate.....	50

Figure 3.2. Cutting and machining of AA7075-T6 plate stock into cylinders for obtaining cylindrical test specimens.	51
Figure 3.3. The aluminum plate stock after removal of the cubic specimens and the cubic specimens.	52
Figure 3.4. The side and top views for the cubic sample holder for polishing.	52
Figure 3.5. The furnace for heat treatment.	53
Figure 3.6. MTS servo-hydraulic mechanical test system for hot uniaxial compression experiments. Image on the right shows the inside view of the environmental chamber with upper and lower loading arms. A cylindrical test specimen is also shown above the bottom compression platen.	54
Figure 3.7. Two different views of the fixtures for centering of the cylindrical and cubic specimens on the bottom compression platen.	55
Figure 3.8 Front view and side view of the electrical resistance heating system.	61
Figure 3.9. Mechanical test system.	62
Figure 3.10. Applied current versus time profiles prior to compression testing.	65
Figure 3.11. The specimen with the thermocouple as installed on the test system.	67
Figure 3.12. The cross-sections of the specimens.	68
Figure 4.1. One quarter models of, (a) cylindrical, and (b) cubic, specimens.	85
Figure 4.2. The contact surfaces of cylindrical specimen.	86

Figure 4.3. Cylindrical specimen geometry, (a) before compression, and (b) after compression.	87
Figure 4.4. Sketches illustrating the different boundary conditions for the FE model of uniaxial compression of a cylindrical specimen.	88
Figure 4.5. Model load-displacement curve from different number of elements, (a) complete curves, (b) partial curves in the 3.8 mm - 4 mm displacement range.	90
Figure 4.6. 3D solid element C3D8 and 2D element R3D4 shapes in ABAQUS FE code.	91
Figure 4.7. Mesh densities of the cylindrical specimen and rigid platen surface.	91
Figure 5.1. Effect of temperature on true stress versus true strain curves	95
Figure 5.2. Effect of temperature on true stress versus true strain curves	95
Figure 5.3. Effect of temperature on true stress versus true strain curves	96
Figure 5.4. Effect of test speed on true stress versus true strain curves.....	98
Figure 5.5. Effect of test speed on true stress versus true strain curves.....	98
Figure 5.6. Effect of test speed on true stress versus true strain curves.....	99
Figure 5.7. Effect of orientation on true stress versus true strain curves.....	100
Figure 5.8. Effect of temper on true stress versus true strain curves. (a) 25 °C, (b) 100 °C, (c) 200 °C and (d) 300 °C	102

Figure 5.9. Effect of geometry on true stress versus true strain curves. (a) 25 °C, (b) 100 °C, (c) 200 °C and (d) 300 °C	104
Figure 5.10. Effect of specimen geometry on true stress versus true strain curves. (a) 25 °C, (b) 100 °C, (c) 200 °C and (d) 300 °C	105
Figure 5.11. Deformed cylindrical specimens after isothermal compression tests at 4 different temperature, (a)RT, (b) 100 °C (c) 200 °C and (d) 300 °C.....	107
Figure 5.12. Deformed cylindrical specimens after isothermal compression tests for 4 different temperature, (a) RT, (b) 100 °C (c) 200 °C and (d) 300 °C.....	108
Figure 5.13. Deformed cylindrical specimens after isothermal compression tests for 4 different temperature, (a) RT, (b) 100 °C (c) 200 °C and (d) 300 °C.....	109
Figure 5.14. Deformed cubic specimens after isothermal compression tests for 4 different temperature, (a) RT, (b) 100 °C (c) 200 °C and (d) 300 °C.....	111
Figure 5.15. Deformed cubic specimens after isothermal compression tests for 4 different temperature, (a) RT, (b) 100 °C (c) 200 °C and (d) 300 °C.....	112
Figure 5.16. Temperature versus time for different applied currents.	114
Figure 5.17. Effect of test speed on true stress versus true strain curves, (a) 5 kA, (b) 7.5 kA and (c) 10 kA.....	116
Figure 5.18. Effect of applied current on true stress and true strain curves; (a) 3 mm/s, (b) 5 mm/s and (c) 10 mm/s.....	117

Figure 5.19. Effect of geometry on true stress and true strain curve (a) 3 mm/s, (b) 5 mm/s and (c) 10 mm/s	119
Figure 5.20. Deformed cylindrical specimens after non-isothermal compression tests for 3 different applied currents, (a) 5 kA, (b) 7.5 kA and (c) 10 kA.	121
Figure 5.21. Deformed cubic specimens after non-isothermal compression tests for 3 different applied currents, (a) 5 kA, (b) 7.5 kA and (c) 10 kA.	122
Figure 5.22. Top and side views of cylinder after compression test (a) 5 kA at 3 mm/s, 5 mm/s and 10 mm/s, (b) 7.5 kA at 3 mm/s, 5 mm/s and 10 mm/s and (c) 10 kA at 3 mm/s, 5 mm/s and 10 mm/s.	123
Figure 5.23. Top view and side view of cube after compression test (a) 5 kA at 3 mm/s, 5 mm/s and 10 mm/s, (b) 7.5 kA at 3 mm/s, 5 mm/s and 10 mm/s and (c) 10 kA at 3 mm/s, 5 mm/s and 10 mm/s.	124
Figure 5.24. A schematic illustration of where in the vertical plane the micrographs have come from in Figure 5.25-5.28.	125
Figure 5.25. Optical micrographs of deformed cylindrical specimens tested at different temperatures	127
Figure 5.26. Optical micrographs from cylindrical specimens tested at 3 different speeds	129
Figure 5.27. Optical micrographs from TD cylindrical specimens tested at RT and 300 °C	131

Figure 5.28. The microstructures of O temper cylindrical specimens	132
Figure 5.29. Three views of the vertical plane at three different compression distances; (a) 1.09 mm, (b), 2.18 mm and (c) 4.36 mm for a specimen tested at 0.005 inch/s (0.127 mm/s) and RT.....	133
Figure 5.30. Three views of the vertical plane at three different compression distances; (a) 1.88 mm, (b), 3.76 mm and (c) 7.52 mm for a specimen tested at 0.005 inch/s (0.127 mm/s) and 300 °C.....	133
Figure 5.31. Microstructures of deformed cubic specimens tested at room temperature and 300 °C	135
Figure 5.32. Comparisons of predicted true stress-strain curves from FE simulation of uniaxial compression tests using Johnson-Cook model and experimentally obtained curves, (a) room temperature, (b) 100 °C, (c) 200 °C and (d) 300 °C	139
Figure 5.33. Comparison of predicted true stress-strain curves from FE simulation of uniaxial compression tests using Arrhenius model and experimentally obtained curves from case (i) fit parameters; (a) room temperature, (b) 100 °C, (c) 200 °C and (d) 300 °C	142
Figure 5.34. Comparison of predicted true stress-strain curves from FE simulation of uniaxial compression tests using Arrhenius model and experimentally obtained curves, case (ii) (a) 200 °C and (b) 300 °C	142

Figure 5.35. Comparison of predicted true stress-strain curves from FE simulation of uniaxial compression tests using modified V-K model and experimentally obtained curves, (a) RT, (b) 100 °C, (c) 200 °C and (d) 300 °C.....	145
Figure 5.36. Top, side and isometric views of compressed cylindrical and cubic specimens	147
Figure 5.37. The Mises stress and equivalent plastic strain contours at various compression distances for cylindrical specimens in side view	149
Figure 5.38. The Mises stress and equivalent plastic strain contours at various compression distances for cubic specimens	150
Figure 5.39. Shear stress and shear strain contours at various compression distances for cylindrical specimens.....	152
Figure 5.40. Shear stress and shear strain contours at various compression distances for cubic	153
Figure 5.41. FE model geometry (1/4 th model) of cylindrical specimen with specific points of interest for strain path determination.....	154
Figure 5.42. FE model geometry (1/4 th model) of cubic specimen with specific points of interest for strain path determination.	154
Figure 5.43. The strain paths of elements located at center (A), mid-surface (B) and top edge (C) of a cylindrical specimen.	155

Figure 5.44. The strain paths of elements located at center (A), mid-surface (B₁ and B₂) and corner (C₁ and C₂) of a cubic specimen. 155

Figure 5.45. A view of the top surface of a deformed cylindrical specimen from simulation (left) and experiments (right) corresponding to the specimen height of 12 mm..... 157

Figure 5.46. Deformed cubic specimen from simulation and experiment corresponding to a specimen height of 7 mm, (a) top view, and (b) side view 158

Figure 5.47. Prediction of fracture from GTN damage model for a cylindrical specimen uniaxially compressed at room temperature. 161

Figure 5.48. The slant failure of a T6 temper cylindrical specimen tested at room temperature. 161

Figure 5.49. Side and isometric views of a 1/8th geometry compressed cylindrical test specimen showing deleted elements along an inclined shear plane from FE simulations with Tresca fracture criterion. 162

List of Tables

Table 2.1. Recent studies on uniaxial compression tests on precipitation-hardenable aluminum alloys from literature.....	20
Table 2.2 Material properties in different tempers of AA7075 aluminum alloy	23
Table 2.3. Grain characteristics of high strength 7xxx aluminum alloys subjected to hot compression tests.	28
Table 2.4. Crystallographic textures from EBSD experiments on hot compressed test samples of 7xxx series aluminum alloys.	30
Table 2.5. Fracture characteristics of 7xxx series aluminum alloys under hot uniaxial compression.	33
Table 2.6. The Constitutive material models of plastic deformation of AA7075 aluminum alloy.....	37
Table 2.7. Different types of FE modeling of hot compression test.	42
Table 3.1. Chemical composition of AA7075 aluminum sheet (wt %).	49
Table 3.2. Test parameters for isothermal compression tests.	55
Table 3.3. Test parameters for interrupted tests.....	56
Table 3.4. Hot compression test parameters.	57
Table 3.5. Strain rates and test times for different tempers and specimen types.	58
Table 3.6. Test parameters for non-isothermal compression tests.....	63

Table 4.1. FE test simulation matrix.	71
Table 4.2. Elastic properties and density of AA7075 alloy used in the FE model.	72
Table 4.3 (a). Values of R-values and F, G, H, L, M, N material constants.....	74
Table 4.3 (b). Values of F, G, H, L, M, N material constants.	74
Table 4.4. Constitutive material parameters for J-C model	75
Table 4.5. Nomenclature of symbols in the modified V-K constitutive equations.....	76
Table 4.6. Nomenclature of symbols in the modified V-K constitutive equations.....	77
Table 4.7. Input variables in UMAT subroutine (a) Arrhenius equation model (b) Modified V-K model	79
Table 4.8. State variables in VUMAT subroutine (a) Arrhenius equation model (b) Modified V-K model.....	80
Table 4.9 Parameters of GTN damage model for AA7075 alloy	82
Table 4.10. Input variables in VUMAT subroutine for Tresca fracture criterion.....	83
Table 4.11. State variables in VUMAT subroutine for Tresca fracture criterion.	83
Table 4.12. ABAQUS FE code selection.....	84
Table 5.1. Constitutive material parameters for J-C material model.....	138
Table 5.2. The material parameters for the modified V-K model.....	144
Table 5.3. Parameters of GTN damage model for AA7075 alloy	159

Nomenclature

A	Area
A, B, C, n and m	Parameters in Johnson-Cook model
a	Length of cubic specimen
C_1 and C_2	Parameters in modified V-K model
D_0	Initial diameter
d_{\max}	Maximum diameter after compression
d_{\min}	Minimum diameter after compression
f^*	Total effective void volume fraction
f_c	Critical void volume fraction at the onset of void coalescence
f_f	Void volume fraction at final fracture
f_n	Void volume fraction of void nucleating particles
F, G, H, L, M and N	Hill's anisotropic parameters
H_0	Initial height
h	Height after compression
K	Strength coefficient
k	Boltzmann constant
$\ln A$, Q , n and α	Material parameters for Arrhenius equation model
m	Strain rate sensitivity
n	Strain hardening exponent
P	Load
q_1, q_2, q_3	Calibration coefficients for GTN model
$R_0, R_{45^\circ}, R_{90}$	Anisotropy values along sheet orientation of 0° , 45° and 90°
s	Compression distance
s_n	Standard deviation
T	Temperature
T_{melt}	Melting temperature
T_{room}	Room temperature

v	Test speed
ε	Strain
$\dot{\varepsilon}$	Strain rate
$\dot{\varepsilon}_0$	Reference strain rate
$\dot{\varepsilon}_{k_0}$	Initial reference strain rate at 0 °K
$\dot{\varepsilon}_{s_0}$	Saturation reference strain rate at 0 °K
ε_p	Plastic strain
ε_E	Engineering strain
ε_n	Mean nucleating strain
ε_r	Strain in the r-direction
ε_T	True strain
ε_z	Strain in the z-direction
ε_θ	Strain in the θ -direction
θ	Work hardening rate
σ	Flow stress
σ_0	Initial yield stress
$\sigma_{11}, \sigma_{22}, \sigma_{33}$	Normal stress components
$\sigma_{12}, \sigma_{13}, \sigma_{23}$	Shear stress components
σ_{k_0}	Initial threshold stress at 0 °K
σ_s	Saturation stress
σ_{s_0}	Saturation threshold stress at 0 °K
σ_E	Engineering stress
σ_T	True stress
σ_h	Hypostatic stress,
$\Delta\bar{\varepsilon}^p$	Increment of equivalent plastic strain
μ	Friction coefficient

Chapter 1. Introduction

1.1. Background

Aluminum is a lightweight material compared to steel with a density of about one third of steel. This attribute along with its superior corrosion resistance and higher recyclability has led to its competitive advantage in many cases and its increasing use in many formed engineered components. The forming process itself is often carried out at room temperature where low strength aluminum alloys of higher ductility are generally utilized. In order to form higher strength aluminum alloys of lower room temperature ductility, elevated temperatures are necessary. This has led to the development of elevated temperature bulk forming process such as hot upsetting, hot forging, hot extrusion as well as warm/hot sheet forming processes. The plastic deformation behavior and ductility in general of most wrought metallic materials tends to be highly strain rate and temperature dependent at elevated temperatures. This arises from thermally activated nature of plastic deformation mechanisms in metallic materials such as activation of additional slip systems for dislocation motion and enhanced diffusional creep of materials.

Many studies exist in the literature that investigate the nature of plastic flow in aluminum alloys at various strain rates and temperatures. In recent years, there has been increased interest in understanding the strain rate and temperature dependent plastic deformation behavior of high strength 7xxx series aluminum alloys. A commonly used aerospace high strength wrought aluminum alloy from 7xxx series, AA7075, in peak aged T6 temper condition, is of special interest as it offers the promise of further weight reduction for

automotive and aerospace components compared to the lower strength aluminum alloys from 2xxx, 5xxx, and 6xxx series due to its extraordinary strength. The AA7075-T6 alloy, as other aluminum alloys, shows a strain rate and temperature dependent plastic deformation behavior that has been studied in the literature in recent years. A simple sketch of specimen deformation under isothermal uniaxial compression test is shown in Figure 1.1. These studies are often conducted under isothermal test conditions in the laboratory where it is easier to obtain a true stress versus true strain response of the material in uniaxial compression and uniaxial tension at different strain rates and temperatures (see Figures 1.2 and Figure 1.3). Such stress-strain response is then represented by existing or new constitutive material models (hardening laws) which are then utilized within the finite element method to simulate and analyze lab-based forming experiments as well as more complex forming processes of industrial relevance. The quality of predictions from the FE model are sensitive to the material model employed and other process parameters such as tool-work piece friction at elevated temperatures. A suitable model for strain rate and temperature dependent plastic deformation of AA7075-T6 alloy in bulk forming is still lacking. While many constitutive laws have been proposed to represent such deformation conditions, a closer investigation often reveals their limited applicability in terms of interpolation and extrapolation of stress-strain curves outside of the range of experimental data. This is often because material-specific deformation mechanisms of temperature-dependent strain and strain rate hardening are poorly captured by the proposed material models. Also, there is a lack of complementary studies of flow localization and fracture at the microstructural level for AA7075-T6 alloy in uniaxial compression. Also, most studies

have been conducted using cylindrical specimen in compression where the stress state is largely uniaxial and under isothermal conditions. There is very limited data on compression of cubic specimens where the material flow is more complex and uniaxial compression stress state cannot be assumed. Further, since isothermal condition is often hard to achieve in real forming operations, and especially under rapid heating conditions, it would be useful to observe the deformation behavior of material under transient temperature conditions.

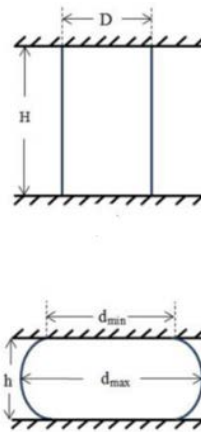


Figure 1.1. A simple representation of isothermal uniaxial compression test before and after compression (Wang et al., 2017).

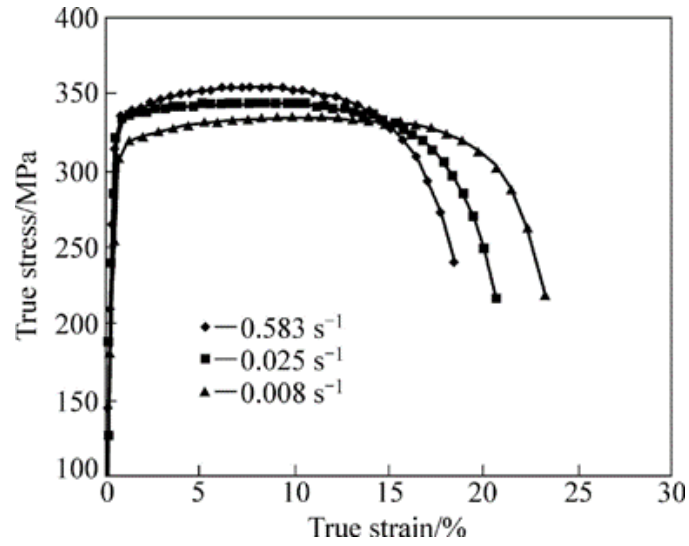


Figure 1.2. True stress-true strain curves of AA7075-T6 at 220 °C at different strain rates (Wang et al.,2012).

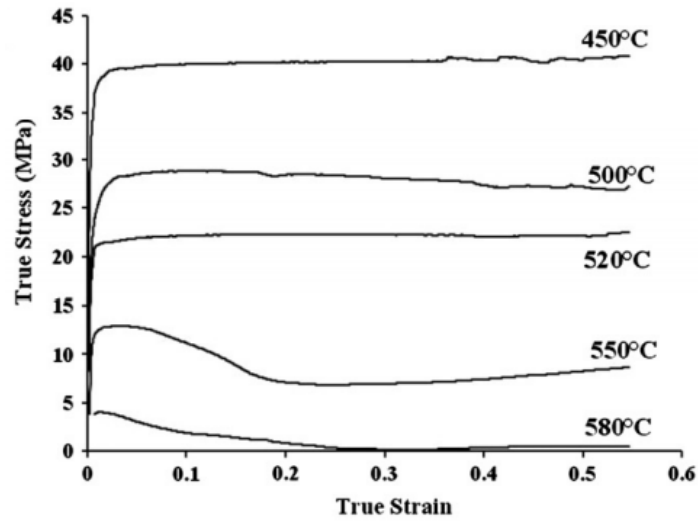


Figure 1.3. True stress-true strain curves of AA7075 at several elevated temperatures (tests conducted at a strain rate of 0.004s⁻¹) (Rokni et al., 2011).

The research presented in this thesis focuses on uniaxial compression experiments on AA7075-T6 cylindrical and cubic specimens at a range of test speeds and isothermal temperatures as well as under transient temperature conditions. Also, the deformed test samples are analyzed for understanding of the underlying microstructural changes at the grain scale, plastic flow localization, and fracture that occur during uniaxial compression of cylindrical and cubic specimens. Further, the uniaxial compressive behavior from the cylindrical test specimens in the form of true stress – strain curves at different initial test speeds and isothermal temperatures are utilized to assess two existing and a new constitutive material model for AA7075-T6 sheet. The latter is then utilized within a general purpose commercial finite element code to simulate the plastic deformation of cylindrical and cubic compression experiments. The experimental and simulation results are compared to assess the validity of the material model and to verify the prediction from the FE model. Furthermore, verified FE model is used in a parametric study to look at the effect of material and process parameters on deformed shape, material flow, strain distribution within the work piece, and aspects of plastic strain localization and fracture. Lastly, simple uniaxial compression experiments under non-isothermal conditions are carried out using a novel method of rapid electrical resistance heating of the specimens with a pulse of large current over a short period of time prior to testing. As above, the macroscopic true stress-strain response of the test specimen as well as resulting microstructural changes within the specimen are studied.

1.2. Project objectives

1.2.1. Experimentally study of large axisymmetric compressive deformation behavior of AA7075-T6 aluminum alloy under isothermal conditions

Following experimental aspects of the deformation and damage behavior of AA7075 aluminum are studied

- Effect of elevated temperature on uniaxial compressive stress-strain response in the axisymmetric upsetting test.
- Effect of test speed in axisymmetric upsetting test at each of the elevated temperatures above.
- Examination of the deformation process by carrying out interrupt tests to different deformable levels.
- Examine the effect of the specimen geometry, cylindrical and cubic, temper and orientation on uniaxial compressive deformation process.
- Study of deformed microstructures and damage within the deformed specimens.

1.2.2. Assessment of material constitutive models for strain rate and temperature dependent plastic deformation of AA7075-T6 alloy in uniaxial compression

- A recent constitutive material model of Nasr et al. (Naser et al., 2014), referred to as Arrhenius model in the thesis, for strain rate and temperature dependent plastic deformation of AA7075-T6 alloy in uniaxial compression is analyzed for its applicability to the above lab-based experiments.
- A commonly used constitutive material model of Johnson-Cook is also assessed for its applicability to the above lab-based experiments.
- A new constitutive hardening law, a modification of Voce-Kocks law, recently proposed by Xu et al., is also assessed for its applicability to the above lab-based experiments.

1.2.3. Numerical study of plastic deformation behavior of AA7075-T6 alloy in uniaxial compression (i.e., simple upsetting)

- Validation of the FE model of axisymmetric uniaxial compression tests with the experiments.

- Utilization of the FE model to simulate the experimental upsetting process for cylindrical and cubic specimens towards a better understanding of material flow, and stress and strain development in critical regions of upset parts.

1.2.4. Experimental study of AA7075 aluminum in simple uniaxial compression under non-isothermal conditions

Following aspects of the deformation and damage behavior of AA7075 aluminum are studied under non-isothermal deformation conditions:

- Study the effect of applied current in a rapid resistance heating uniaxial compression test.
- Study the true stress-strain response of the material under transient temperature conditions.
- Study the effect of initial strain rate (or test speed) and geometry on hot compressive deformation behavior under transient temperature conditions of resistance heating.

1.3. Thesis structure

This thesis consists of 7 chapters. This first chapter provides a background and motivation for the study of axisymmetric uniaxial compression process for AA7075-T6 and AA7075-O alloys and the specific objectives of the research. A review of previous work on

axisymmetric upsetting process is presented in Chapter 2. This review includes experimental work on axisymmetric upsetting of AA7075-T6 alloy as well as strain rate and temperature dependent constitutive material models for deformation of AA7075 alloy. The experimental methodologies for conducting isothermal and non-isothermal uniaxial compression tests are presented in Chapters 3. The FE simulation methodology including the constitutive material models utilized with the FE simulations are covered in Chapter 4. The related results of experiments and simulations are also compared to validate the FE model in Chapters 5. This chapter also includes the results of a parametric study of the effect of material and process parameters on deformation behavior of AA7075-T6 alloy in simple isothermal and non-isothermal uniaxial compression of cylinders and cubes. The conclusions arising from present work and suggestions for future work are provided in Chapters 6 and 7 respectively. A list of references is provided at the end of the thesis.

Chapter 2. Literature Review

This chapter provides a review of the previous experimental and numerical modeling studies pertaining to uniaxial hot compression (and very briefly simple upsetting) of aluminum alloys with emphasis on 7xxx aluminum alloys. The chapter is divided into several sections and each section is further divided into sub-sections to cover the effects of process and material parameters on flow and fracture characteristics of 7xxx aluminum alloys in uniaxial hot compression test conditions.

2.1. Experimental aspects of simple upsetting process

2.1.1. Stress and strain states and strain paths in simple upsetting

Uniaxial compression test is a common test utilized to assess material behavior in the upsetting process. Uniaxial cylindrical compression test involves placement of a cylinder between two platens which are attached to the loading arms of a mechanical test system. Typically, one of the loading arms with the attached platen is kept fixed while the other arm and the platen is moved in such a way as to reduce the distance between the two platens (see Figure 2.1). Consequently, the cylindrical specimen deforms under uniaxial compression. However, the stress state is one of axial compression, radial expansion as well as circumferential (or hoop tension) as depicted in Figure 2.2. The strain path in the left quadrant can be varied by changing the aspect ratio (i.e., ratio of initial height H_0 to initial diameter D_0 of the cylinder) as long as this ratio is below unity and by varying the lubrication condition between the cylinder top (and bottom) surfaces and the two platens,

as shown in Figure 2.3. As shown, when the aspect ratio is increased, ϵ_z and ϵ_r are increased. Also, by comparing curves from lubricated and unlubricated platen cases, the effect of aspect ratio is reduced for the lubricated case.

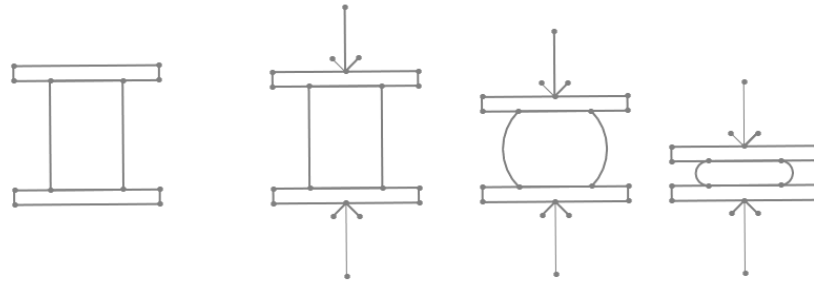


Figure 2.1. The procedure in the cylindrical compression test.

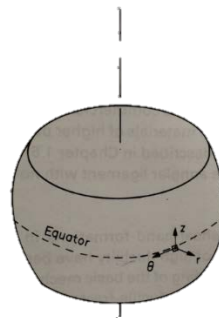
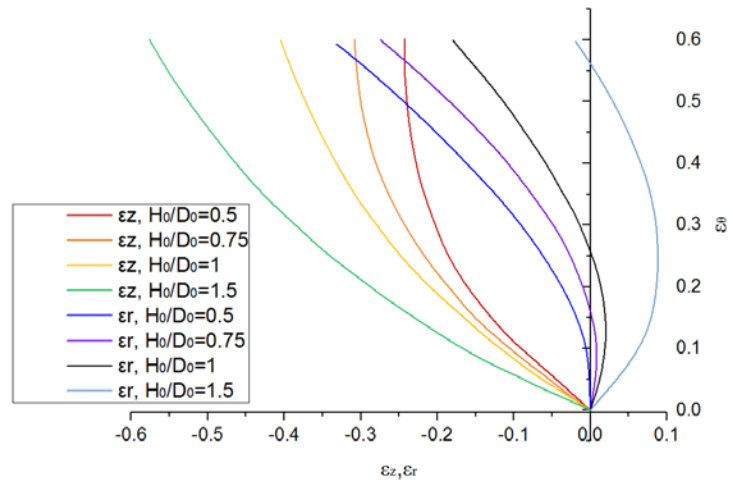
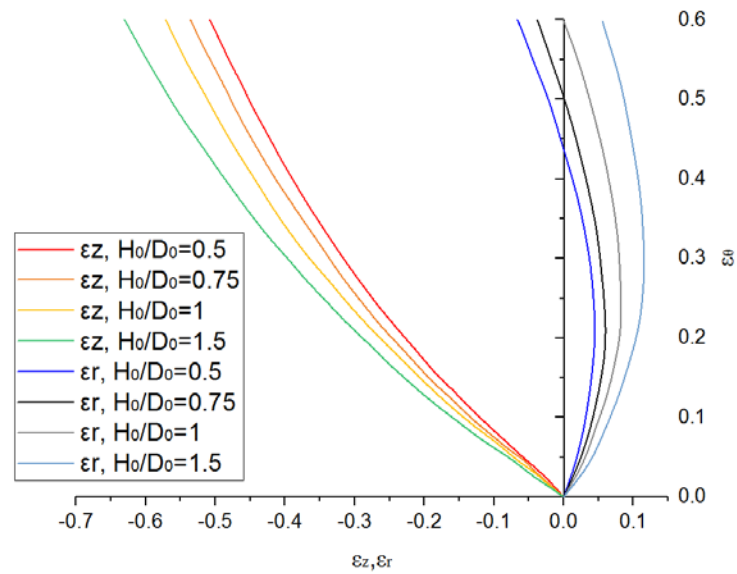


Figure 2.2. Reference axes for an element at the equatorial free-surface of a barrelled compression specimen (Thomason, 1990).



(a) Unlubricated platen



(b) Lubricated platen

Figure 2.3. Relationship between the principle strains at the equatorial surface of compression specimens with (a) unlubricated (b) lubricated platens (Thomason, 1990).

2.1.2. Typical deformation stages in uniaxial compression of cylindrical specimens

Simple upsetting process can be described in three stages, (i) uniform elastic deformation of the test specimen up to the yield point, (ii) uniform plastic deformation, and (iii) non-uniform large plastic deformation of the test specimen due to presence of friction at the specimen-compression platen interface. The last stage leads to barreling of the outer surface of the specimen. Barrelling can lead to the development of tensile mean (or hydrostatic) stresses in the outer barrelled region of compression specimens. These values are highest in magnitude at the equatorial free surfaces. In the last stage, crack initiate and grow, and often from the equatorial surface into the fracture, as reported in the literature. The fracture surfaces are typically inclined to the loading axis. They can be planar or curved. The initiation of surface micro-cracks can lead to a gradual reduction in load and subsequently more catastrophic drop in load as the micro-cracks link to form a macro-crack, and eventually physical separation of the material occurs. Figure 2.3 earlier showed the strain paths at the equatorial free surface of the uniaxial compression specimens in terms of both $d\varepsilon_z / d\varepsilon_\theta$ and $d\varepsilon_r / d\varepsilon_\theta$ ratios.

Figure 2.4 shows a schematic of the compressive load (or compressive axial stress) versus compressive displacement (or compressive axial strain) response of a cylindrical specimen along with the evolving shape of the cylindrical specimen at different amounts of axial strains. As shown, the curve continues to rise until the onset of fracture (last point on the curve) at room temperature, unlike in the case of uniaxial tensile tests where plastic

instability arises from diffuse and localized necking of the specimens, and a large load drop occurs prior to fracture.

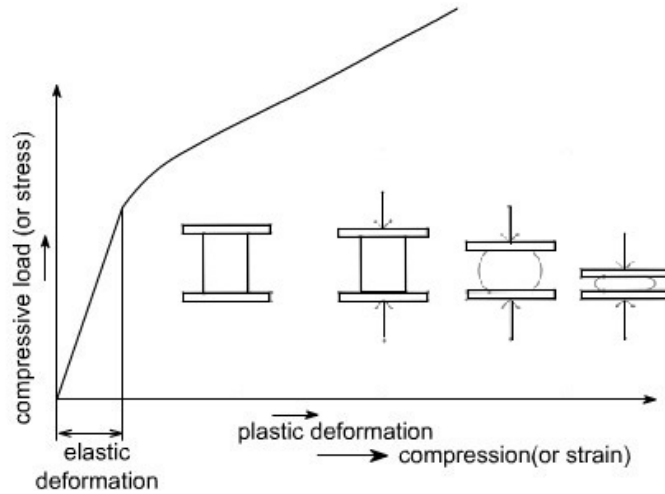


Figure 2.4. Axisymmetric compressive plastic deformation process of simple upsetting of cylinders (<http://nptel.ac.in/courses/112107146/12>).

2.1.3. Process parameters in simple upsetting

A simple uniaxial compression test can be conducted under well-controlled laboratory test conditions where process parameters can be carefully controlled and their role and significance can be determined. Previous work on uniaxial compression of cylinders and cubes has revealed that test results are influenced by many factors such as specimen geometry (i.e., aspect ratio of the cylinder), applied strain, strain rate, temperature, platen-work piece interface friction etc.

2.1.3.1. Specimen geometry

Cylindrical specimen geometry is the most common geometry in the lab-based simple uniaxial compression experiments. The initial dimension of the cylindrical specimen is represented by height H_0 and diameter D_0 (see Figure 2.5 below from (Li et al., 2011)). The barreled dimension of deformed cylindrical specimen is represented by top and bottom surface diameters d_{\min} , barreling region maximum diameter d_{\max} and height after compression h . As noted earlier, the friction at the specimen surface and platen leads to the barreling effect. Typically, the platen, as well as the top and bottom surfaces of the specimen, are applied with a low friction lubricant to reduce the amount of barreling. This is more challenging at elevated temperatures. Typically, solid lubricants, such as MoS_2 powder, graphite powder, Teflon tape, and liquid lubricants such as light oil, grease, and silicone oil are used (Hall et al., 2003). The lubricants can reduce the friction coefficients between the plate and specimen surface and reduce the amount of barreling (i.e., increase the amount of homogeneous deformation). The barreling effect leads to non-uniformity of the deformation process and increase in the circumferential (or hoop) tensile stress on the cylindrical specimen surface as indicated earlier in Figure 2.3.

Li et al. (Li et al., 2011) carried out interrupted compression tests on 6061-T6 aluminum with the specimen geometry shown in Figure 2.5. The aspect ratio of initial diameter to height is chosen as 0.5, 1.0 and 2.0. They also carried out some interrupted flange and tapered upsetting tests on the 6061-T6 aluminum and these are shown in Figure 2.6 and Figure 2.7 below. The interrupted test can lower the barreling effect for the test because the barreling effect is related to the initial height, the higher is the initial height for the same

cylinder diameter (i.e., higher is the aspect ratio of cylinder), the lesser is the amount of barreling.

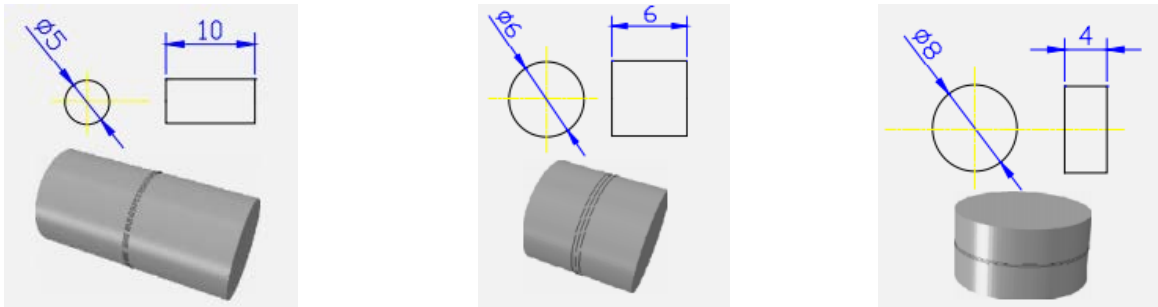


Figure 2.5. The cylindrical specimen geometry of various ratio of diameter and initial height (Li et al., 2011).

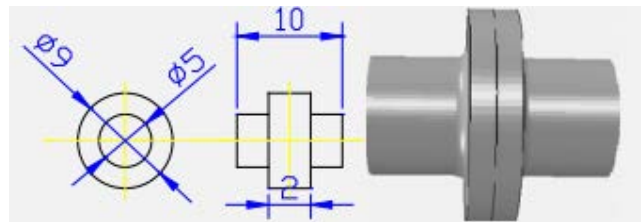
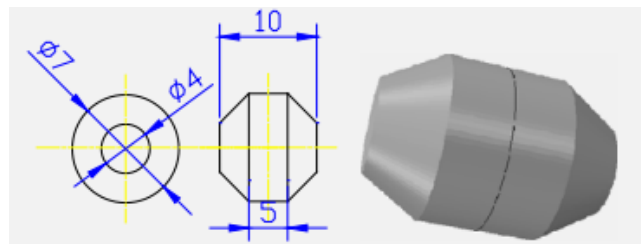


Figure 2.6. Geometry and fracture phenomena in the flanged upsetting (Li et al. 2011).



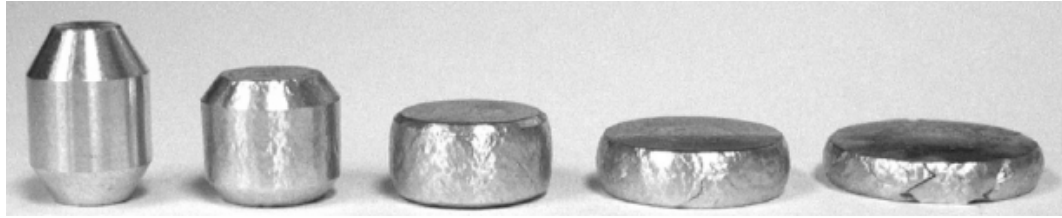


Figure 2.7. Geometry and fracture phenomena in the tapered upsetting (Li et al., 2011).

2.1.3.2. Strain rate (or test speed)

The compression strain rate at a given test temperature can affect the stress-strain response in a simple uniaxial compression test, especially at elevated temperatures. This is shown in Figure 2.8 for 2124-T851 alloy tested at 380 °C at a range of constant strain rate tests. The yield strength is shown to increase for this material as the strain rate is increased (Lin et al., 2010). The increased elongation at lower strain rates and higher temperatures is often attributed to increased rate sensitivity of the material. Also, the material exhibits strain softening soon after reaching its yield point. The strain softening can occur from increased dynamic recovery and recrystallization of the material at higher temperatures (Zhang et al., 2007). Similar effect has been observed in other aluminum alloys [Lin et al., (2008), Chen et al., (2012) and Li et al., (2017)]. However, at lower temperatures, the rate effects can be quite small and often negligible due to reduced strain rate sensitivity of aluminum alloy at lower temperatures. In fact, many aluminum alloys exhibit flow stress curves which are independent of strain rate at room temperature [Paul and Ramamurty (2000) and Höppel et al., (2005)].

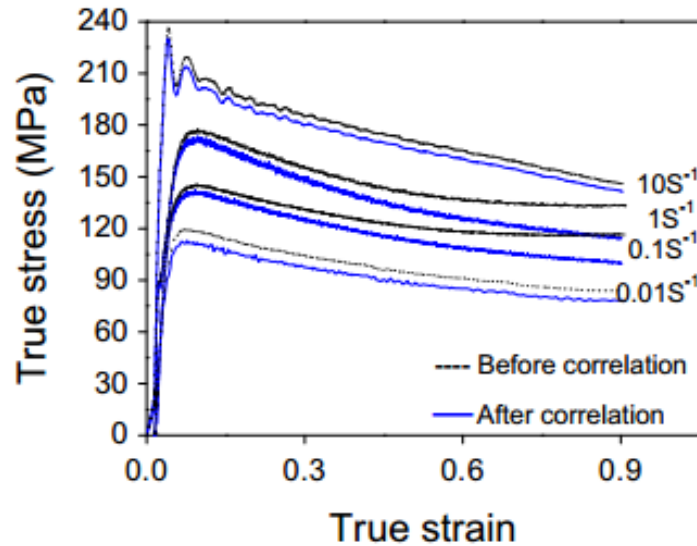


Figure 2.8. True stress and true strain curves of 2124-T851 Al at 380 °C in different strain rate (Lin et al., 2010).

2.1.3.3. Test temperature

Luo et al., (2012) studied the formability of high strength aluminum alloy (AA7075-T6) at elevated temperature by uniaxial compression test. Their compressive stress-strain curves at a range of temperatures (from 20 °C to 260 °C), corresponding to a constant strain rate of 0.078 s^{-1} , are shown in Figure 2.9. In the lower temperature range of about 20 °C-100 °C, the changes in the stress-strain curves are rather small. However, at temperatures in the range 140 °C-220 °C, the true stresses decrease and true strain increase sharply. At a temperature of 260 °C, both the flow stress and strain to fracture decrease. This anomalous behavior at 260 °C could result from microstructural changes in the material such as by resolution of precipitates and hence elimination of the hardened T6 temper, although no clear

explanation is available in the literature. In summary, the temperature is a key process variable in uniaxial compression of aluminum alloys as it affects the flow stress (and thus the forming load) and the limit strain (or formability) of the material.

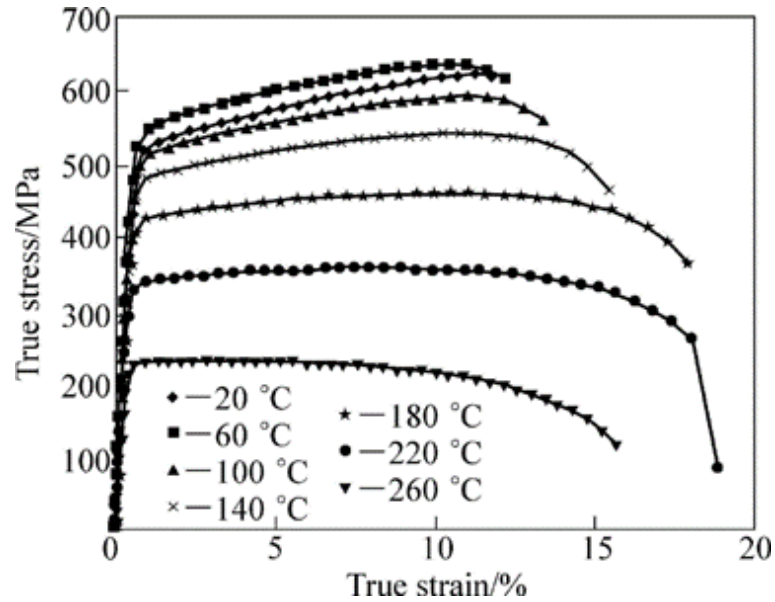


Figure 2.9. True stress-true strain curves of AA7075 at several elevated temperatures (Strain rate is 0.078 s^{-1}) (Luo et al., 2012).

2.1.4. Other factors affecting uniaxial compression behavior of aluminum alloys

Table 2.1 below provides a summary of recent studies related to common precipitation-hardenable aluminum alloys in uniaxial compression from literature. In addition to strain rate and temperature, effect of specimen aspect ratio and lubrication between specimen and platen have been studied as well. Most of these studies have been carried out at a constant

temperature and utilize cylindrical specimens. Studies related to transient temperature conditions such a hot specimen placed between cold compression platens and then formed under ambient air atmosphere are limited. Also, studies on cubic or other shapes are very limited.

Table 2.1. Recent studies on uniaxial compression tests on precipitation-hardenable aluminum alloys from literature.

References	Sample geometry	Temperature condition	Workpiece material	Process parameter(s)
(Lee et al., 2000)	Cylindrical	Isothermal	AA7075-T6 aluminum alloy	Strain rate and temperature
(Bao and Wierzbicki 2004)	Cylindrical	Isothermal	2024-T351 aluminum alloy	Ratio of D_0/H_0
(Li et al., 2009)	Cylindrical	Isothermal	AA2024-T651 aluminum alloy	Strain rate, geometry and lubricant
(Wang et al., 2012)	Cylindrical	Isothermal	AA7075-T6 aluminum alloy	Strain rate and temperature
(Kitamura and Terano 2014)	Cubic	Isothermal	Aluminum alloy (unknown)	Orientation
(Jiang et al., 2015)	Cylindrical	Non-isothermal	AA7150-F aluminum alloy	Strain rate and temperature

2.1.5. A summary of studies on AA7075, and another common alloy AA2024 at elevated temperatures using uniaxial compression tests

2.1.5.1. AA7075 aluminum alloy composition and processing

Typical composition range of AA7075 aluminium in weight percent consists of 5.6–6.1% zinc, 2.1–2.5% magnesium, 1.2–1.6% copper, and less than a half percent of silicon, iron, manganese, titanium, chromium, and other metals. The high strength of AA7075 comes from the addition of Zn, Mg, Cu and small amounts of Ti, Cr and other metals which enable precipitation hardening strengthening mechanism to operate after water quenching and artificial ageing of the materials to desirable tempers.

2.1.5.2. AA7075 alloy temper states

AA7075 aluminum alloy is produced in many tempers, some typical tempers are O, T6, T651 and T7. A schematic diagram that displays the temperature-time history to achieve each of the above tempers is shown in Figure 2.10 below.

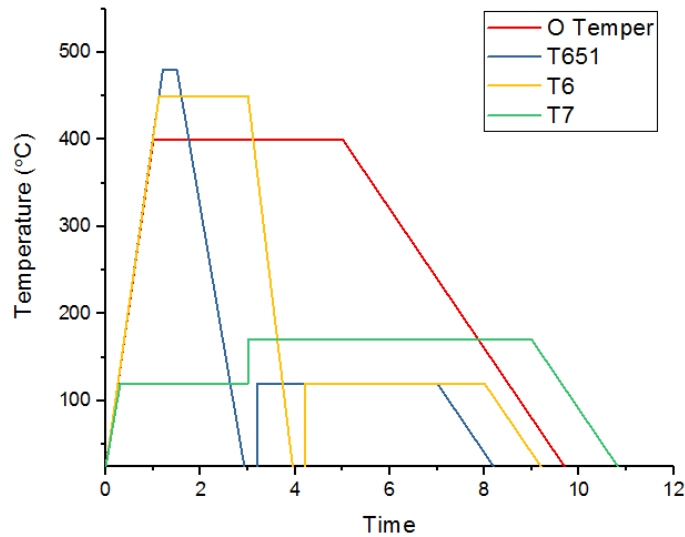


Figure 2.10 Temperature-time history of above tempers

(https://en.wikipedia.org/wiki/7075_aluminium_alloy#cite_note-4).

For O temper, the alloy is heated to 400 °C for about 5 hours and then slowly furnace cooled to room temperature. T6 temper is usually achieved by homogenizing the cast AA7075 at 450 °C for several hours, quenching, and then aging at 120 °C for 24 hours. T651 is similar to T6 by heating the alloy for 50 minutes at 480 °C followed by quenching and aging at 120 °C for 24 hours, and then subjecting it to a small plastic deformation. T7 temper is often accomplished by aging at 120 °C for several hours and then over-aging at 160-180 °C for 24 hours or more.

The specific differences in room temperature material properties for each temper are shown in Table 2.2. As shown, the different tempers may have a significant effect on yield stress,

ultimate tensile strength and uniform elongation of AA7075 alloy in uniaxial compression. At room temperature, lowest and highest yield stress and the ultimate tensile strength values are exhibited by O and T651 tempers. The overaged temper T7, on the other hand, has the largest elongation than all other tempers in AA7075 aluminum alloys. The O-temper also exhibits good elongation for cold upsetting of simple parts.

Table 2.2 Material properties in different tempers of AA7075 aluminum alloy (Park and Ardell 1983).

Temper	AA7075-O	AA7075-T6	AA7075-T651	AA7075-T7
Yield Strength	140 MPa	430-480 MPa	500 MPa	435 MPa
Ultimate Tensile Strength	280 MPa	510-540 MPa	570 MPa	505 MPa
Uniform elongation	9-10 %	5-11 %	3-9 %	13 %

2.1.5.3. AA7075 strain hardening characteristics

Strain hardening is the strengthening of a metallic material by plastic deformation. This strengthening occurs because of dislocation movements and generation within the polycrystalline structure of the metallic material. The commonly used hardening law, also known as power or Hollomon law, is written as:

$$\sigma = K \varepsilon_p^n \quad (2.1)$$

where σ is the stress, K is the strength coefficient, ε_p is the plastic strain and n is the strain hardening exponent, a material parameter of much significance in assessing workability in

simple upsetting. Since stress and strain are both temperature dependent, the above relationship is expressed as (Hu et al., 2012):

$$\sigma(T) = K(T)\varepsilon_p^{n(T)} \quad (2.2)$$

However, specific function relating n value to temperature for AA7075 aluminum alloy could not be found in the literature.

2.1.5.4. Strain rate sensitivity

Similar to strain hardening, the flow stress of most metals also varies with strain rate $\dot{\varepsilon}$ and temperature. The change in flow stress with strain rate at constant strain (or microstructure) and temperature is generally expressed as:

$$\sigma = C\dot{\varepsilon}^m \quad (2.3)$$

where m is referred to as strain rate sensitivity of the material. The m -value in eqn. 2.3 can be also written as:

$$\ln\sigma = \ln C + m \ln\dot{\varepsilon} \quad (2.4)$$

$$m = \frac{\ln(\frac{\sigma}{C})}{\ln(\dot{\varepsilon})} \quad \text{or} \quad m = \frac{d\ln(\sigma)}{d\ln(\dot{\varepsilon})} \quad (2.5)$$

Similar to the n -value, the m value is also dependent on temperature of deformation. It is also dependent on the grain size and shape as well as the underlying fundamental mechanisms of deformation such as grain rotation, grain boundary sliding, and grain boundary diffusion at elevated temperatures.

From the uniaxial compression stress-strain data of Jenab et al. (Jenab and Taheri 2014) on AA7075 aluminum alloy, the specimens were heat treated at 345 °C for 3 h and air cooled to room temperature to eliminate any machining residual stresses. The tests were conducted at strain rates of 0.003 s⁻¹, 0.001 s⁻¹, 0.01 s⁻¹, 0.1 s⁻¹ and 1 s⁻¹ and temperatures of 200 °C, 250 °C, 300 °C, 350 °C, 400 °C and 450 °C. A relationship between *m*- value and temperature was then obtained in the range of the strain from 0.1 to 0.7 as shown in Figure 2.11 below. The value of *m* increased with increase in temperature and converged at 350 °C, which means at higher temperature condition, strain rate may have a larger effect on the flow stress. A higher *m* value also means an increased strain to fracture.

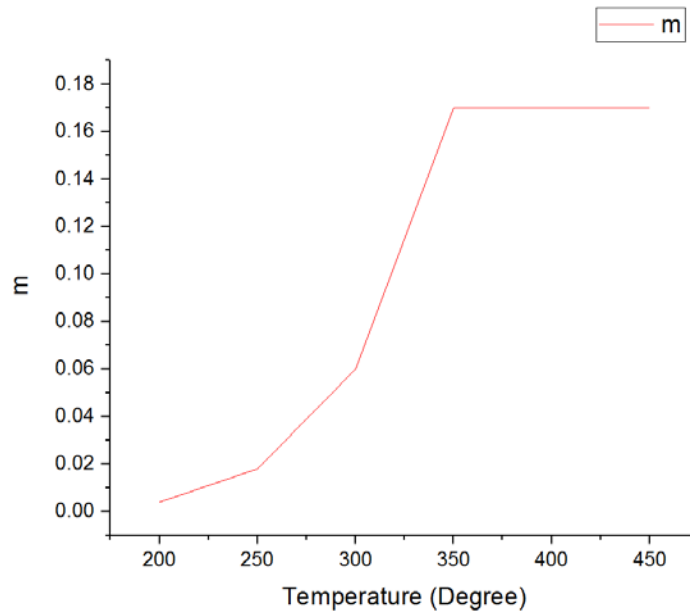


Figure 2.11 Strain rate sensitivity parameter (*m*) plotted as function of temperature for AA7075 alloy (Jenab and Taheri 2014).

In another similar study by (Wang et al., 2012), involving uniaxial compression tests on AA7075-T6 alloy at various strain rates of 0.008 s^{-1} , 0.025 s^{-1} and 0.583 s^{-1} and temperatures of $140 \text{ }^\circ\text{C}$, $180 \text{ }^\circ\text{C}$ and $220 \text{ }^\circ\text{C}$, the maximum m -value was obtained at $180 \text{ }^\circ\text{C}$ but dropped as the temperature was increased further as shown in Figure 2.12. Therefore, there is some inconsistency in the data reported in the literature. At the room temperature, no effect of strain rate on flow stress-strain behavior of the material was observed.

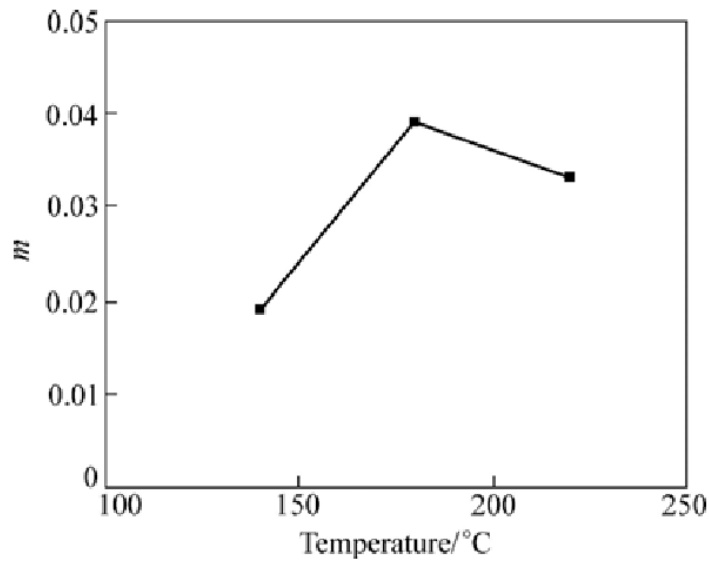


Figure 2.12. Strain rate sensitivity parameter (m) plotted as function of temperature for AA7075-T6 alloy (Wang et al., 2012).

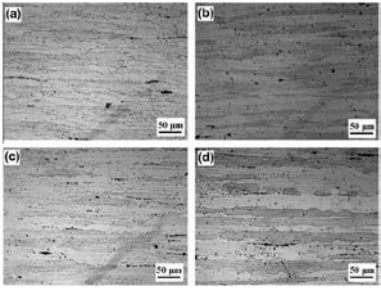
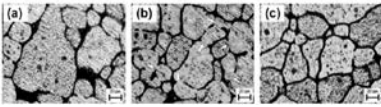
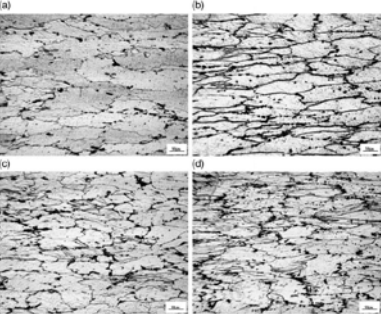
Both researchers provided the experimental trend in m value with temperature, but no specific function that related the two quantities.

2.1.6. Microstructure and texture evolution during elevated temperature uniaxial compressive deformation of 7xxx aluminum alloys

2.1.6.1. Grain size evolution

7xxx series aluminum alloys not only have the advantage of lightweight like other types of aluminum alloys but also have high strength. Increased strength of these alloys is due to the addition of alloying elements such as Zn, Mg, and Cu which result in precipitation of fine microstructural precipitates. However, they reduce room temperature ductility as well as hot workability. Workability is usually defined as the amount of deformation that a material can undergo without cracking and reach desirable deformed microstructure at a given temperature and strain rate. Typical microstructures of several AA7xxx series alloys tested in uniaxial compression at different temperatures and strain rates are shown in Table 2.3. Chen (Chen et al., 2012) conducted hot deformation studies on AA7085 alloy in the temperature and strain rate ranges from 350 °C and 450 °C and from 0.001 s⁻¹ and 1 s⁻¹ respectively. The results show that grains elongate and dynamically recrystallize into smaller grains. When the temperature increases from 350 °C to 450 °C, the grains become flatter. Also, there are less precipitates, but of larger size, when the temperature increases and the material is able to flow easily. Zarei-Hanzaki et al. (2011) studied the microstructure of AA7075 after hot compression at a rather high temperature of 580 °C and strain rates of 0.004 s⁻¹, 0.04 s⁻¹ and 0.4 s⁻¹. As shown in Table 2.3, significant grain refinement occurred with increased strain rate. Similar observations were made in the experimental study by Jin et al., (2009) on hot compression of AA7150 alloy.

Table 2.3. Grain characteristics of high strength 7xxx aluminum alloys subjected to hot compression tests.

References	Material	Test conditions	Microstructure
(Chen et al., 2012)	AA7085	(a) $T=350\text{ }^{\circ}\text{C}$, $\dot{\epsilon}=1\text{ s}^{-1}$ (b) $T=350\text{ }^{\circ}\text{C}$, $\dot{\epsilon}=0.001\text{ s}^{-1}$ (c) $T=450\text{ }^{\circ}\text{C}$, $\dot{\epsilon}=1\text{ s}^{-1}$ (d) $T=450\text{ }^{\circ}\text{C}$, $\dot{\epsilon}=0.001\text{ s}^{-1}$	
(Rokni et al., 2011)	AA7075	$T=580\text{ }^{\circ}\text{C}$ $\dot{\epsilon}=(a)\ 0.004\text{ s}^{-1}$ (b) 0.04 s^{-1} (c) 0.4 s^{-1}	
(Jin et al., 2009)	AA7150	(a) $T=450\text{ }^{\circ}\text{C}$, $\dot{\epsilon}=0.01\text{ s}^{-1}$ (b) $T=400\text{ }^{\circ}\text{C}$, $\dot{\epsilon}=0.1\text{ s}^{-1}$ (c) $T=350\text{ }^{\circ}\text{C}$, $\dot{\epsilon}=1\text{ s}^{-1}$ (d) $T=300\text{ }^{\circ}\text{C}$, $\dot{\epsilon}=10\text{ s}^{-1}$	

As the temperature decreases and the strain rate increases, the grains become elongated and possess high-angle grain boundaries. Such grains undergo dynamic recrystallization (DRX) during the hot compression test. A simplified schematic of the DRX process from is shown in the Figure 2.13.

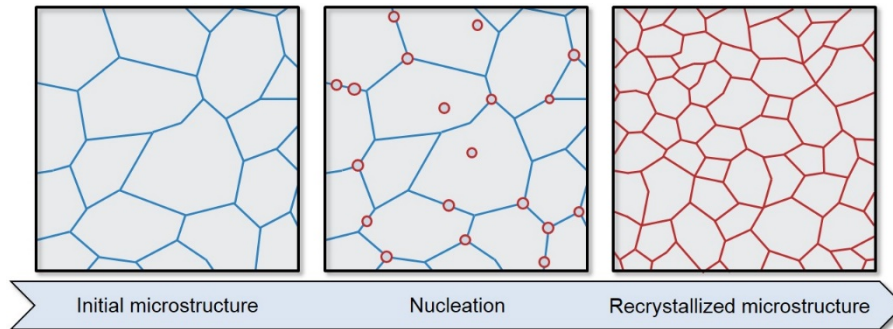


Figure 2.13. The process of dynamic recrystallization during hot compression of aluminum alloys (<http://www.hhallberg.com/p=556>).

2.1.6.2. Texture evolution

Typical 7xxx series alloy crystallographic textures from electron backscatter diffraction (EBSD) experiments using SEM equipment are shown in Table 2.4. In each EBSD image in column 4, grains of different morphology and orientations are revealed as the specimens are compressed at different rates. For example, in the work of Deng et al., (2011), the grains of hot compressed AA7050 alloy at 623 K and 673 K, and at strain rates of 1 s^{-1} , 0.01 s^{-1} and 0.0005 s^{-1} , exhibit more elongation under (i) lower temperature at constant strain rate, and (ii) lower strain rate at constant temperature, see row 1 of Table 2.4. Wang et al., (2012) studied the strain effects on microstructure behavior of 7050-H112 aluminum alloy during hot compression at $450 \text{ }^\circ\text{C}$ and the strain rate is 1 s^{-1} where the specimens were compressed to axial strain values of 0.34, 0.9 and 1.6. From Table 2.4, it can be clearly seen that many fine grains with high angle boundaries evolved along the original grain boundaries and some dislocation substructures are revealed in the grain interior. These substructures appear to increase in density with increasing applied strain from 0.3 to 0.9.

However, at larger strain of 1.6, the dislocations rearrange in to embryos and promote grain recrystallization leading to smaller grains with significantly less dislocation substructures. Similar results can be observed in the work of Jin et al., (2009) on AA7055 alloy in Table 2.4.

Table 2.4. Crystallographic textures from EBSD experiments on hot compressed test samples of 7xxx series aluminum alloys.

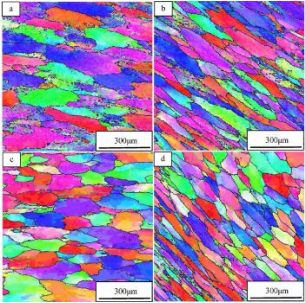
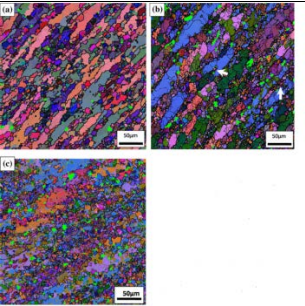
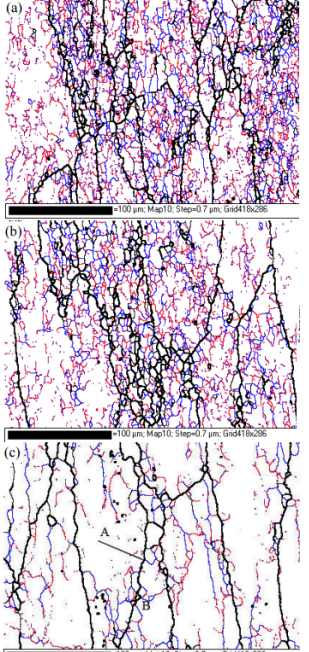
References	Material	Test conditions	Microstructure
(Deng et al., 2011)	AA7050	(a) $T=623\text{ K}, \dot{\epsilon}=1\text{ s}^{-1}$ (b) $T=623\text{ K}, \dot{\epsilon}=0.01\text{ s}^{-1}$ (c) $T=673\text{ K}, \dot{\epsilon}=0.01\text{ s}^{-1}$ (d) $T=623\text{ K}, \dot{\epsilon}=0.0005\text{ s}^{-1}$	
(Wang et al., 2012)	AA7050-H112	$T=450\text{ °C}, \dot{\epsilon}=1\text{ s}^{-1}$ (a) $\epsilon=0.34$ (b) $\epsilon=0.9$ (c) $\epsilon=1.6$	

Table 2.4. Continued...

(Jin et al., 2009)	AA7055	<p>(a) $T=350\text{ }^{\circ}\text{C}$, $\dot{\epsilon}=0.01\text{ s}^{-1}$</p> <p>(b) $T=400\text{ }^{\circ}\text{C}$, $\dot{\epsilon}=0.1\text{ s}^{-1}$</p> <p>(c) $T=450\text{ }^{\circ}\text{C}$, $\dot{\epsilon}=0.1\text{ s}^{-1}$</p>	
--------------------	--------	---	--

2.1.7. Fracture characteristics during elevated temperature simple upsetting of 7xxx aluminum alloys

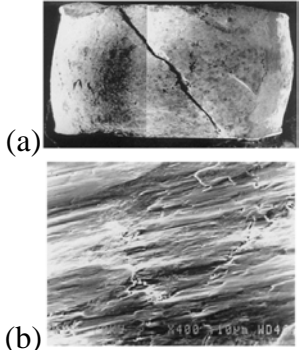
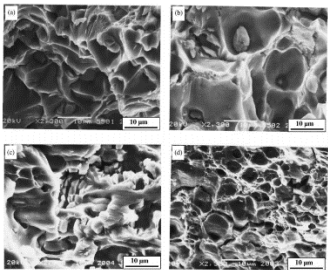
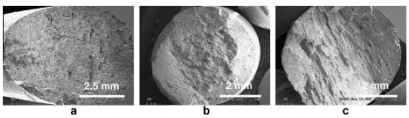
A fracture is the physical separation of an object or material under the action of load or stress. The fracture of a solid usually occurs due to the development of certain displacement discontinuity on the surface or within the plastically deforming solid. While fracture is to be avoided in a manufacturing process, a study of fracture behavior of the material is critical to understanding the limits of workability and the ability to make parts by forming processes. The fracture characteristics during uniaxial compression or simple upsetting such as fracture orientation and type of fracture (brittle or ductile) are affected by applied

strain, strain rate and temperature. Typical fracture characteristics of 7xxx series aluminum alloys under hot uniaxial compression are presented in Table 2.5.

Lee et al., (2000) compared the fracture orientation and surface features of cylindrical specimens taken to fracture at 200 °C and 300 °C and at a very high strain rate of 3100 s⁻¹. Typical slant failure with a failure angle of 45° with respect to the axis of loading is observed often in such tests, as shown in Table 2.5, row 1. Shear bands can be observed in the SEM image of the fractured surface. These are narrow bands within the faceted, relatively smooth, fracture surface that lead to the separation of the specimen (see Figure (b), in row 1). Fine striations can be seen running parallel to the shear direction. Chen et al., (2003) compared the fracture features of AA7055 alloy specimen after hot compression for different initial microstructures arising from various heat treatment as shown in Table 2.5. Microstructure in row 2, figure (a), shows dimples (or voids) of various sizes on the fracture surface indicative of ductile rupture. Constituent particles can be seen inside some of the voids as well. It is evident from figures (a) and (b) that the coarse constituents fractured first and acted as a precursor to the formation of micro-cracks. This kind of mixed fracture, in which fracture is initiated at second phase particles and links up along the matrix grain boundaries has been reported for other materials. The improved dissolution of the coarse constituent particles by two-step solution heat-treatment allowed the matrix grains to deform evenly, avoiding early rupture and resulting in a large number of smaller dimples, as shown in figures (c) and (d). The work of Pedersen et al., (2011) shows the fracture surfaces of 3 specimens tested in three different orientations (see row 3 of Table 2.5) . The

samples were machined from AA7150-T651 plate stock along 0°, 45° and 90° with respect to the rolling direction of the plate. The samples tested in the rolling direction failed in shear mode approximately 45° to the applied load direction with almost no necking, while the specimens in the two other orientations showed a rough, irregular fracture surface and the strains to fracture were higher.

Table 2.5. Fracture characteristics of 7xxx series aluminum alloys under hot uniaxial compression.

References	Material	Test conditions	Microstructure
(Lee et al., 2000)	AA7075-T6	(a) T=200 °C, $\dot{\epsilon}=3100 \text{ s}^{-1}$ (b) T=300 °C, $\dot{\epsilon}=3100 \text{ s}^{-1}$	
(Chen et al., 2003)	AA7055	Heat treatment conditions: (a) T=455 °C/2h (b) T=455 °C/1h (c) T=455 °C/1h, 5–15 °C/h and 485 °C/2 h (d) T=455 °C/1h, 5–15 °C/h and 490 °C/2h	
(Pedersen et al., 2011)	AA7150-T651	Cutting from a plate At room temperature (a) Rolling direction (0°) (b) 45° direction (c) Long transverse direction (90°)	

2.2. Strain rate and temperature dependent constitutive material models of plastic deformation of 7xxx series aluminum alloys

Material constitutive laws that represent temperature and strain rate dependent flow stress-strain curves are useful not only for understanding of the material behavior in terms of strength and elongation but also for die design and elevated part forming simulations using the finite element method. These are essential components of any plastic analysis of a deforming material. Several material temperature and strain rate dependent constitutive hardening laws have been proposed to describe the behavior of AA7xxx alloys under hot compression. In general, constitutive laws dealing with thermo-mechanical deformation are often highly simplified empirical expressions in the literature and therefore have poor physical basis in the deformation behavior of a specific material systems. The most widely used approaches to analyze high-temperature uniaxial compression of AA7xxx alloys include Johnson-Cook, Zerilli-Armstrong, Mechanical Threshold Stress (MTS), Voce-Kocks, and Arrhenius equation models. The classical Swift (or power law) equation is typically extended to include strain rate and temperature effect on flow stress (and strain), by introducing a so-called Zener-Hollomon parameter. The general form for each of the above constitutive material model is shown in Table 2.6 below. All of these mathematical forms have flow stress as a function of strain, strain rate and temperature and a number of material parameters. Some of them also involve reference temperature, reference stress or reference strain rate values. Johnson-Cook (J-C) model, for example, involves strain, strain rate and temperature components in a simple multiplicative form as shown in Table 2.6

(see row 1, column 2) where square brackets separate the contributions of each component. The material constants are A , B , n represent a Swift law-type strain hardening. The material constants C and reference strain rate $\dot{\epsilon}_0$ strain rate effect. Lastly, parameters such as reference temperature T_{room} and melting temperature T_{melt} represent the temperature effect in their simplest form. While J-C model is widely used to represent many hot deformation conditions for different ferrous and aluminum alloys, and is available in many commercial FE codes, it has limited use in cases where materials, including AA7075-T6 alloy, exhibits strain softening (high temperature and slow strain rate conditions). Similar comments can be made for other constitutive material models such as Zerilli-Armstrong, MTS, V-K and Arrhenius equation. In some cases, extrapolations beyond the range of fit deviate sharply in terms of the shape and values and the interpolations do not match well with the experimental data. The number of fit parameters can be large in many cases and it is often difficult to assign physical meaning to many of them. This is especially true, when the material, such as AA7075 alloy, exhibits multiple flow stress versus strain shapes depending on the strain rate and temperature, as shown in Figure 2.14 below.

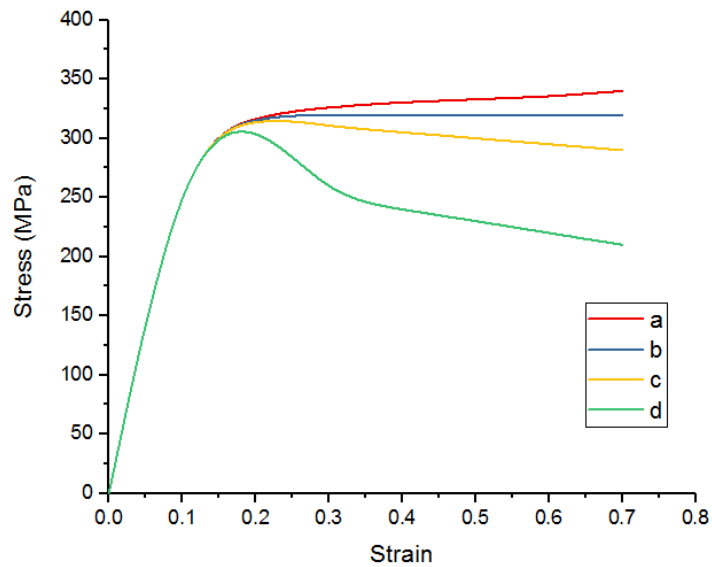


Figure 2.14. Stress-strain shapes for AA7075 alloy.

Figure 2.14 is a schematic, and does not show real experimental curves, because every reference paper has different material and test conditions, and therefore, the experimental curves were modified from the literature to represent general shapes. The 4 curves (a-d) indicate; (a) continued strain hardening to fracture (Wang et al., 2017), (b) strain hardening to stress saturation and fracture (Rokni et al., 2011), (c) strain softening immediately after yield (Wang et al., 2012), and (d) strain hardening followed by strain softening (Rokni et al., 2011). All of these shapes of flow stress-strain curves perhaps arise from changes in deformation mechanisms at the microstructural level as a function of strain rate, temperature, grain structure and crystallographic texture of the alloy. In summary, formulating a strain rate and temperature dependent constitutive material model for AA7075 alloy that applies to a wide range of practical temperatures and strain rates

(deformation speeds) and yet involve few parameters that could be easily determined with simple experimental infrastructure remains a challenge. A few modified constitutive models have been implemented as a User material subroutine for ABAQUS/Standard FE code and utilized in the simulations of lab-based hot compression experiments in the literature. This will be also covered in more detail in Chapter 4. Also, a couple of the existing constitutive material models have been modified to represent hot compression test data on AA7075 alloy in the present study. This will be covered in Chapter 5.

Table 2.6. The Constitutive material models of plastic deformation of AA7075 aluminum alloy.

Researchers	Formula	Constitutive Model
(Brar et al., 2009)	$\sigma = [A + B\varepsilon_p^n] \left[1 + C \ln \left(\frac{\dot{\varepsilon}}{\dot{\varepsilon}_0} \right) \right] [1 - T^{*m}]$ $T^* = \frac{T - T_{room}}{T_{melt} - T_{room}}$	Johnson-Cook Model
(Smerd, 2005)	$\sigma = \Delta\sigma_{G'} + C\varepsilon^{\frac{1}{2}} \exp(-C_1T + C_2T \ln \dot{\varepsilon}) + k\dot{\varepsilon}^{\frac{1}{2}}$	Zerilli-Armstrong model
(Smerd, 2005)	$(\sigma - \sigma_a)^r = \Sigma [S_i(\dot{\varepsilon}, T) \hat{\sigma}_i]^r$	Mechanical threshold stress model

Table 2.6. Continued...

(Kocks, 1976)	$\sigma = \sigma_s + (\sigma_0 - \sigma_s) \exp\left(-\frac{\varepsilon}{\varepsilon_r}\right)$ $\begin{cases} \sigma_s = \sigma_{s0} \left(\frac{\dot{\varepsilon}}{y_s}\right)^{\frac{kT}{A_s}} \\ \sigma_0 = \sigma_{k0} \left(\frac{\dot{\varepsilon}}{y_k}\right)^{\frac{kT}{A_k}} \end{cases}$	Voce-Kocks model
(Naser and Kraljics, 2014)	$\sigma = \frac{\operatorname{arcsinh}\left(\exp\left(\frac{RT(\ln(\dot{\varepsilon}) - \ln(A)) + Q}{RTn}\right)\right)}{\alpha}$	Arrhenius equation

2.3. Analytical modeling

Analytical models of uniaxial compression test are mathematical models that represent in a simplified manner the specimen geometry and loading, and incorporate theory of plasticity and mechanics of uniaxial compressive deformation. They can be in a closed form algebraic equation or in the form of a differential equation that could be solved numerically. The advantages of analytical models are that they are faster and easier to analyze. On the other hand, they may not capture all of the characteristics of an experimental hot compression test. For instance, an analytical model of hot cylindrical compression test on 1040 steel was developed by Kobayashi et al. (Kobayashi et al., 1970). The geometrical details of this model are given in Figure 2.15.

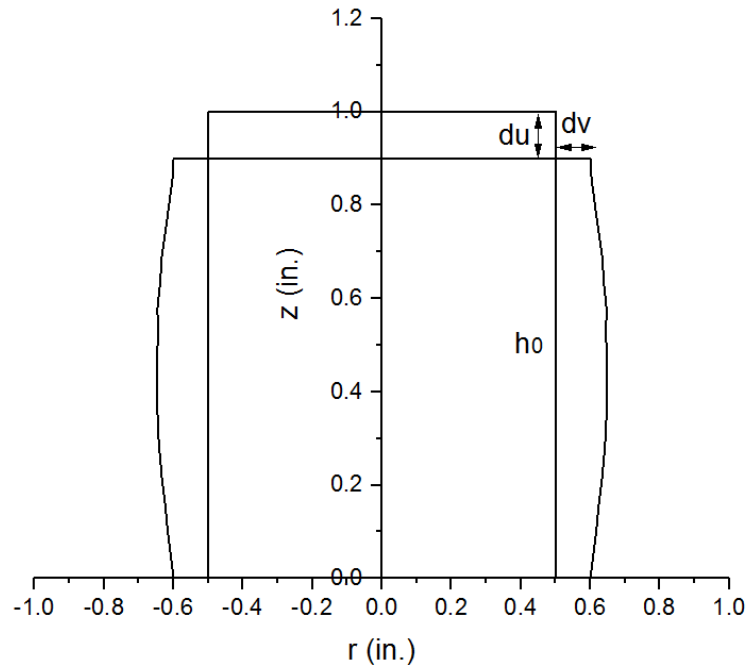


Figure 2.15. The geometrical details of the analytical model.

Kobayashi assumed the following equations for incremental radial displacement du and axial dv in upsetting of a cylinder:

$$du = a_1 r(1 - \lambda z^2) + a_2 r^3 \quad (2.6)$$

$$dv = -2a_1 \left(z - \frac{\lambda}{3} z^3 \right) - 4a_2 r^2 z \quad (2.7)$$

In the above equations for du and dv , the functions a_1 and a_2 are described later. The symbols z , and r refer to the axial and radial coordinates. The symbol λ was friction

coefficient in this paper, and the values of λ were 0.4, 0.8, 2.2 and 3.4. The incompressibility condition was expressed as:

$$\frac{\partial(\mathrm{d}u)}{\partial r} + \frac{\mathrm{d}u}{r} + \frac{\partial(\mathrm{d}v)}{\partial z} = 0 \quad (2.8)$$

where $z=0$ was taken at half-height of the specimen. The inclination θ of the principal stress direction relative to the radial (or r) axis was related to the incremental strains with the following expression:

$$\tan 2\theta = \frac{\frac{\partial(\mathrm{d}v)}{\partial r} + \frac{\partial(\mathrm{d}u)}{\partial z}}{\frac{\partial(\mathrm{d}u)}{\partial r} - \frac{\partial(\mathrm{d}v)}{\partial z}} = \frac{-(8a_2 + 2\lambda a_1)}{3a_1(1 - \lambda z^2) + 7a_2 r^2} \quad (2.9)$$

For $z = 0$, $\rho\theta = z$, ρ is the radius of curvature of the trajectory of the principle stress direction. So, at $z = 0$ and $r = R$, the equation (2.9) reduces to the following expression

$$\frac{-(8a_2 + 2\lambda a_1)}{3a_1 + 7a_2 R^2} = \frac{2}{R\rho} \quad (2.10)$$

where R is the radius of the equatorial free surface. The functions a_1 and a_2 are shown below:

$$a_1 = \frac{7R^2 + 4R\rho}{4R^2 + 4R\rho - \lambda R^3 \rho} d\varepsilon_\theta \quad (2.11)$$

$$a_2 = \frac{3 + \lambda R\rho}{4R^2 + 4R\rho - \lambda R^3 \rho} d\varepsilon_\theta \quad (2.12)$$

Substituting factors a_1 and a_2 , given by equation (2.11) and (2.12), into equation (2.13) below:

$$d\varepsilon_r = \frac{\partial(du)}{\partial r} = a_1 + 3a_2R^2 \quad (2.13)$$

at $z = 0$ and $r = R$, the following relationship was obtained:

$$d\varepsilon_r = \frac{4\rho - 2R - 3\lambda R^2 \rho}{4\rho + 4R - \lambda R^2 \rho} d\varepsilon_\theta \quad (2.14)$$

From the relationship in equation 2.14, the curve of ε_r and ε_θ (i.e., strain paths) were plotted by selecting the value of λ to fit the experiment curve. These are shown below in Figure 2.16 below.

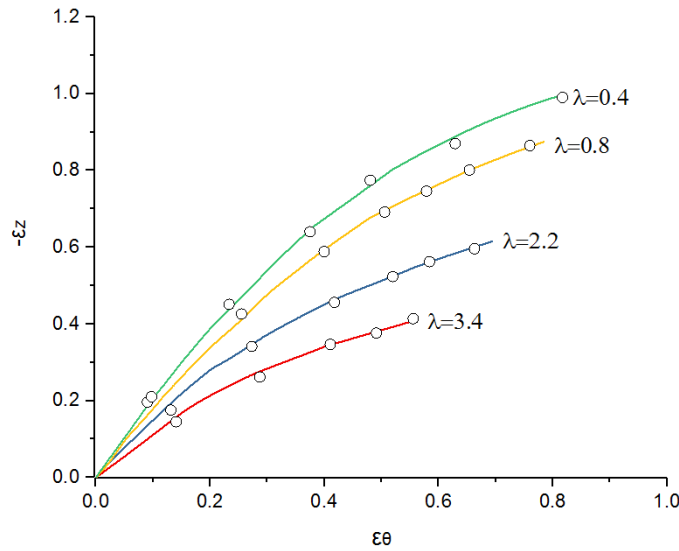


Figure 2.16. Calculated strain paths and comparison with the experimental (the line represent calculation data and the circle represent experimental data) (Kobayashi et al.,

1970).

2.4. Finite element modeling of uniaxial hot compression test

Besides the experimental studies and analytical modeling, finite element (FE) method is a powerful numerical analysis tool that is increasingly being used to simulate bulk forming processes such as simple upsetting to understand the mechanics of material flow. The method also allows for conducting systematic parametric studies towards analyzing the effect of material and process parameters on material flow behavior, formability and damage development, similar to the experimental studies. An advanced FE model that incorporates a good representation of material behavior in the form of a constitutive law, as well as other condition of the experiments, can be useful in optimizing the upsetting process in a cost-effective manner. A list of FE modeling-based studies of hot uniaxial compression test is given in Table 2.7 below.

Table 2.7. Different studies on FE modeling of hot compression test.

Researcher	FE-code	Element type	Material model	Fracture criterion
(Wang et al., 2017)	ABAQUS/Explicit	C3D8R	Mises	N/A
(Bao and Wierzbicki, 2004)	ABAQUS/Standard	4-node axisymmetric	Johnson-Cook	McClintock
(Sofuoglu and Rasty, 1999)	ABAQUS/Explicit	2D axisymmetric	N/A	N/A
(Brar et al., 2009)	DYNA3D, EPIC	N/A	Johnson-Cook	N/A
(Bai and Wierzbicki, 2008)	ABAQUS/Explicit-VUMAT	3D asymmetric	Johnson-Cook	McClintock, Rice and Tracey
(Gao and Kim, 2006)	ABAQUS/UHARD	2D axisymmetric	Gurson-Tvergaard	Porous failure criteria

2.5. Non-isothermal hot compression studies on AA7xxx alloys

Isothermal condition is the most commonly used test condition for studying the hot compression behavior of materials in the literature. However, there is interest in also understanding the material behavior under transient conditions where a workpiece may be hot as it is removed from a furnace and then placed on a cold die for upsetting. This case is more complex as the workpiece is cooling by conduction from contact with the tooling as well as by convection and radiation to the surrounding air while it is being formed with a cold die. Unfortunately, very few studies have studied the non-isothermal compression test. (Jiang et al., 2015) explored the non-isothermal hot compression test on AA7150 aluminum alloy at dynamic temperature and various strain rates. A cylindrical specimen, 10 mm in diameter and 15 mm in height was used for the non-isothermal compression test. The tests consisted of pre-heating samples to 425 °C for 180 s, then gradually cooling it down to 325 °C during the deformation with equal pass strain of 0.2 and inter-pass intervals of 10 s. The strain rates were 0.01 s⁻¹, 0.1 s⁻¹ and 1 s⁻¹ respectively. The result of true stress and true strain curve in various temperatures and strain rates are shown in Figure 2.17.

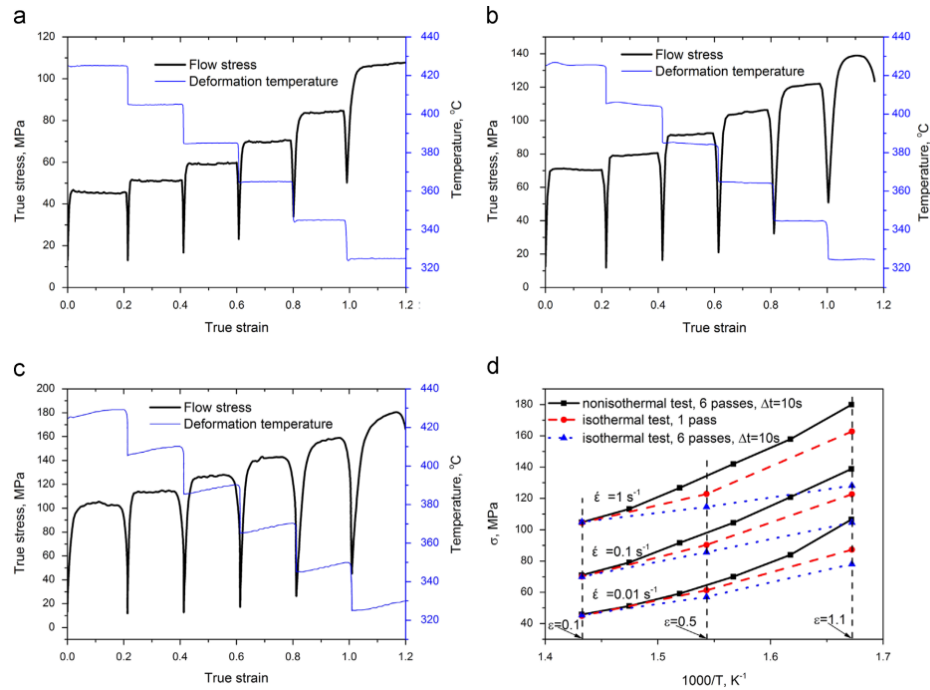


Figure 2.17. Flow stress of 7150 aluminum alloy during non-isothermal hot compression with the temperature decreasing from 425 °C to 325 °C with interval of 10 s: (a) $\dot{\epsilon} = 0.01 \text{ s}^{-1}$, (b) $\dot{\epsilon} = 0.1 \text{ s}^{-1}$, (c) $\dot{\epsilon} = 1 \text{ s}^{-1}$ and (d) comparison among non-isothermal stresses with isothermal continuous and multistage stresses.

As the strain rate increased, the true stress also increased which is similar to the isothermal condition except at the true strain where the temperature decreased, the stress decreased to almost zero rapidly but recovered immediately. It was also interesting to find that the non-isothermal stresses were higher than both isothermal continuous and multi-stage stresses in the later passes (Figure 2.17(d)), and this difference increased with cumulative strain. No explanation of this phenomenon was provided in the paper.

2.6. Hot compression studies on non-cylindrical shapes of work piece

Cylindrical specimen geometry is the mostly commonly used geometry in hot compression tests reported in the literature. Besides the cylindrical specimen, there are some other different shapes for the compression test such as flange and taper which were shown earlier in Figure 2.6 and Figure 2.7 (Li et al., 2011). Khan and Baig (2011) studied the effects of strain-rate and temperature on the formability of AA5182-O aluminum alloy for a cubic specimen. To determine the material response at different temperatures and strain rates, quasi-static compression and tension experiments were performed at elevated temperatures 296 °K, 373 °K to 473 °K respectively. These high temperature experiments were performed at different strain-rates ranging from 10^{-4} s^{-1} to 1 s^{-1} . The stress and strain curve for both tension and compression test are shown in Figure 2.18 below.

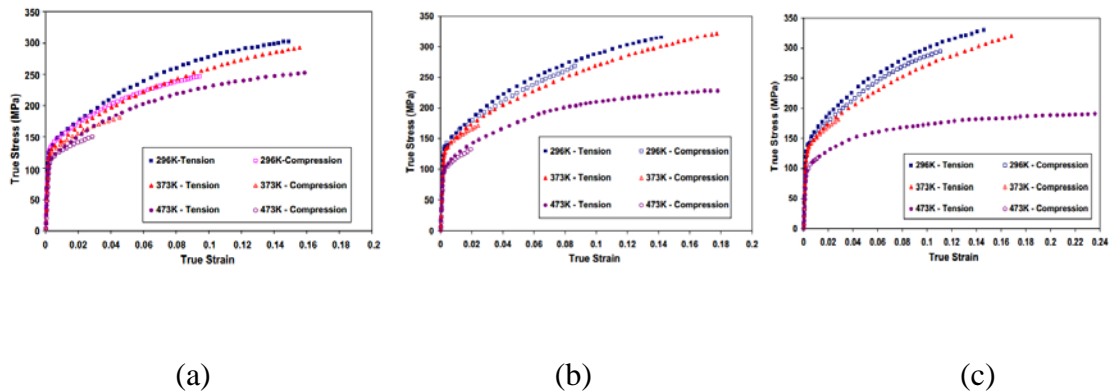


Figure 2.18. True stress and strain response of AA5182-O at strain rate (a) 1 s^{-1} , (b) 10^{-2} s^{-1} and (c) 10^{-4} s^{-1} along rolling direction (Khan and Baig, 2011).

Similar to the case of cylindrical specimens, Figure 2.16 indicates that the flow stress is not only dependent on temperature but also on strain-rate. However, there is a large tension compression asymmetry in the strain to fracture. Also, at the higher strain rates of 1 s^{-1} and 10^{-2} s^{-1} (see Figs. 2.18 (a, b)), there is a significant decrease in the elongation in compression as the temperature is increased. This is quite contradictory to the normal understanding from the studies on cylindrical specimens. However, no mechanistic explanation is provided in the paper regarding this anomaly.

2.7. Summary

After reviewing the previous research on hot compression of 7xxx aluminum alloys including AA7075 alloy, it can be said that many factors may affect the material flow and fracture in a compression test such as temperature, strain rate, material initial microstructure and crystallographic texture, specimen geometry, specimen loading with respect to material prior processing orientation, and isothermal or transient deformation conditions within the work piece. By studying the effect of these parameters, the hot compression process can be better understood. Most of the researchers have focussed on low strength aluminum, cylindrical specimens and isothermal condition during testing. The modeling of high strength AA7075 in hot compression is still quite new and no significant FE simulation work involving a suitable constitutive hardening model for this alloy is available in the literature. The study of compression behavior of AA7075 aluminum alloy in transient temperature is also a relatively new field. Thus, a study of the effect of isothermal and non-isothermal compression tests through lab-based experiments and FE

simulations may provide new knowledge that could be exploited in forming new shapes more efficiently. The hot compression of cubic specimens allows the orientation effects to be analyzed easily and readily. Also, the stress state and barrelling-type bulging in cubic compression is more complex. Therefore, a more comprehensive study of flow and fracture of such specimens may have applications in hot upsetting of similar shaped components.

Chapter 3. Experimental Methodology

3.1. Introduction

The experimental work is composed of continuous and some interrupted isothermal uniaxial hot compression tests as well as non-isothermal hot compression tests. The isothermal compression tests utilized specimens of cylindrical and cubic shapes which were compressed at several elevated temperatures, test speeds, two orientations with respect to the original as-received rolled plate direction, and two (artificially aged T6 and fully annealed O) tempers. The interrupt tests involved compression of only cylindrical specimens to several compression distances at specific temperatures and test speeds. The non-isothermal (i.e., transient temperature) compression tests were carried out on cylindrical and cubic specimens at different speeds immediately after applying a high current, via electrical resistance heating, over a very short duration. All deformed samples were sectioned, mounted, polished, etched, and observed with a metallurgical optical microscope to reveal the initial and deformed microstructures under different test conditions.

The experimental methodologies presented in this chapter include details of isothermal and non-isothermal mechanical test systems for uniaxial compression tests and details of the specimen preparation for optical microscopy work.

3.2. Test materials

The material studied for this research was a rolled AA7075 aluminum plate received in T6 temper condition with an initial length, width and thickness values of 305 mm, 305 mm and 19 mm respectively. Another AA7075-T6 rolled plate of smaller size and of 8 mm thickness was also purchased from the same supplier. The composition of AA7075 aluminum in weight percentage range are shown in Table 3.1.

Table 3.1. Chemical composition of AA7075 aluminum sheet (wt %).

AA7075-T6 plate	Al	Cu	Zn	Mg
	Bal	1.390	5.474	2.320

3.3. Machining of test cylindrical specimens

The cylindrical specimens were machined from the plate to 15 mm in height and 10 mm in diameter with axis of the cylinder along the rolling (RD) and transverse (TD) directions of the original plate. This was to analyze the effect of specimen orientation on flow stress behavior and deformation characteristics. The cylindrical specimen orientations with respect to the as-received plate are depicted in Figure 3.1.

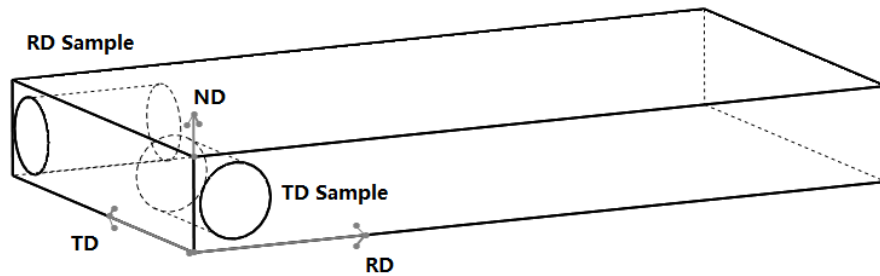


Figure 3.1. A schematic of RD and TD specimens machined from the plate.

The steps to obtain machined cylindrical test specimens consisted of the following; (i) cutting of a strip of about 11 mm width from the plate stock using a band saw while keeping the original length of the plate stock as such, (ii) creating a small conical groove on one side of the cut strip for centering the strip on a lathe, (iii) machining the strip into a cylinder of length 305 mm and diameter 10 mm, and (iv) cutting the long cylinder into shorter test specimen lengths of 16 mm with a band saw. A coolant was utilized to extract heat generated during machining so as to not alter microstructure of the material. Figure 3.2 presents photographs, from the left to right, of the cutting process using the band saw, cut strip from the plate stock, and its machining into a long rod on the lathe.



Figure 3.2. Cutting and machining of AA7075-T6 plate stock into cylinders for obtaining cylindrical test specimens.

The cubic specimens of 9 mm size were cut from the 9 mm thick AA7075-T6 plate by waterjet but with a small through-thickness region of each of the specimens still attached to the plate as shown in Figure 3.3. The samples were removed by gently tapping each of the specimens with a hammer to break them off from the plate. However, there was a small protrusion in the region of fracture (see the right image in Figure 3.3). A special sample holding fixture for polishing off the protrusion as well as the two compression surfaces was designed and fabricated in steel as shown in Figure 3.4 (side and top views of the fixture). Orientation of the cube with respect to the plate was clearly marked for each of the cubic specimens throughout the specimen preparation process.

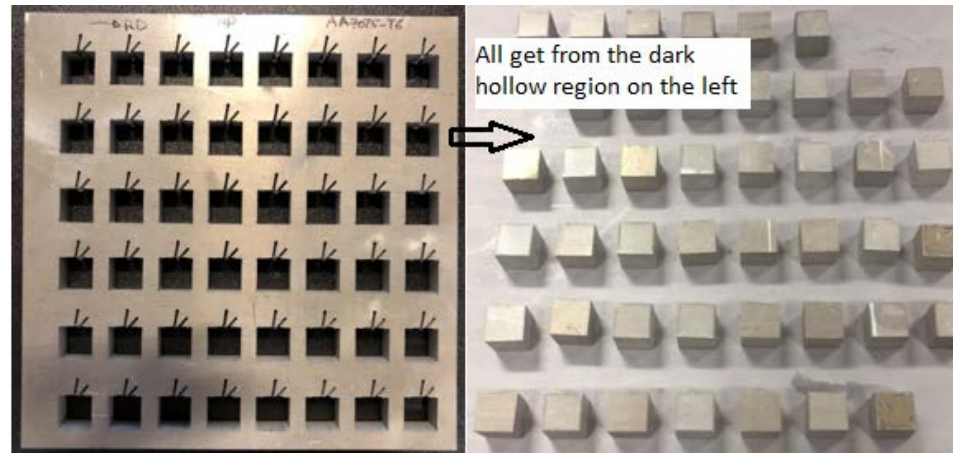


Figure 3.3. The aluminum plate stock after removal of the cubic specimens and the cubic specimens.

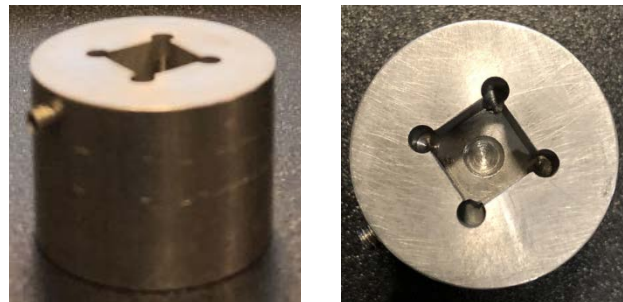


Figure 3.4. The side and top views for the cubic sample holder for polishing.

3.4. Heat treatment of test specimens

In order to study the effect of temper state on uniaxial compression characteristics, some of the as-received T6 temper cylindrical specimens were subjected to fully annealed (O) temper by heating them in a temperature-controlled furnace to solutionizing temperature of 480 °C for 3 hours, water quenching in cold water, then heating the samples to 413 °C for

3 hours and finally a furnace cool to room temperature. The furnace utilized for heat treatment is shown in Figure 3.5.



Figure 3.5. Furnace utilized O-temper specimens for heat treatments to attain.

3.5. Isothermal uniaxial compression tests

3.5.1. Mechanical test system

The mechanical test system consisted of a computer-controlled servo-hydraulic machine of 250 kN load capacity from MTS with a hydraulic actuator located at the bottom and below the base plate, and a load cell attached to the cross-head at the top. This system was fitted with an Instron environmental chamber between its two columns. The load train entered the environmental chamber from its top and bottom faces. The compression platens were mounted on the loading arms (see Figure 3.6).



Figure 3.6. MTS servo-hydraulic mechanical test system for hot uniaxial compression experiments. Image on the right shows the inside view of the environmental chamber with upper and lower loading arms. A cylindrical test specimen is also shown above the bottom compression platen.

The upper loading rod was cooled by circulating cold water through cooling channels to protect the load cell. For this purpose, the top of the upper bar was connected with the cooling tubes which were connected to the water supply. The lower loading rod was connected to the bottom compression platen which held the specimen during the compression test. In order to ensure that the specimen was positioned at the very center of the compression platen and aligned axially to the load train, centering fixtures for cylindrical and cubic specimen shapes were also designed and machined (see Figure 3.7). This fixture had a collar that matched the diameter of the upper rod.



Figure 3.7. Two different views of the fixtures for centering of the cylindrical and cubic specimens on the bottom compression platen.

3.5.2. Test parameters

A list of test parameters for the continuous isothermal uniaxial compression tests is presented in Table 3.2. The list includes two test specimen geometries, two material orientations, two tempers, 4 temperatures and 3 test speeds. A limited number of interrupted tests were conducted as shown in Table 3.3.

Table 3.2. Test parameters for isothermal compression tests.

Material	AA7075 aluminum
Orientation	Rolling direction and transverse direction
Geometry	Cylinder and cube
Temper	T6 and O-temper
Test speed (or initial strain rate)	0.00066 inch/s, 0.005 inch/s and 0.025 inch/s (0.0167 mm/s, 0.127 mm/s and 0.635 mm/s)
Temperature	RT, 100°C, 200°C and 300°C
Number of repeat tests	Duplicate tests at each the above test condition

Table 3.3. Test parameters for interrupted tests

Cylindrical specimen	Compression displacement		
AA7075-T6, RD, 0.005 inch/s (0.127 mm/s)	0.043 inch (1.09 mm)	0.086 inch (2.18 mm)	0.172 inch (4.36 mm)
	Compression temperature		
	RT		300 °C

3.5.3. Test procedure

3.5.3.1 Installation of compression platen and centering of the specimen

First, compression platen was installed on the lower loading rod. The test specimen with graphite lubrication film under its bottom surface was then placed on the compression platen. The graphite film was similarly placed on the top surface of the test specimen. The bottom rod was then manually moved up and closer to the fixed upper rod (also called punch rod) to adjust the distance between the upper rod and the compression platen to less than 1 inches. The centering fixture was then placed on the upper loading rod for centering of the specimen. Once centered, the fixture was removed.

3.5.3.2. Computer set-up, control and data acquisition

All tests were conducted at a constant test speed (or velocity) v . Since the speed is related to the strain rate by $v = \dot{\epsilon} \times H_0$, where H_0 is the initial height of the specimen, the strain rate increased to some extent as the specimen was compressed. Therefore, the initial strain rate, based on the initial height of the specimen and applied velocity, is utilized in the

present work as a basis of studying the effect of strain rate of flow stress-strain behavior of the material.

The data acquisition rate was first adjusted for tests carried out at different initial strain rates to keep the number of data points manageable. Table 3.4 shows the strain rates, data acquisition rate, test time in seconds, and the number of data points recorded during the test. Because of the stroke limit of the hydraulic actuator, the required compression displacement was estimated first to ensure safe operation of the test system. At lower temperature, the compression displacements of T6 and O temper cylindrical specimens prior to fracture could reach a maximum value of 0.172 in (4.36 mm) and 0.382 in (9.70 mm) respectively. Compression displacement of T6 cubic specimen, on the other hand, could reach up to 0.078 in (1.98 mm) only. The test times for the different test conditions are shown in Table 3.5 below.

Table 3.4. Hot compression test parameters.

Strain rate	Rate	Time (seconds)	Data points
0.00066 inch/s (0.0167 mm/s)	1 Hz	1500	1500
0.005 inch/s (0.127 mm/s)	10 Hz	100	1000
0.025 inch/s (0.635 mm/s)	100 Hz	100	10000

Table 3.5. Strain rates and test times for different tempers and specimen types.

Geometry		Cylindrical specimen		Cubic specimen	
Temper		T6	O	T6	
Test speed	Temperature		Time		
0.00066 inch/s (0.0167 mm/s)	RT	100 °C	260 s	579 s	118.2 s
0.005 inch/s (0.127 mm/s)	RT	100 °C	34.4 s	76.4 s	15.6 s
0.025 inch/s (0.635 mm/s)	RT	100 °C	7 s	15 s	3.12 s

Referring to Figure 3.6 (right), the test procedure consisted of moving the lower specimen holding platen upward to a proper position using the control software of the test machine while ensuring that the specimen has enough gap between its top surface and the upper rod. If the specimen is too close, any rise in the temperature of the specimen may lead to interference with the upper rod prior to the test.

3.5.3.3. Heating of the environmental chamber and sample testing

Once the computer-based test controller was set-up, the door of the environmental chamber was closed prior to heating the chamber. The chamber was set to the desired temperature with a remote-control device and the temperature was displayed on the digital panel on the chamber. The dwell time at the desired temperature was about 30 minutes for all tests to ensure attainment of uniform set temperature of all tooling and the test specimen. The compression platen was then manually moved up to bring the top surface of the specimen in contact with the upper compression rod. A small preload in the 100 – 150 lbf range was applied to the specimen to ensure contact of the specimen with the entire load train, prior to the test. The test program was then run from the dedicated computer to compress the

specimen. The compression load and displacement data were continuously recorded during the test. The specimen was observed from the quartz window of the environmental chamber. At the end of the test, the environmental chamber door was opened and the compression platen was lowered manually to remove the specimen. The same procedure was applied for interrupted tests except that the compression displacements were set to different values.

3.5.3.4. Data analysis

The raw data from the test was received in the form of continuously recorded load and displacement values. This data was converted into true stress versus true strain curves using the following well-known formulas:

$$\sigma_E(\text{MPa}) = \frac{P(N)}{A} \quad (3.1)$$

$$A = 0.25\pi D_0^2 \text{ (Cylindrical Specimen)} \quad (3.2)$$

$$A = a^2 \text{ (Cubical Specimen)} \quad (3.3)$$

$$\varepsilon_E = \frac{s}{H_0} \quad (3.4)$$

$$\sigma_T = \sigma_E \times (1 - \varepsilon_E) \quad (3.5)$$

$$\varepsilon_T = -\ln(1 - \varepsilon_E) \quad (3.6)$$

where σ_E , ε_E , σ_T , ε_T are engineering stress, engineering strain, true stress and true strain respectively. The remaining symbols, P , A , D_0 , a , s and H_0 are recorded load, area, diameter of cylindrical specimen, length of cubic specimen, displacement, initial height of cylindrical and cubic specimen respectively. Also, the elastic part of the data was truncated

to obtain true stress and corresponding true plastic strain values as material data input for use in the FE simulations of tests using ABAQUS software code. The details of the FE simulations are presented in Chapter 4.

3.6. Non-isothermal uniaxial compression tests

Non-isothermal tests uniaxial compression tests were also conducted on AA7075 cylindrical and cubic specimens in a laboratory built rapid electrical resistance heating and mechanical testing system (RHMT). Electrical resistance (or Joule) heating is a process in which electrical energy is converted to heat. The thermal energy is then used to heat the specimen to different temperatures depending upon the input current and time. This type of heating method is extensively used in spot welding applications. The electrical resistance system that uses large currents can provide enough electrical energy and turn it into thermal energy for rapid transient heating of small test specimens. The details of RHMT system in terms of its features, tool set configuration, test procedure and experimental data analysis are described in the sub-sections below.

3.6.1. Test system

The RHTM system was developed as part of a previous Master degree thesis in the research laboratory of Dr. Jain in JHE314. The various components of this system are shown in Figure 3.8 and Figure 3.9 respectively. The system in Figure 3.8 consisted of a mid-frequency Direct Current (MFDC) transformer and a cross bar attached to the transformer and a copper shunt. Two ends of the shunt were attached to the upper and lower electrodes. The uniaxial compression test specimen was placed between the two electrodes. The top electrode protruded from the top end of the copper shunt and acted as upper punch to compress the specimen. The bottom electrode was part of a base plate for placing the specimen. A high current of several thousand amperes was passed between the electrodes, through the test specimen, to heat it rapidly to high temperatures in a few seconds.

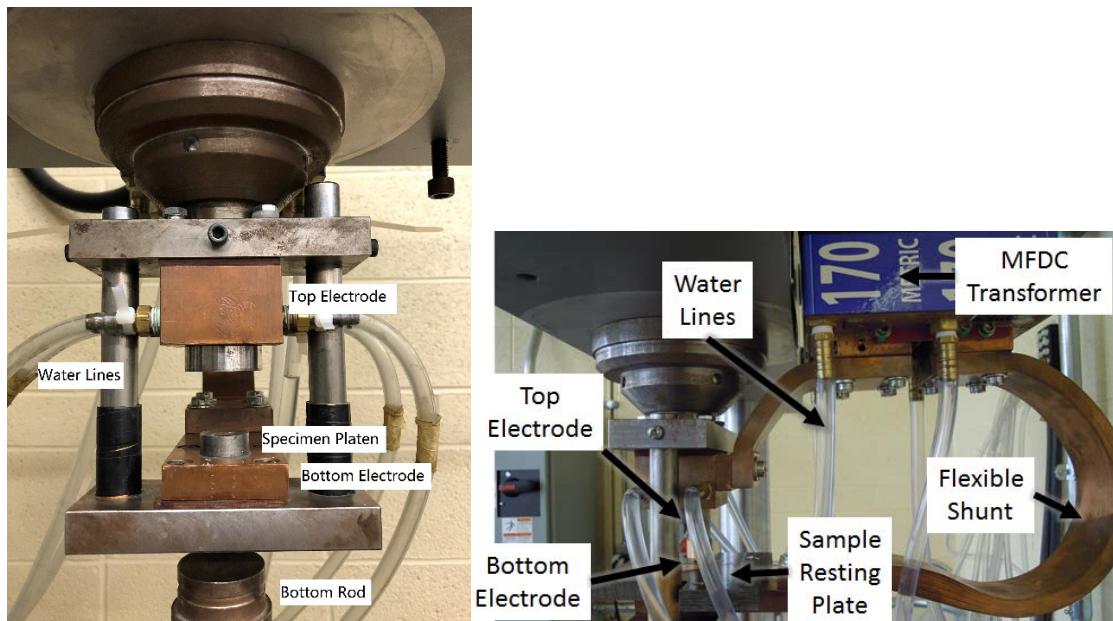


Figure 3.8 Front view and side view of the electrical resistance heating system.

The upper and lower electrodes were part of a test-jig which was placed in the mechanical test system (see Figure 3.9 below). This system consisted of a two-column mechanical testing frame fitted with computer controlled servo-hydraulic actuator from Instron, and equipped with a test controller and a data acquisition system. The test jig housed the upper and lower electrodes (and the bottom plate). This jig was rigidly fastened to the crosshead at the top of the mechanical test system. The lower electrode was attached to the bottom actuator and could be moved precisely up and down at various desired speeds to compress the test specimen to desired displacements and then to unload the specimen using the test controller and the computer interface. A recirculating water cooling system was also installed with the system so that after each test the system needed to be cooled down immediately to prevent overheating of the other attached components and consequent damage to the equipment. In fact, a hydraulic loop linking MFDC transformer, control unit, servo-hydraulic pump, and chiller was created, providing cooling water to all three devices.

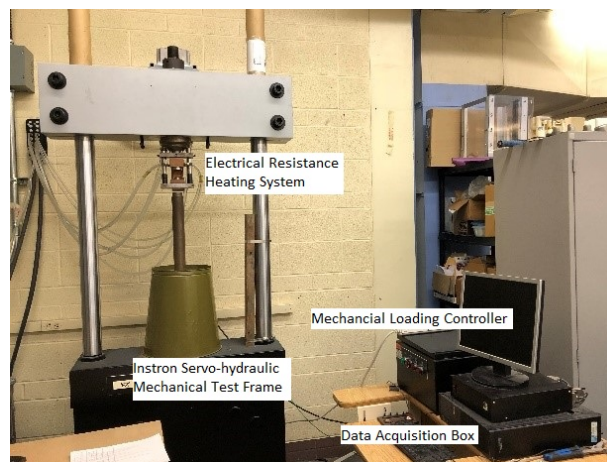


Figure 3.9. Mechanical test system.

The electrical resistance heating system was designed to provide currents up to 15 kA, where unit kA stands for kilo-amperes, over 1 second period. It could provide applied current profile in the form of a constant step, linearly increasing (ramp) current, and a time delay (with no applied current) between the profiles.

3.6.2. Test parameters

The uniaxial compression tests with the above set-up fall into the category of non-isothermal tests because the heating rate of the test specimen from high currents is very rapid and there is little time for heat diffusion to occur to reach a steady state temperature distribution within the test specimen in the duration of the test. The test parameters consisted of specimen geometry (cylindrical and cubic), the amplitude of the applied current and its duration and the test speed (see Table 3.6 below).

Table 3.6. Test parameters for non-isothermal compression tests.

Material	AA7075-T6
Specimen orientation	Transverse
Geometry	Cylinder, cube
Current	5 kA, 7.5 kA and 10 kA
Speed	3 mm/s, 5 mm/s and 10 mm/s

3.6.3. Test procedure

3.6.3.1. Installation of the test specimen in the test jig

The test specimen was first placed at the centre of the bottom steel plate and directly above the bottom electrode. The bottom actuator was then manually jogged upwards to establish contact with the upper electrode and to ensure that there was no gap between the test specimen and the bottom and upper electrodes. Any gap can lead to a large electrical discharge which will likely cause damage to the system.

3.6.3.2. Heating system set-up

Heating of the specimen depended on the applied electrical current and its duration which were both controlled. Three input currents values of 5 kA, 7.5 kA and 10 kA were chosen based on preliminary trial and error experiments. Since the current from the transformer was supplied at 60 Hz (or 60 cycles per second), the currents distribution over 3 second (i.e., 180 cycles) was programmed in the transformer. The compression test procedure was divided into 120 cycles of applied current as a ramp profile followed by dwell time of no current for 60 cycles. For instance, when the applied current was set at 5 kA, in first 120 cycles the current ramped from 0 to 5 kA in 2 seconds, and immediately dropped to zero for the last 1 second for the heat to dissipate within the specimen. This is illustrated in Figure 3.10 below.

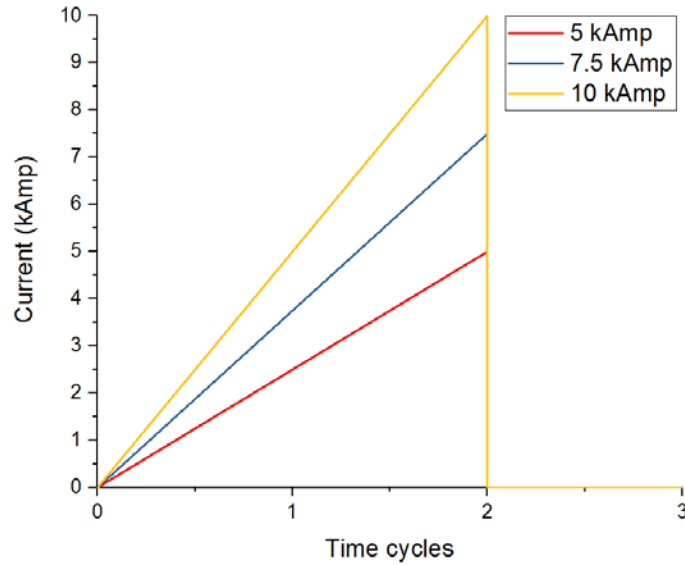


Figure 3.10. Applied current versus time profiles prior to compression testing.

3.6.3.3. Mechanical testing conditions

The uniaxial compression test was initiated instantly after the 3 second duration. The bottom actuator moved up at a constant speed to compress the heated specimen. The load and displacement data were continuously recorded using the data acquisition system and its interface with the computer. The actuator was immediately retracted after the test to remove the specimen from the test machine. The water cooling system was immediately activated once the loading of the specimen was completed. Three test speeds of 3 mm/s, 5 mm/s and 10 mm/s were chosen to assess the effect of speed on deformation behavior of AA7075-T6 specimens. At least two repeat tests were conducted for each condition.

3.6.3.4. Temperature measurement experiments

One of the limitations of the above experiments was that the temperature of the work piece could not be easily measured for each of the applied currents and test speeds for individual compression test specimens. The procedure would have required drilling holes on individual specimens and inserting a thermocouple at a desired location, possibly at the symmetric centre of the specimen, to measure the temperature in real time during the entire heating and mechanical testing period due to the transient nature of the process. This would have led to the destruction or significant damage to the thermocouple at the end of each test as the sample was subjected to large compressive strains. An alternative was thus chosen to simplify the temperature measurement process. A single specimen with a hole of diameter 1 mm at the mid-height location (axially) at the centre (radially) was fabricated. A closed fitting type K thermocouple (The response time is around 0.23 second) that was capable of measuring temperatures in the range -270-1260 °C from Omega Engineering company was installed in the hole and connected to a temperature acquisition unit from National Instruments (NI cDAQ-9174). The specimen with the thermocouple was then placed in the mechanical test system and various currents were applied to this specimen by bringing the top and bottom electrodes in contact with the specimen but without any compressive plastic loading (i.e., plastic deformation) of the specimen. The temperature – time history over a time period of 500 seconds was recorded. These results are presented in Chapter 5.

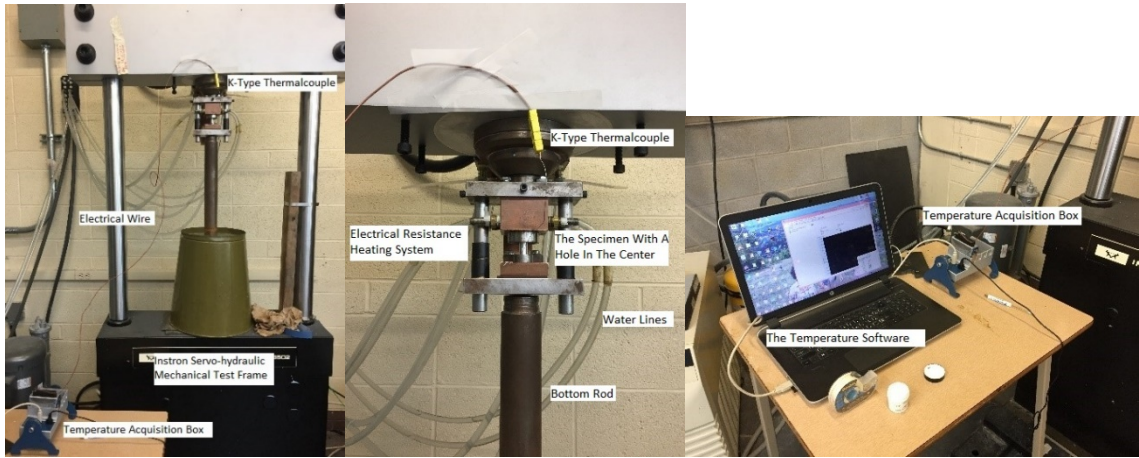


Figure 3.11. The specimen with the thermocouple as installed on the test system.

3.7. Optical metallography of test specimens

Optical micrographs of hot compressed specimens, as well as of un-deformed specimens, were obtained by preparing specimens by optical metallographic methods. The steps involved cutting, mounting, polishing and etching of each of the specimens using the equipment available at Centre for Automotive Materials and Corrosion (CAMC) at McMaster. The specimens were cut vertically through the cross-section to create two halves but as shown in Figure 3.12 below but only one of the two halves was mounted with the cut flat surface flush with the polishing surface.

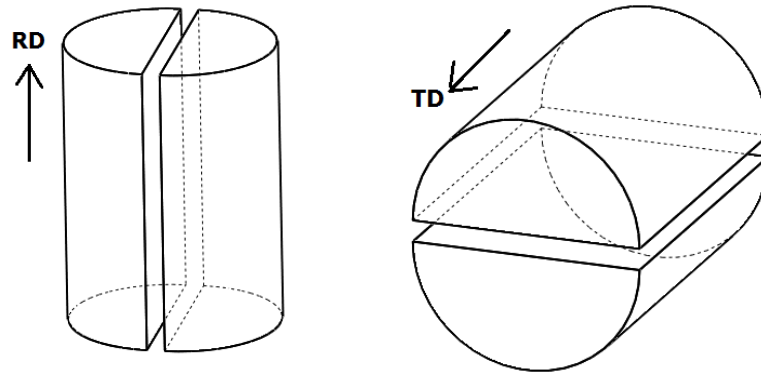


Figure 3.12. The cross-sections of the specimens

The half specimens were hot mounted in Bakelite polymer using a mounting machine. The mounted samples were manually polished first with sand paper of various grit sizes of smaller sand particles (#400, #800 and #1200) for about 1.5 minutes to sequentially eliminate surface scratches and any Bakelite residue on the surface from hot mounting. The polishing was then continued with an automatic rotary polishing system using $3\mu\text{m}$ and $1\mu\text{m}$ size colloidal silica suspension (OP-S) to completely eliminate all scratches over 3-5 minutes polishing period. The automated polishing procedure was repeated if the intermediate low magnification microscopic examination of the surface indicated presence of in the image of the fine polished surface. The polished specimens were cleaned and dried between steps to ensure no accidental transfer of the bigger polishing medium particles from one polishing step to another. Final polished scratch-free, mirror-like, specimens were etched with sodium hydroxide and nitric acid solutions as per the following procedural steps:

1. Mix in a container 10 grams of sodium hydroxide into 90 ml of distilled water.
2. Add 72.5 ml of nitric acid into 27.5 ml of distilled water in another container.
3. Heat the sodium hydroxide solution to a stable temperature of 60 °C by X Fisher IsoTemp equipment.
4. Place the specimen into sodium hydroxide container for 33 seconds and then wash with water to remove any residual solution from the surface.
5. Place the specimen into nitric acid container for about 5 seconds and then wash it with water and dry it with a blower.

The etched samples were placed in a desiccator for preservation of the surface prior to observing them under an optical microscope. Typically, a magnification of $200\times$ was selected to observe the grain structure and other macroscopic features of plastic flow in the specimens. Typically, various regions of the etched specimen such as center, top, left and diagonal and an overall image of the entire mounted specimen were recorded. Results of microstructural characterization of deformed samples are presented in Chapters 5.

Chapter 4. FE Simulation Methodology for Isothermal Uniaxial Compression Tests

4.1. Introduction

The finite element (FE) method is a useful numerical method for simulating metal forming processes including uniaxial compressive deformation and simple upsetting of metallic materials. The simulations can incorporate specimen and tool geometries, interfacial contact conditions and friction between tool and sheet, elastic and plastic strain, strain rate, and temperature dependent plastic properties of the deforming workpiece, as well as the elastic properties of the test platens and forming tools. The output data from the model such as stress and plastic strain contours from the entire specimen can help understand the material flow behavior, and formability (or workability) of the material in terms of deformation heterogeneity, flow localization and fracture characteristics at large strains. Also, by changing the simulation parameters in a systematic manner, such as specimen geometry, test speed, temperature of the work piece, tool-specimen friction and material properties of the material, one can analyze the role of different parameters on the process characteristics in a cost effective and efficient manner. However, the quality of the prediction from the simulations depends critically on the accuracy and applicability of the material model parameters as well as other process and numerical parameters.

In this chapter, aspects of the FE modeling methodology, material constitutive model, and other forming process parameters are described for elevated temperature uniaxial

compression of AA7075 aluminum cylindrical and cubic specimens. The FE simulation methodology will be discussed in terms of analyzing hot deformation characteristics, effect of material anisotropy and specimen fracture. The FE test simulation matrix is shown in Table 4.1 below.

Table 4.1. FE test simulation matrix.

Geometry, material and process parameters	Material Anisotropy	Hot deformation	Fracture
Cylindrical	√	√	√
Cubic	√	√	×
Orientation	TD and RD	TD and RD	RD
Temper	T6	T6 and O	T6
Temperature	RT	RT, 100 °C, 200 °C and 300 °C	RT
Test speed	0.005 inch/s (0.127mm/s)	0.00066 inch/s, 0.005 inch/s and 0.025 inch/s (0.0167 mm/s, 0.127 mm/s and 0.635 mm/s)	0.005 inch/s (0.127mm/s)

This chapter is divided into several sub-sections that cover details of the strain rate and temperature dependent material constitutive models, types of FE analysis, uniaxial compression specimen geometries used, FE element type and mesh characteristics, steel compression platen properties, test specimen contact definition, and selection of boundary conditions to accurately capture the loading of test specimens.

4.2. Material modeling

The AA7075 alloy can have a large range of elastic-plastic behavior at room and elevated temperatures depending upon its temper state, forming temperature, and strain rate, as discussed earlier in the literature review chapter. For the present FE modeling work, AA7075 aluminum alloy test specimens were considered in two different temper states (T6 and O). The material was treated as elastic and non-linear hardening plastic, whereas the steel compression platens were considered as rigid (i.e., un-deformable) as well as elastic in some cases. The elastic properties and density of AA7075 alloy are presented in Table 4.2.

Table 4.2. Elastic properties and density of AA7075 alloy used in the FE model.

Material	AA7075 Aluminum alloy
Young's Modulus	69000 MPa
Poisson's Ratio	0.33
Density	$2.7e-9$ ton/mm ³

4.2.1. Yield criterion

Since the as-received AA7075 aluminum alloy plate was in the as-rolled and T6 temper state, it was considered as anisotropic material in some of the simulations with a difference in anisotropic material property along rolling direction (RD) and transvers direction (TD). However, this difference was found to be relatively small and, for a large majority of the simulations, the effect of material anisotropy via an anisotropic yield criterion was not

considered, for simplification. The material was assumed to follow isotropic Mises yield criterion expressed mathematically as:

$$\sigma = \left[\frac{1}{2}(\sigma_1 - \sigma_2)^2 + \frac{1}{2}(\sigma_1 - \sigma_3)^2 + \frac{1}{2}(\sigma_3 - \sigma_2)^2 \right]^{\frac{1}{2}} \quad (4.1)$$

where σ_1 , σ_2 and σ_3 are three principal stresses.

For analyzing the effect of anisotropy of AA7075-T6 aluminum alloy, Hill quadratic yield criterion was utilized. This criterion in the generalized form can be written as:

$$F(\sigma_{22} - \sigma_{33})^2 + G(\sigma_{33} - \sigma_{11})^2 + H(\sigma_{11} - \sigma_{22})^2 + 2L\sigma_{23}^2 + 2M\sigma_{31}^2 + 2N\sigma_{12}^2 = 1 \quad (4.2)$$

$$F = \frac{R_0}{R_{90}(1+R_0)} \quad (4.3)$$

$$G = \frac{1}{1+R_0} \quad (4.4)$$

$$H = \frac{R_0}{1+R_0} \quad (4.5)$$

$$L = M = N = \frac{(R_{90}+R_0)(1+2R_{45})}{2R_{90}(1+R_0)} \quad (4.6)$$

where σ_{ij} are the stresses, R_0 , R_{45} , R_{90} are R-values, F, G, H, L, M, N are material constants that were obtained from the data reported in Table 4.3 below.

Table 4.3 (a). Values of R-values and F, G, H, L, M, N material constants. (Sciammarella et al., 2016)

R ₀	R ₄₅	R ₉₀
0.78	0.95	1.34

Table 4.3 (b). Values of F, G, H, L, M, N material constants.

F	G	H	L	M	N
0.33	0.56	0.44	1.29	1.29	1.29

4.2.2. Constitutive hardening law

Several different strain rate and temperature dependent plastic hardening laws were considered for FE modeling of elevated temperature uniaxial deformation of AA7075 alloy. These laws included Johnson-Cook (J-C), Arrhenius Equation model of Nasr et al., (2014), original Voce-Kocks (V-K) model as well as a recent modification of the V-K model by Dr. Xu. The J-C model is already implemented in ABAQUS/Standard FE code and was used as such. The mathematical expressions for J-C model are as follows:

$$\sigma = \left[A + B\varepsilon_p^n \right] \left[1 + C \ln \left(\frac{\dot{\varepsilon}}{\dot{\varepsilon}_0} \right) \right] \left[1 - T^{*m} \right] \quad (4.7)$$

$$T^* = \frac{T - T_{room}}{T_{melt} - T_{room}} \quad (4.8)$$

The experimental data from a range of test temperatures and test speeds were fitted to the above equation to obtain the constitutive parameters values for AA7075 alloy for J-C model. These are shown, as an example, in Table 4.4 below from Brar et al. (2009). The actual

parameter values from AA7075 alloy uniaxial compression tests in the present study are presented in Chapter 5.

Table 4.4. Constitutive material parameters for J-C model from Brar et al. (2009).

A (MPa)	B (MPa)	C	n	m	T _{melt} (°C)	T _{room} (°C)	$\dot{\epsilon}_0$
546	678	0.024	0.71	1.56	477	25	1

The expression for Arrhenius equation model is as follows:

$$\sigma = \frac{\arcsin h \left[\exp \left[\frac{RT [\ln \dot{\epsilon} - \ln A] + Q}{RTn} \right] \right]}{\alpha} \quad (4.9)$$

where $\ln A$, Q , n and α are considered as strain-dependent material parameters. As earlier, the experimental data from a range of test temperatures and test speeds was fitted to the above equation to obtain the constitutive parameters values for AA7075-T6 and O temper alloy for the Arrhenius equation model. Three cases were considered for the above equation involving various sub-sets of experimental data, (i) RT, 100 °C, 200 °C and 300 °C, (ii) 100 °C, 200 °C and 300 °C, and (iii) 200 °C and 300 °C only. The R square value of the fit to the above equation for stress, strain rate and temperature for the three cases were 0.800, 0.900 and 0.997 respectively. Fourth-order polynomial functions were utilized to describe the relationship between the parameters $\ln A$, Q , n , α and applied strain, and values of the coefficients were obtained by curve fitting.

In addition to J-C and Arrhenius equation models, Voce-Kocks (V-K) constitutive model from the literature was also studied for its applicability to represent the constitutive behavior of AA7075-T6 and O alloys. This model is mathematically expressed as:

$$\sigma = \sigma_s + (\sigma_0 - \sigma_s) \exp\left(-\frac{\varepsilon}{\varepsilon_r}\right) \quad (4.10)$$

$$\sigma_s = \sigma_{s0} \left(\frac{\dot{\varepsilon}}{\dot{\varepsilon}_{s0}}\right)^{\frac{kT}{A_s}} \quad (4.11)$$

$$\sigma_0 = \sigma_{k0} \left(\frac{\dot{\varepsilon}}{\dot{\varepsilon}_{k0}}\right)^{\frac{kT}{A_0}} \quad (4.12)$$

$$\varepsilon_r = \frac{\sigma_s}{\theta} \quad (4.13)$$

The nomenclature for the various symbols used in equations of V-K model is given in Table 4.5 below.

Table 4.5. Nomenclature of symbols in the original V-K constitutive equations.

Symbols	Parameters
σ	Flow stress
σ_s	Saturation stress
σ_0	Initial yield stress
ε	Plastic true strain
ε_r	Relaxation strain
σ_{s0}	Saturation threshold stress at 0 °K
$\dot{\varepsilon}$	Strain rate
$\dot{\varepsilon}_{s0}$	Saturation reference strain rate at 0 °K
k	Boltzmann constant
T	Temperature
A_s, A_0	Material parameters
σ_{k0}	Initial threshold stress at 0 °K
$\dot{\varepsilon}_{k0}$	Initial reference strain rate at 0 °K
θ	Work hardening rate

A non-linear least square curve fitting procedure similar to the J-C and Arrhenius models was employed for obtaining the material parameters of the V-K model. However, the results of the fit were poor in the lower temperature range, as in the case of the Arrhenius model. Therefore, a recently modified Voce-Kocks (V-K) constitutive model was also assessed for representing the constitutive hardening behavior of AA7075 alloy. The expressions for modified V-K model are:

$$\sigma = \sigma_s + (\sigma_0 - \sigma_s) \exp\left(-\frac{\varepsilon}{\varepsilon_r}\right) \quad (4.14)$$

$$\sigma_s = \sigma_{s0} \left(\frac{\dot{\varepsilon}}{\dot{\varepsilon}_{s0}}\right)^{\frac{kT}{C_1 \exp(C_2 T)}} \quad (4.15)$$

$$\sigma_0 = \sigma_{k0} \left(\frac{\dot{\varepsilon}}{\dot{\varepsilon}_{k0}}\right)^{\frac{kT}{C_1 \exp(C_2 T)}} \quad (4.16)$$

$$\varepsilon_r = \frac{\sigma_s}{\theta} \quad (4.17)$$

The nomenclature for the various symbols used in equations of modified V-K model is given in Table 4.6 below.

Table 4.6. Nomenclature of symbols in the modified V-K constitutive equations.

Symbols	Parameters
σ	Flow stress
σ_s	Saturation stress
σ_0	Initial yield stress
ε	Plastic true strain
ε_r	Relaxation strain
σ_{s0}	Saturation threshold stress at 0 °K
$\dot{\varepsilon}$	Strain rate
$\dot{\varepsilon}_{s0}$	Saturation reference strain rate at 0 °K
k	Boltzmann constant
T	Temperature
C_1 and C_2	Additional fit Parameters

Table 4.6. Continued...

σ_{k0}	Initial threshold stress at 0 °K
$\dot{\epsilon}_{k0}$	Initial reference strain rate at 0 °K
θ	Work hardening rate

The modified V-K model was found to fit the experimental true stress and plastic true strain data better compared to the Arrhenius equation model and Johnson-Cook model over the entire test temperature range. Arrhenius equation model provided good fit to data only in the temperature range 200 °C – 300 °C.

The Arrhenius equation model and modified V-K constitutive plastic hardening models used in this study were not available in ABAQUS program. Fortunately, ABAQUS program allows the user to implement an appropriate constitutive equation for the material of interest using a separate Fortran subroutine, called UMAT. The input variables of materials properties and the state variables in the UMAT subroutine for Arrhenius equation model and modified V-K model are listed in Tables 4.7 and 4.8.

Table 4.7. Input variables in UMAT subroutine (a) Arrhenius equation model (b)

Modified V-K model

(a) Arrhenius equation model

Input Variables	Descriptions
PROPS (1)	Young's modulus
PROPS (2)	Poisson's ratio
PROPS (3-7)	Q, 4th order polynomial fit (0-4)
PROPS (8-12)	N, 4th order polynomial fit (0-4)
PROPS (13-17)	ln(A), 4th order polynomial fit (0-4)
PROPS (18-22)	α , 4th order polynomial fit (0-4)

(b) Modified V-K model

Input Variables	Descriptions
PROPS (1)	Young's modulus
PROPS (2)	Poisson's ratio
PROPS (3)	Saturation stress at 0 °K
PROPS (4)	Saturation reference strain rate at 0 °K
PROPS (5)	Parameter C_1
PROPS (6)	Parameter C_2
PROPS (7)	Initial threshold stress at 0 °K
PROPS (8)	Initial reference strain rate at 0 °K
PROPS (9)	Parameter C_1
PROPS (10)	Work hardening rate
PROPS (11)	Test temperature
PROPS (12)	Test strain rate

Table 4.8. State variables in VUMAT subroutine (a) Arrhenius equation model (b)

Modified V-K model.

(a) Arrhenius equation model

State Variables	Descriptions
STATEV (1)	Equivalent strain
STATEV (2)	Equivalent plastic strain rate
STATEV (3-8)	Plastic strains (all 6 components)
STATEV (9)	Equivalent plastic strain
STATEV (10)	Current yield stress
STATEV (11)	Equivalent stress
STATEV (12-17)	Elastic strains (all 6 components)

(b) Modified V-K model

State Variables	Descriptions
STATEV (1)	Equivalent strain
STATEV (2)	Equivalent plastic strain rate
STATEV (3-8)	Plastic strains (all 6 components)
STATEV (9)	Equivalent plastic strain
STATEV (10)	Current yield stress
STATEV (11)	Equivalent stress
STATEV (12-17)	Elastic strains (all 6 components)
STATEV (18)	Saturation stress
STATEV (19)	Initial yield stress
STATEV (20)	Equivalent strain increment

A comparison of results from these three models (J-C, Arrhenius and modified V-K) will be presented in Chapter 5.

4.2.3. Ductile fracture models

For analyzing fracture characteristics of uniaxial compression specimen, two different types of models were considered, Gurson-Tvergaard-Needlemen (GTN) damage model and Tresca fracture model. These two types of models are discussed below.

4.2.3.1. GTN ductile damage model

The GTN damage model is already implemented in ABAQUS/Explicit FE code. This model is mathematically expressed as:

$$\Phi = \left(\frac{\sigma_{eq}}{\sigma_y}\right)^2 + 2q_1 f^* \cosh\left(1.5q_2 \frac{\sigma_h}{\sigma_y}\right) - (1 + q_3 f^{*2}) = 0 \quad (4.18)$$

$$\text{where } f^* = \begin{cases} f & f \leq f_c \\ f_c + \frac{1-f_c}{f_f-f_c}(f-f_c) & f_c \leq f \leq f_f \end{cases} \quad (4.19)$$

where σ_{eq} is equivalent stress, σ_y is yield stress, σ_h is hypostatic stress, q_1 q_2 and q_3 are parameters of the GTN damage model, f^* is a function of void volume fraction f as shown above in eqn. 4.18, the void coalescence and the material fracture are considered to take place when the void volume fractions reach critical values of f_c and f_f respectively. The evolutions of the two void volume fractions f_c and f_f are driven by the growth of existing voids and the nucleation of new voids as follows:

$$\Delta f = \Delta f_{growth} + \Delta f_{nucleation} \quad (4.20)$$

$$\Delta f_{growth} = (1-f)\Delta\bar{\epsilon}^p \quad (4.21)$$

$$\Delta f_{nucleation} = B\Delta\bar{\varepsilon}^p \quad (4.22)$$

$$B = \frac{f_n}{s_n\sqrt{2\pi}} \exp\left[-\frac{1}{2}\left(\frac{\bar{\varepsilon}^p - \varepsilon_n}{s_n}\right)^2\right] \quad (4.23)$$

where $\Delta\bar{\varepsilon}^p$ is the increment of equivalent plastic strain, f_n is the void volume fraction of void nucleating particles, s_n is the standard deviation and ε_n is the mean nucleating strain. The parameters of GTN damage model for AA7075 alloy are shown in Table 4.9 below from Zhu et al. (2017) shows the GTN parameters obtained from uniaxial tension tests.

Table 4.9 Parameters of GTN damage model for AA7075 alloy from Zhu et al. (2017).

q_1	q_2	q_3	f_n	ε_n	s_n	f_c	f_f
1.5	1	2.25	0.01	0.3	0.1	0.15	0.25

4.2.3.2. Tresca fracture model

Tresca fracture criterion was selected as the most promising one based on its wide applicability in predicting fracture under shear mode of deformation (Jain et al., 1999). The Tresca fracture criterion is expressed as:

$$\tau_{max} = C \quad (4.24)$$

where τ_{max} is the maximum shear stress, C is a material constant. However, Tresca fracture criterion is not implemented in ABAQUS/Explicit library. Therefore, a VUMAT user subroutine, developed by Dr. Xu in our research group, was utilized. The input

variables of materials properties and the state variables in the VUMAT subroutine for Tresca fracture criterion are listed in Tables 4.10 and 4.11 respectively.

Table 4.10. Input variables in VUMAT subroutine for Tresca fracture criterion.

Input Variables	Descriptions
PROPS (1)	Young's modulus
PROPS (2)	Poisson's ratio
PROPS (3)	Initial threshold stress at 0 °K
PROPS (4)	Initial reference strain rate at 0 °K
PROPS (5)	Parameter C ₁
PROPS (6)	Parameter C ₂
PROPS (7)	Saturation stress at 0 °K
PROPS (8)	Saturation reference strain rate at 0 °K
PROPS (9)	Parameter C ₁
PROPS (10)	Work hardening rate
PROPS (11)	Constant of Tresca rule
PROPS (12)	Temperature
PROPS (13)	Reference strain rate

Table 4.11. State variables in VUMAT subroutine for Tresca fracture criterion.

State Variables	Descriptions
STATEV (1)	Equivalent plastic strain
STATEV (2)	Strain rate
STATEV (3)	Element deletion
STATEV (4)	Principle shear stress
STATEV (5)	Hydrostatic stress
STATEV (6)	Yield strength
STATEV (7)	Plastic strain increment

4.3. Analysis type

ABAQUS/Standard FE code (version 6.14) was utilized for all FE simulations of uniaxial compression tests. ABAQUS/Standard employs solution procedure ideal for static and low-

speed dynamic events where accurate stress solutions are critically important. ABAQUS/Standard offers several material models and has a robust capability for solving the contact problem. ABAQUS/Standard is also more efficient for solving the smooth non-linear problem. The UMATs for Arrhenius equation model and modified V-K model were thus written for ABAQUS/Standard code.

ABAQUS/Explicit FE code (version 6.14) was utilized for the FE simulation of the fracture in uniaxial compression tests, ABAQUS/Explicit is more efficient for the high speed (short duration) dynamic problems (i.e., fracture problem). Also, it does not require as much disk space as ABAQUS/Standard for large problems, and it often provides a more efficient solution for large deformation problems involving contact such as in uniaxial compression tests. Therefore, VUMAT sub-routine was developed in ABAQUS/Explicit for the Tresca fracture criterion. The FE code selection for each condition is shown in Table 4.12 below.

Table 4.12. ABAQUS FE code selection

Sample geometry	Hot deformation	Anisotropy	Fracture	
			GTN	Tresca
Cylinder	ABAQUS/Standard 6.14	ABAQUS/Explicit 6.14	ABAQUS/Explicit 6.14	
Cube	ABAQUS/Standard 6.14	ABAQUS/Explicit 6.14	N/A	

4.4. FE model geometry

Since the cylinder and cube were both axisymmetric with respect to the loading axis, only one eighth of the specimen with appropriate symmetry boundary conditions was needed for the simulation to shorten the analysis time. The dimension of one quarter cylindrical specimen is a quadrant with a radius of 5 mm and a height of 15 mm and one quarter cubic specimen is a square with a side length 4.5 mm and a height of 9 mm. Although the specimen is axisymmetric to all axis, but for observing the fracture process better, one quarter model is built for the final simulation. The two geometries of the FE model are shown in the Figure 4.1 below:

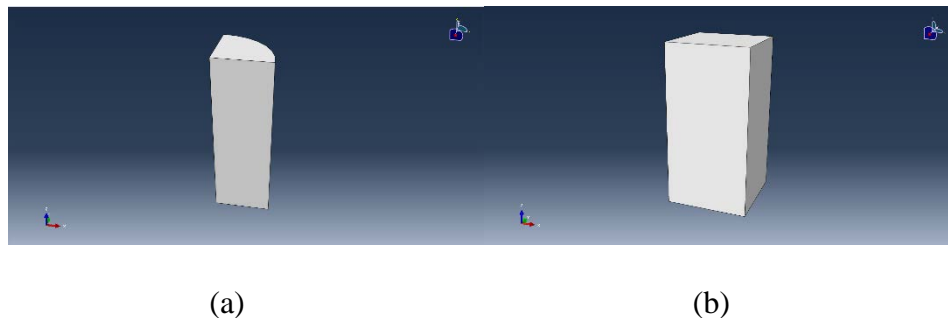


Figure 4.1. One quarter models of, (a) cylindrical, and (b) cubic, specimens.

A steel bottom compression platen attached to the lower rod and an upper rod were utilized in the experiment for applying the load to the upper and bottom surfaces of the test specimen to carry out the uniaxial compression test. However, in the FE model, bottom platen and upper rod were simplified as two un-deformable (rigid) surfaces. The benefit of treating the tools as rigid surfaces was to reduce the calculation of nodes and elements associated with the tools, so that the computational time could be reduced.

4.5. Contact definition

ABAQUS/Standard provides two algorithms for modeling contact, one is a general contact algorithm and the other considers the contacting surfaces as a ‘contact pair’. General contact algorithm typically includes all bodies in the model and has few restrictions on the type of the surfaces involved which is sufficient for the uniaxial compression test simulation. Figure 4.2 shows the top and bottom surfaces of the cylindrical specimen in contact with the top and bottom rigid surfaces.

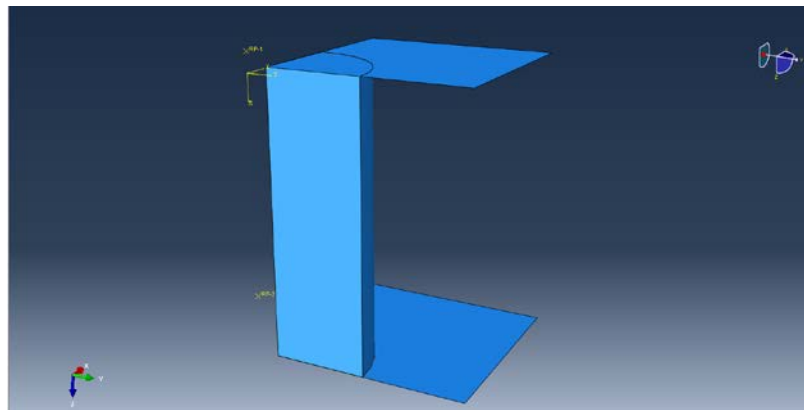


Figure 4.2. The contact surfaces of cylindrical specimen.

In the FE model of isothermal uniaxial compression test, the contact interaction occurs only between the surface of specimen and rigid body. The friction coefficient (μ) between the specimen and platen surfaces is an important property in this interaction. In fact, the barreling effect in cylindrical upsetting is related to the friction coefficient. However, the friction coefficient could not be measured experimentally. Therefore, a geometric analysis

proposed by (Lin et al., 2010) was utilized to obtain the value of μ from dimensions of the compressed specimen as follows:

$$\mu = \frac{\left(\frac{R}{h}\right)b}{\left(\frac{4}{\sqrt{3}}\right) - \left(\frac{2b}{3\sqrt{3}}\right)} \quad (4.25)$$

where

$$b = 4 \frac{\Delta R h}{R \Delta h} \quad (4.26)$$

$$\Delta R = R_M - R_T \quad (4.27)$$

$$R_T = \left(3 \frac{h_0}{h} R_0^2 - 2R_M^2\right)^{\frac{1}{2}} \quad (4.28)$$

and

$$\Delta h = h_0 - h \quad (4.29)$$

The geometric parameters in the above equation are shown in the un-deformed and deformed specimen geometries in Figure 4.3 where the parameters R_0 , R_M , h_0 and h can be directly measured from the initial and compressed specimen geometries.

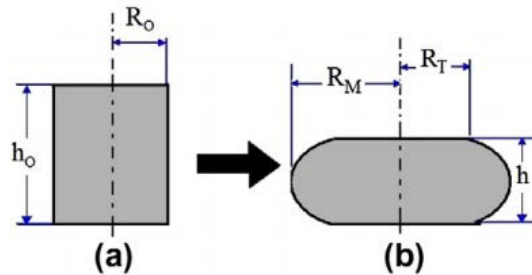


Figure 4.3. Cylindrical specimen geometry, (a) before compression, and (b) after compression.

Working through the equations 4.25-4.29 in the reverse manner, an average friction coefficient μ could be easily determined. The value of friction coefficient μ was in the range of 0.10-0.13.

4.6. Model boundary conditions

Proper application of boundary conditions is important for capturing the experimental compression characteristics in the FE model. Five different boundary conditions were applied to the model as shown in Figure 4.4 for the cylindrical specimen geometry, two for the side boundary of the rigid surfaces, two for the side faces of the specimen and one for the rigid point that causes the upper compression surface to move downward uniformly to compress the specimen.

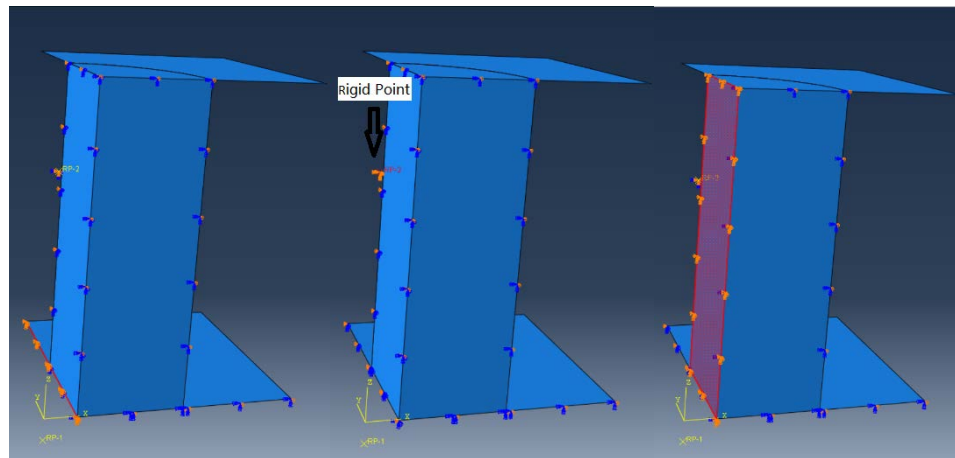
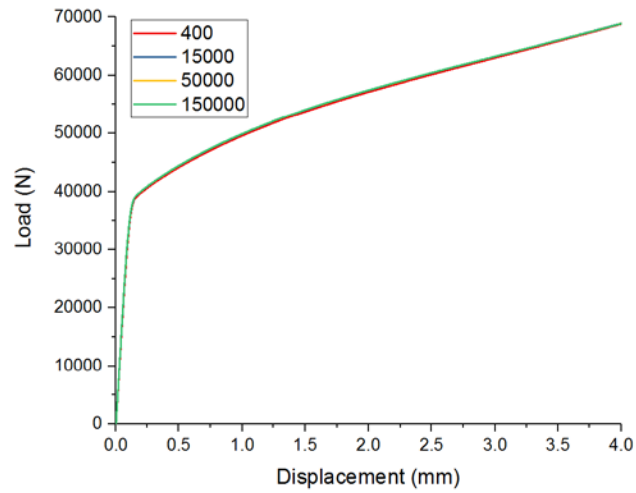


Figure 4.4. Sketches illustrating the different boundary conditions for the FE model of uniaxial compression of a cylindrical specimen.

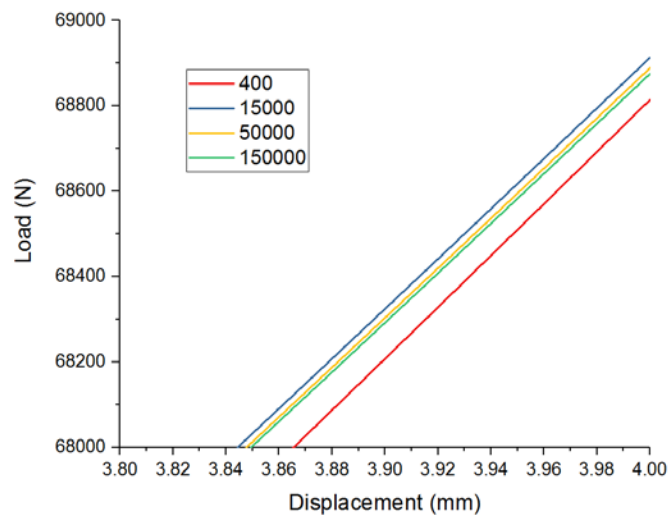
The X-axis was fixed ($XS_{YMM}=0, U_1=UR_2=UR_3=0$) along the side boundary of rigid surface and side faces of specimen in the Y-Z plane. Similarly, the Y-axis was fixed ($YS_{YMM}=0, U_2=UR_1=UR_3=0$) along the side boundary of rigid surface and side faces of specimen in the X-Z plane. The rigid point was fixed, and, thus considered all degree of freedoms to be zero ($U_1=U_2=U_3=UR_1=UR_2=UR_3=0$).

4.7. Meshing

The mesh density can affect the accuracy of the results and the computation time. If the density is too low the result is less accurate and mesh-dependent, and if the density is too high the computational time can be prohibitive and gain in accuracy may be only marginal. After trying several different mesh densities to represent the specimen geometry, an appropriate mesh size of 0.2 mm for each side was selected. This resulted in 50,000 elements in total for the quarter model and computation time per simulation was about 45 minutes. An 8-node linear brick element, C3D8, often utilized for finite strain plasticity problems in ABAQUS was chosen for the model. A comparison of the effect of mesh density on the simulated load versus displacement plots is shown in Figure 4.5(a,b) below.



(a) Complete load-displacement curves.



(b) Partial load-displacement curves.

Figure 4.5. Model load-displacement curve from different number of elements, (a) complete curves, (b) partial curves in the 3.8 mm - 4 mm displacement range.

According to the Figure 4.5 (b), for a mesh with 50000 C3D8 elements, the result is more accurate and the computational time is reduced by half compared to case with 150000 elements. Therefore, 50000 element model was chosen for all simulations. For the rigid surface, the mesh density did not affect the simulation results and computational time. Therefore, to shorten the simulation time, a coarse mesh was utilized for the rigid surface. A 4-node 3-D bi-linear rigid quadrilateral (R3D4) element was chosen to represent such surfaces. The two element types and the final mesh are shown in Figure 4.6 and Figure 4.7 respectively.

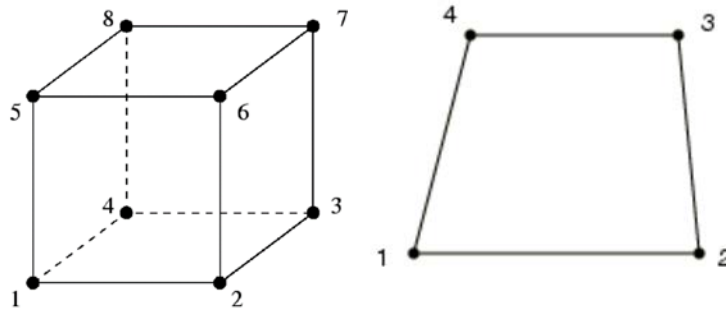


Figure 4.6. 3D solid element C3D8 and 2D element R3D4 shapes in ABAQUS FE code.

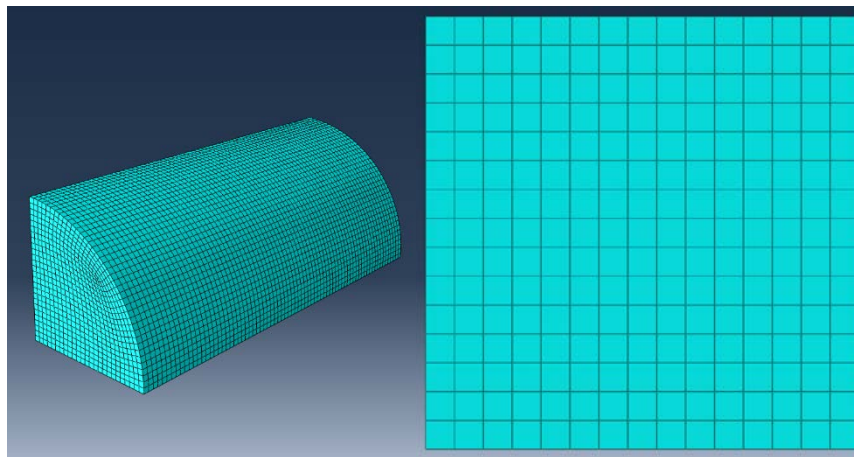


Figure 4.7. Mesh densities of the cylindrical specimen and rigid platen surface.

4.8. Summary

All aspects of FE modeling methodology covering constitutive material and fracture models and their implementation into ABAQUS/Standard and ABAQUS/Explicit FE codes using UMAT VUMAT subroutines respectively as well as contact definition, boundary condition, friction and mesh considerations were presented in this chapter. Consequently, reliable and robust FE models of uniaxial compression tests were obtained for comparison with the laboratory-based experiments. The modified V-K model was considered as the best material hardening model amongst those studied in the present work. This model was utilized to simulate the elevated temperature uniaxial compression experiments. Experimental and FE simulation results are presented in the next chapter.

Chapter 5. Results and Discussion

This chapter presents all of the results of the research work and a discussion of the results. The results are arranged as follows. The experimental uniaxial compression results under isothermal conditions are presented first. This is followed by similar experimental results of uniaxial compression tests under non-isothermal conditions. The next section deals with low magnification photographic images and optical microscopic observations of the flow behavior of the post-test isothermal test specimens. Experimental results are then followed by FE simulation results of the isothermal uniaxial compression test results in an effort to assess the model predictions based on different material constitutive laws of plastic strain hardening and ductile fracture models. A comparison of the experimental and FE model results as well as additional characteristics of material flow behavior from the FE models are presented. A brief summary of the results is presented in the last section.

5.1. Isothermal uniaxial compression experiments

Table 3.2 and 3.3 in Chapter 3 earlier presented the experimental test matrix that was utilized for isothermal uniaxial compression experiments. The specimens were typically stopped prior to fracture and a few interrupted tests were also conducted to observe the intermediate shapes of the specimen and to analyze the material flow characteristics in the intermediate stages of deformation. The results are presented in the form of true stress versus true strain curves. The results from the cylindrical specimens are presented first and then those from the cubic specimens.

5.1.1. Effect of temperature

Figures 5.1 and 5.2 show the effect of temperature on the shape of the true stress - true strain curves for T6 temper cylindrical samples tested along original RD and TD plate directions at a test speed of 0.005 inch/s (0.127 mm/s) respectively. Similar results for the O temper cylindrical samples tested along RD direction are shown in Figure 5.3. The curves show a linear elastic region at first, followed by onset of yielding and plastic flow up to large plastic strains. The general shapes of the all strain curves are consistent with those reported in the literature for uniaxial compression of AA7075 alloy at elevated temperatures (Wang et al., 2012). For example, the plastic region exhibits strain hardening which is more pronounced at lower temperatures (RT and 100 °C) but the work hardening rates and flow stress drop significantly at the two higher temperatures (200 °C and 300 °C). In fact, a saturation in stress can be seen from T6 temper specimens in both RD and TD orientations (see Figures 5.1 and 5.2) at 200 °C and a slight drop in flow stress at 300 °C (negative work hardening rate). The results of T6 temper alloy suggest that test temperature of 200 °C offer a good combination of strength and ductility. The O-temper specimens also exhibited trends similar to those exhibited by T6 sample with a few specific differences. First, the O-temper state resulted in significantly lower flow stress at RT and 100 °C compared to the T6-temper. The stress dropped considerably at 300 °C but still remained lower than the T6 temper state. Second, an important feature of the stress-strain curves for the O-temper alloy was that the strain of about 0.6 could be achieved at all test temperatures.

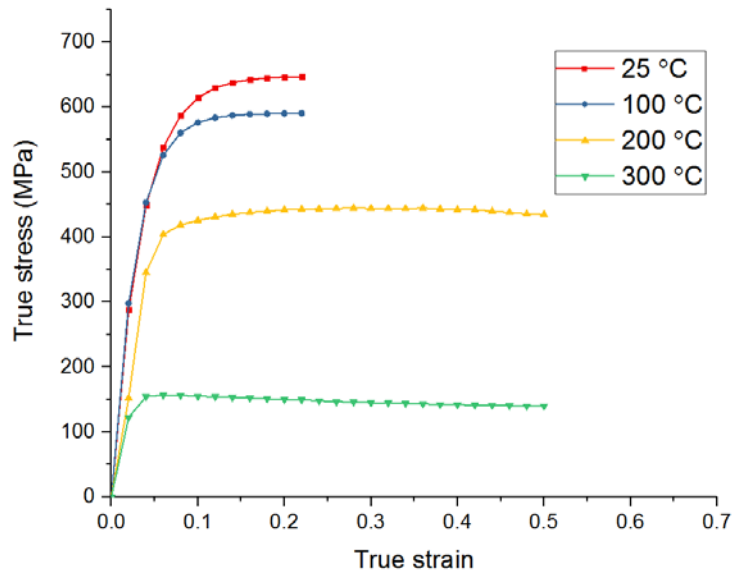


Figure 5.1. Effect of temperature on true stress versus true strain curves (Test speed: 0.005 inch/s (0.127 mm/s), temper: T6, orientation: RD, geometry: cylinder).

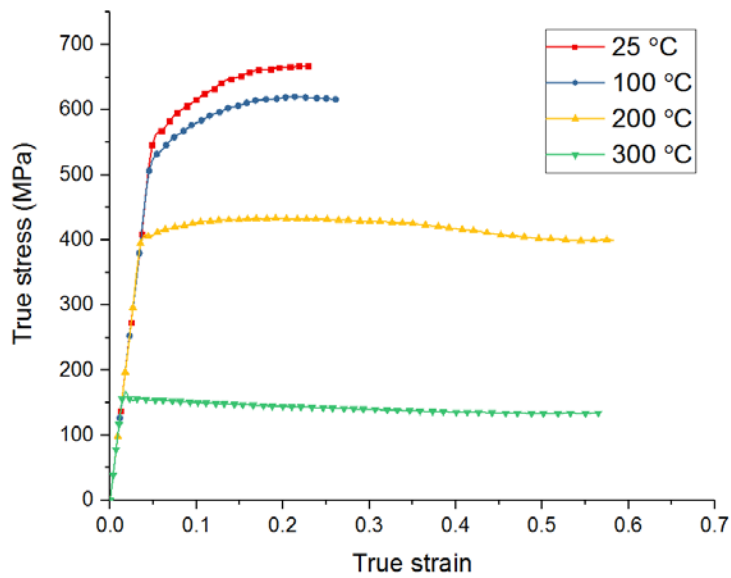


Figure 5.2. Effect of temperature on true stress versus true strain curves (Test speed: 0.005 inch/s (0.127 mm/s), temper: T6, orientation: TD, geometry: cylinder).

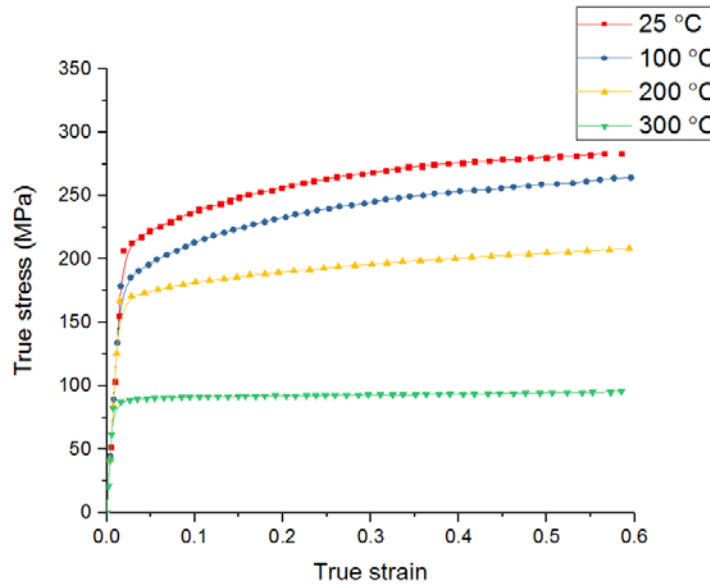


Figure 5.3. Effect of temperature on true stress versus true strain curves (Test speed: 0.005 inch/s (0.127 mm/s), temper: O temper, orientation: RD, geometry: cylinder).

The above trends in the stress-strain with respect to test temperature are consistent with the general understanding of the physical mechanisms that operate in high strength aluminum alloys. As reported in the literature, higher temperatures provide higher mobility to the grain boundaries for the nucleation and growth of dynamically recrystallized grains. Increased temperature also aids the dislocation annihilation mechanism, and thus reduces the flow stress level (Zhang et al., 2007). Both of these phenomena are temperature and time dependent. Dynamic recrystallization leading to strain softening is expected to be more pronounced in the higher strength T6 temper state compared to the O temper state. The dislocation mechanisms involve both dislocation multiplication leading to strain hardening as well as dislocation annihilation which results in a reduction in flow stress. At

lower temperatures, the dislocation hardening kinetics is predominant whereas at higher temperatures, more dislocation annihilation is expected from dynamic recovery and dynamic recrystallization processes.

5.1.2. Effect of speed

Figures 5.4 - 5.6 show the true stress and true strain curves at three different test speeds (0.00066 inch/s (0.0167 mm/s), 0.005 inch/s (0.127 mm/s) and 0.025 inch/s (0.635 mm/s)) for T6 RD, T6 TD and O temper RD orientation cylindrical test samples respectively. The results indicate rather small effect of test speed at lower temperatures (RT and 100 °C) for both temper states (T6 and O) as well as for the two orientations (RD and TD). However, the stress-strain curves rise rapidly with test speed at 200 °C and 300 °C for both tempers. For the T6 temper alloy, the effect of test speed was particularly pronounced in the RD samples at the two elevated temperatures. This could be attributed to texture anisotropy of the rolled T6 plate from which the test samples were obtained. The RD orientation O-temper specimens exhibited rather similar strain rate response to the TD orientation T6 specimens

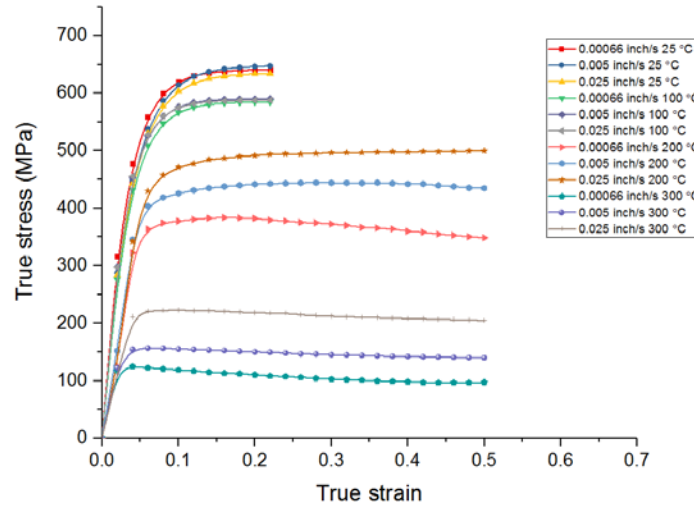


Figure 5.4. Effect of test speed on true stress versus true strain curves (Temper: T6, orientation: RD, geometry: cylinder).

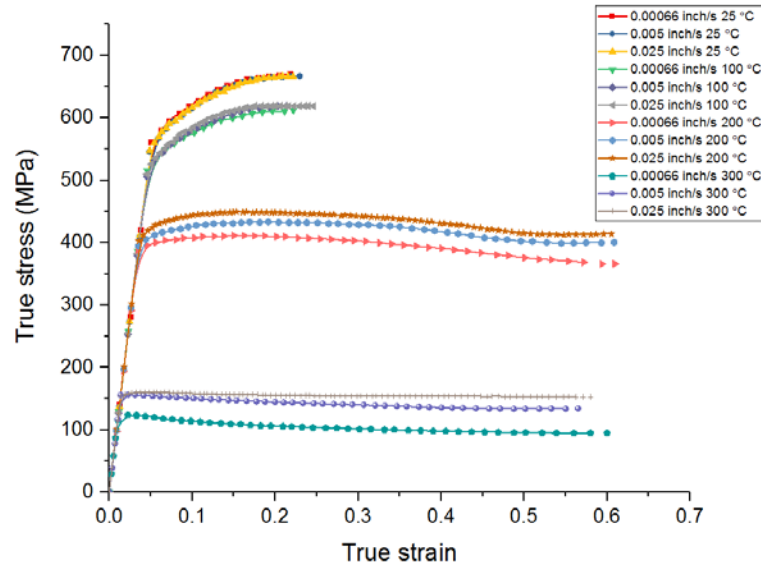


Figure 5.5. Effect of test speed on true stress versus true strain curves (Temper: T6, orientation: TD, geometry: cylinder).

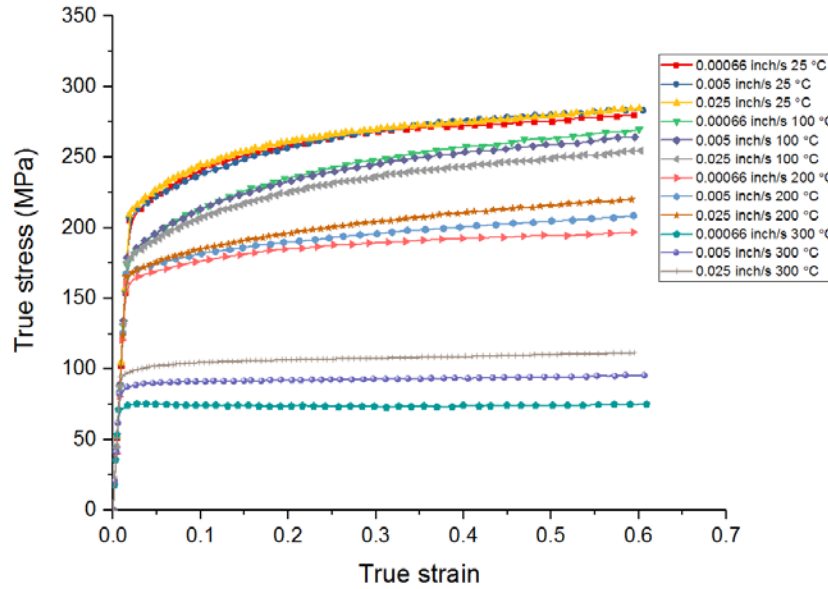


Figure 5.6. Effect of test speed on true stress versus true strain curves (Temper: O, orientation: RD, geometry: cylinder).

It is to be noted that strain rate sensitivity of aluminum alloys in general is both strain rate and temperature dependent. The strain rate sensitivity attains an optimum value in a specific elevated temperature and strain rate range depending upon the alloy composition and initial microstructure (the latter affects the grain rotation, grain boundary diffusion and grain boundary sliding mechanisms) and deformation induced changes to the microstructure at elevated temperature such as strain induced grain growth.

5.1.3. Effect of orientation

The above true stress and true strain curves for AA7075-T6 for different orientations (RD and TD) were replotted at various temperatures. These are shown in Figure 5.7 below to

clearly observe the effect of orientation. In general, the two orientations yielded very similar stress-strain curves under identical temperatures and strain rates. However, at lower temperatures (RT and 100 °C) the TD orientation exhibits slightly higher flow stress curves compared to the RD orientation. Small differences in flow stress observed at lower temperatures are likely a result of different grain size and crystallographic texture differences in the two different orientations which result in the activation of different slip systems during plastic compression. As more slip systems become operative at elevated temperatures, the texture anisotropy is reduced and the anisotropy of flow stress is eliminated.

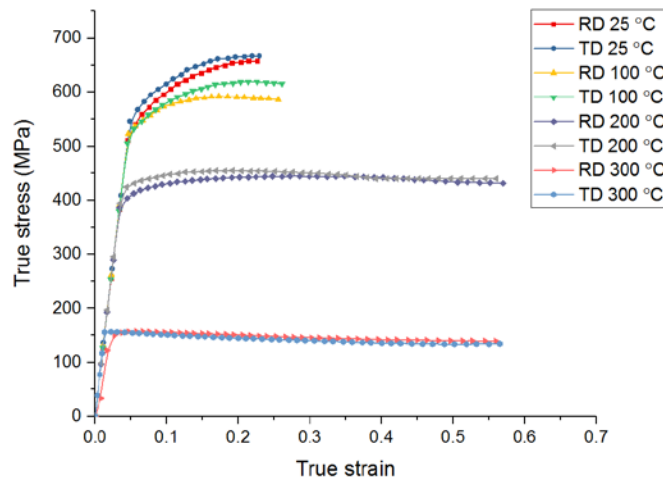


Figure 5.7. Effect of orientation on true stress versus true strain curves (Temper: T6, test speed: 0.005 inch/s (0.127 mm/s), geometry: cylinder).

5.1.4. Effect of temper

The above rolling direction true stress - true strain curves for T6 and O temper specimens at the test speeds of 0.005 inch/s (0.127 mm/s) are replotted in Figure 5.8 to highlight the differences in the flow curves in the two temper states. Clearly, yield strength and flow stress curves are significantly higher for the artificially aged T6 temper compared to the annealed (O-temper) material. The T6 temper has a large fraction of precipitates which offer significant resistance to dislocation motion as well formation of dislocation debris during deformation resulting in much higher yield strength and flow stress up to a test temperature of 200 °C compared to the O-temper alloy. The O-temper material, on the other hand, has very low dislocation density in the initial state and a higher mean free path for moving dislocation which provides a lower yield strength as well as a more sustained work hardening rate up to large plastic strains, compared to the T6 alloy, as cross-slip and dislocation multiplication occurs. The onset of plastic strain localization and ductile damage is postponed in the O-temper state resulting in large plastic strains prior to fracture compared to the T6 alloy. At 300 °C there is significant dynamic recovery and recrystallization in the T6 temper, which results in lowering of the flow stress and the true stress-strain curve becomes much closer to that of the O-temper material.

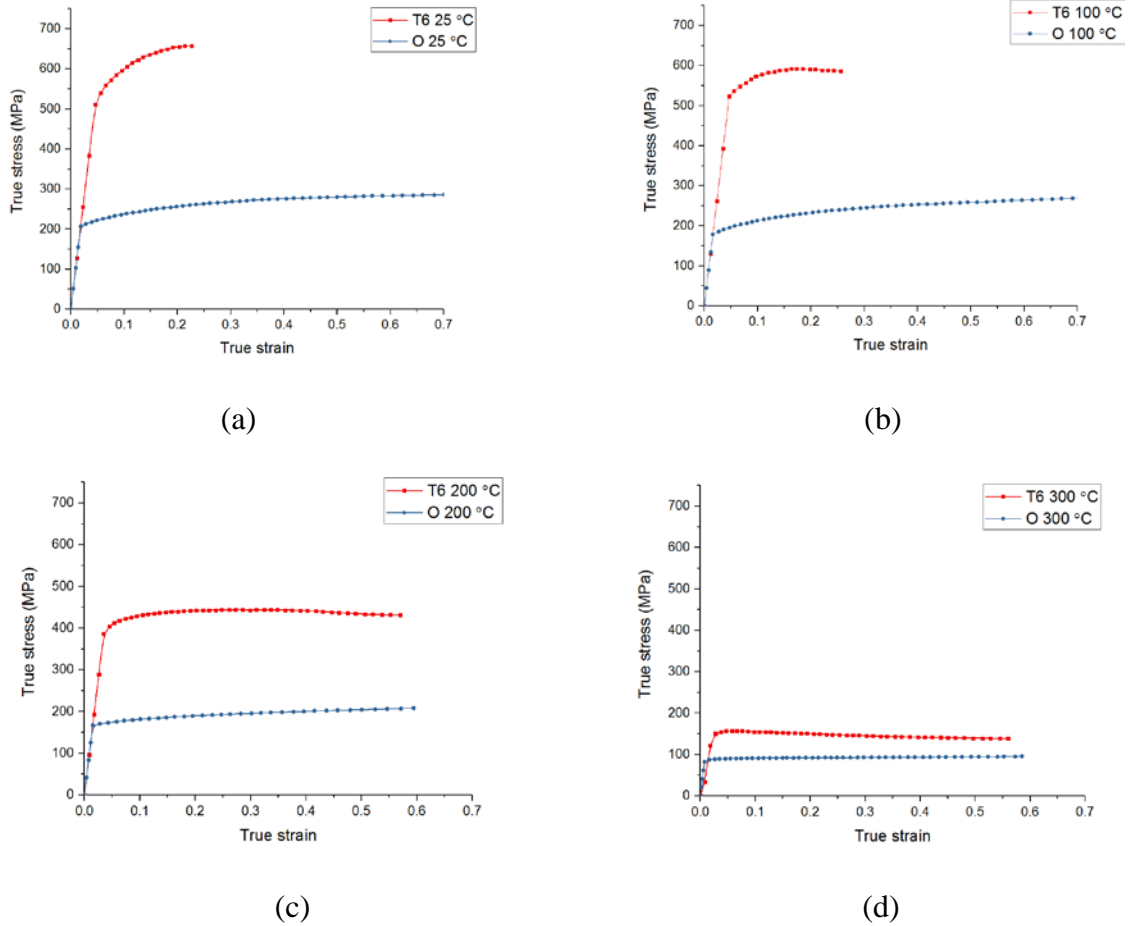
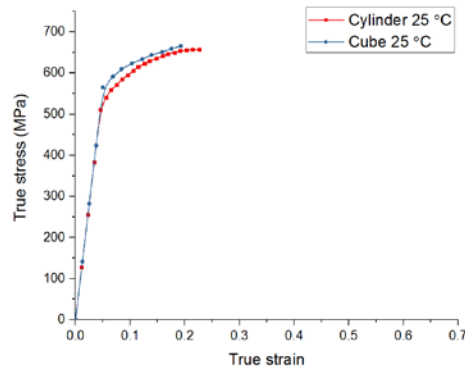


Figure 5.8. Effect of temper on true stress versus true strain curves. (a) 25 °C, (b) 100 °C, (c) 200 °C and (d) 300 °C (Orientation: RD, test speed: 0.005 inch/s (0.127 mm/s), geometry: cylinder).

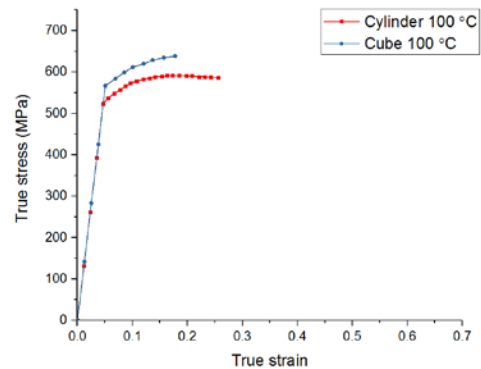
5.1.5. Effect of test specimen geometry

As noted earlier, two different specimen geometries were utilized in the uniaxial compression experiments to analyze the nature of the deformation processes as a function of specimen shape. The cubic specimen exhibited marginally higher flow stress and lower strains to fracture compared to the cylindrical specimens at lower temperatures (RT and

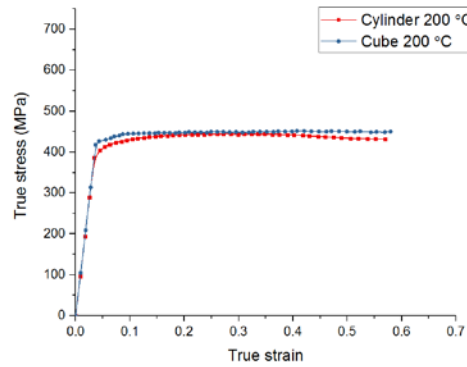
100 °C) but revealed very similar behavior at higher temperatures of 200 °C and 300 °C (see Figures 5.9 and 5.10). The differences in flow stress curves at lower temperatures could arise from more non-uniformity of flow in cubic specimens due to the presence of corners in the specimen geometry which are likely responsible for more constrained plastic flow and early onset of localization. At higher temperatures, with increased strain rate sensitivity of the material, such corner effect is less likely to have an effect on the flow stress and strain localization in the specimen. The role of specimen geometry is discussed further in the context of FE simulation results from the two different specimen geometries. The trends in true stress-strain curves with respect to the two test directions, RD and TD, are very similar at all test temperatures.



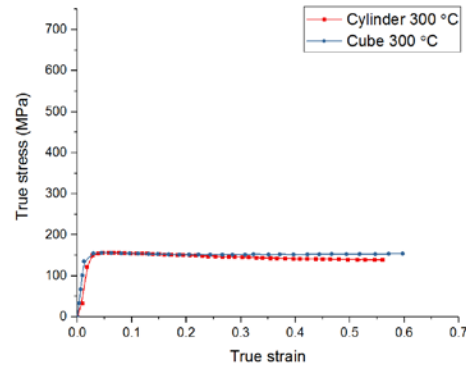
(a) 25 °C



(b) 100 °C

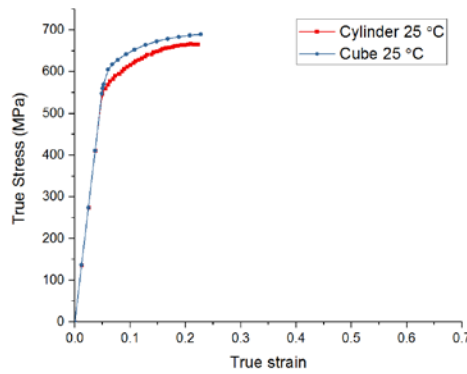


(c) 200 °C

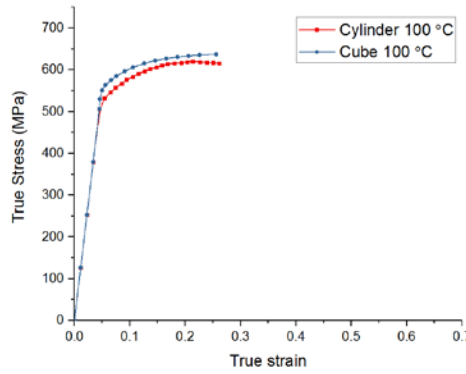


(d) 300 °C

Figure 5.9. Effect of geometry on true stress versus true strain curves. (a) 25 °C, (b) 100 °C, (c) 200 °C and (d) 300 °C (Temper: T6, orientation: RD, test speed: 0.005 inch/s (0.127 mm/s)).



(a) 25 °C



(b) 100 °C

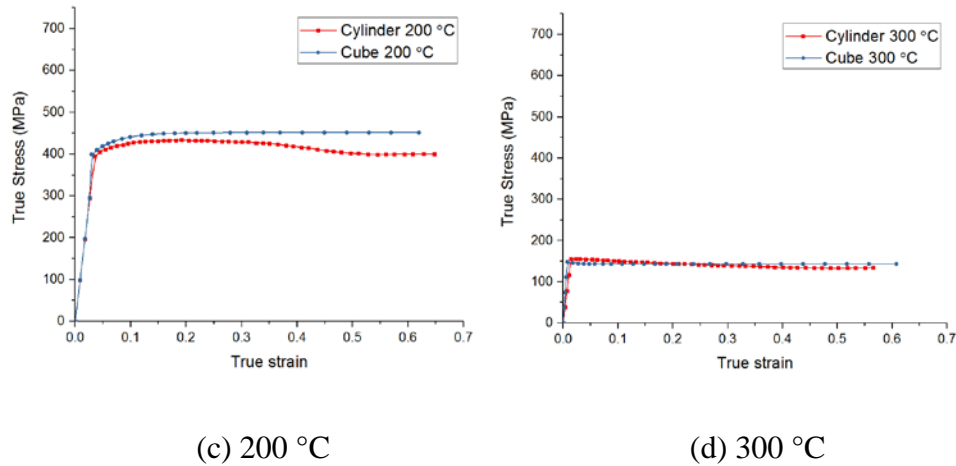
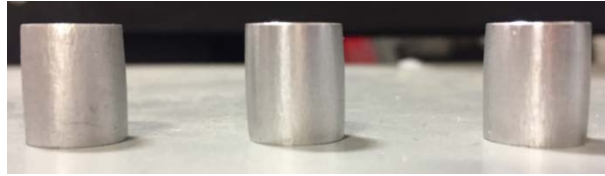


Figure 5.10. Effect of specimen geometry on true stress versus true strain curves. (a) 25 °C, (b) 100 °C, (c) 200 °C and (d) 300 °C (Temper: T6, orientation: TD, test speed: 0.005 inch/s (0.127 mm/s)).

5.1.6. Pattern of flowlines and barrelling characteristics of test specimens

Figures 5.11-5.13 each present sets of photographs of deformed cylindrical specimens from the above test conditions corresponding to different test orientations, tempers, temperatures and test speeds. Figures 5.11(a, b) and 5.12(a, b) represent specimen images for the T6 temper specimens tested RT and 100 °C at the three test speeds. Since compression distances are short (and the deformation small), the deformed surfaces remain smooth. Note that the compression distance at 100 °C is larger than the distance at RT. Also, the test speeds did not influence the surface characteristics of the specimens in the lower temperature. The specimens tested at 200 °C and 300 °C, in sets of Figures 5.11 (c, d) and 5.12 (c, d), are more ductile and subjected to larger strains. The specimen images thus reveal increased barrelling and presence of flowlines on the surface. The flow lines are

typically vertical in the region of contact with the top and bottom compression platens but highly inclined in the middle of the specimen. The regularity of the flowlines at higher speeds is somewhat disturbed at higher speeds. The pattern of flow lines is likely the result of friction and material constraint in the platen regions and less so in the middle of the specimen as well as increased barrelling in the middle of the specimen. In addition to the above deformation features, some specimens exhibited marked planar shear-like distortion of the entire specimen (see for example, rightmost images in Figures 5.11(b, c) and 5.12 (b, c)). This effect appeared more pronounced in the case of higher strain rate tests, but not always. Such a specimen shape distortion likely arose from dissimilar friction at the top and bottom platen/specimen interfaces during the test. Although MoS₂ lubricant film was applied on both platens, it is likely that the surface smoothness of the two platen was not identical and played a role in governing friction. No marked difference in the flow pattern and barrelling characteristics was observed as a function of the test orientation (RD versus TD). Similar optical images from O-temper cylindrical specimens tested in the RD direction are presented in Figure 5.13. The images in terms of flowlines and specimen shape distortion appear in the O-temper specimens appear similar to the T6 specimens. Overall, a larger degree of barrelling can be observed in the O temper material, especially at lower temperatures, and this is consistent with the larger strains to which O temper material could be subjected prior to fracture compared to the T6 specimens (see earlier Figures 5.1 and 5.3)



(a) RT at 0.00066 inch/s (0.0167 mm/s), 0.005 inch/s (0.127 mm/s) and 0.025 inch/s (0.635 mm/s).



(b) 100 °C at 0.00066 inch/s (0.0167 mm/s), 0.005 inch/s (0.127 mm/s) and 0.025 inch/s (0.635 mm/s).

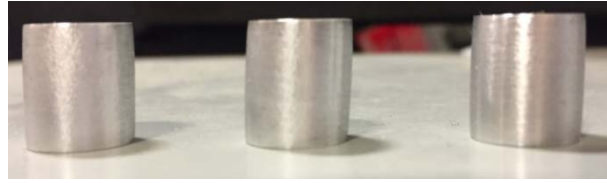


(c) 200 °C at 0.00066 inch/s (0.0167 mm/s), 0.005 inch/s (0.127 mm/s) and 0.025 inch/s (0.635 mm/s).



(d) 300 °C at 0.00066 inch/s (0.0167 mm/s), 0.005 inch/s (0.127 mm/s) and 0.025 inch/s (0.635 mm/s).

Figure 5.11. Deformed cylindrical specimens after isothermal compression tests at 4 different temperature, (a)RT, (b) 100 °C (c) 200 °C and (d) 300 °C (Temper: T6, orientation: RD).



(a) RT at 0.00066 inch/s (0.0167 mm/s), 0.005 inch/s (0.127 mm/s) and 0.025 inch/s (0.635 mm/s).



(b) 100 °C at 0.00066 inch/s (0.0167 mm/s), 0.005 inch/s (0.127 mm/s) and 0.025 inch/s (0.635 mm/s).



(c) 200 °C at 0.00066 inch/s (0.0167 mm/s), 0.005 inch/s (0.127 mm/s) and 0.025 inch/s (0.635 mm/s).



(d) 300 °C at 0.00066 inch/s (0.0167 mm/s), 0.005 inch/s (0.127 mm/s) and 0.025 inch/s (0.635 mm/s).

Figure 5.12. Deformed cylindrical specimens after isothermal compression tests for 4 different temperature, (a) RT, (b) 100 °C (c) 200 °C and (d) 300 °C (Temper: T6, orientation: TD).



(a) RT at 0.00066 inch/s (0.0167 mm/s), 0.005 inch/s (0.127 mm/s) and 0.025 inch/s (0.635 mm/s).



(b) 100 °C at 0.00066 inch/s (0.0167 mm/s), 0.005 inch/s (0.127 mm/s) and 0.025 inch/s (0.635 mm/s).



(c) 200 °C at 0.00066 inch/s (0.0167 mm/s), 0.005 inch/s (0.127 mm/s) and 0.025 inch/s (0.635 mm/s).



(d) 300 °C at 0.00066 inch/s (0.0167 mm/s), 0.005 inch/s (0.127 mm/s) and 0.025 inch/s (0.635 mm/s).

Figure 5.13. Deformed cylindrical specimens after isothermal compression tests for 4 different temperature, (a) RT, (b) 100 °C (c) 200 °C and (d) 300 °C (Temper: O Temper, orientation: RD).

Images of deformed cubic T6 specimens tested under different orientations, temperatures and test speeds are shown in Figures 5.14 and 5.15. For comparison, the sets of images are arranged in a similar pattern to the earlier cylindrical T6 RD and TD specimens. As in the case of cylindrical specimens, the lower temperatures tests, RT and 100 °C, exhibited minimal barrelling due to lower strains, with more pronounced barrelling at 200 °C and 300 °C at larger strains. Also, the barrelled shape and overall shape distortion was more complex for the cubic specimens compared to the cylindrical specimens with material in the corner regions deforming differently from the 4 side faces of the cube. The deformed shape of the cubes perhaps also compounded the likelihood of frictional differences at the top and bottom platen/specimen interfaces. For example, observing the images in Figures 5.14(c,d) and 5.15(c,d), for tests conducted at 200 °C and 300 °C in the RD and TD direction directions respectively at three different test speeds, the curvature developments in all 6 cube faces and 12 edges at the two temperatures appear to be different. More detailed and systematic investigation of deformation of cubic specimens will be needed in the future.



(a) RT at 0.00066 inch/s (0.0167 mm/s), 0.005 inch/s (0.127 mm/s) and 0.025 inch/s (0.635 mm/s).



(b) 100 °C at 0.00066 inch/s (0.0167 mm/s), 0.005 inch/s (0.127 mm/s) and 0.025 inch/s (0.635 mm/s).

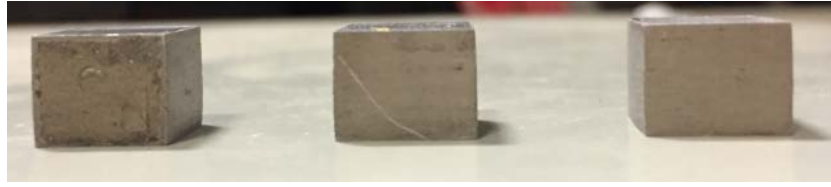


(c) 200 °C at 0.00066 inch/s (0.0167 mm/s), 0.005 inch/s (0.127 mm/s) and 0.025 inch/s (0.635 mm/s).



(d) 300 °C at 0.00066 inch/s (0.0167 mm/s), 0.005 inch/s (0.127 mm/s) and 0.025 inch/s (0.635 mm/s).

Figure 5.14. Deformed cubic specimens after isothermal compression tests for 4 different temperature, (a) RT, (b) 100 °C (c) 200 °C and (d) 300 °C (Temper: T6, orientation: RD).



(a) RT at 0.00066 inch/s (0.0167 mm/s), 0.005 inch/s (0.127 mm/s) and 0.025 inch/s (0.635 mm/s).



(b) 100 °C at 0.00066 inch/s (0.0167 mm/s), 0.005 inch/s (0.127 mm/s) and 0.025 inch/s (0.635 mm/s).



(c) 200 °C at 0.00066 inch/s (0.0167 mm/s), 0.005 inch/s (0.127 mm/s) and 0.025 inch/s (0.635 mm/s).



(d) 300 °C at 0.00066 inch/s (0.0167 mm/s), 0.005 inch/s (0.127 mm/s) and 0.025 inch/s (0.635 mm/s).

Figure 5.15. Deformed cubic specimens after isothermal compression tests for 4 different temperature, (a) RT, (b) 100 °C (c) 200 °C and (d) 300 °C (Temper: T6, orientation: TD).

5.2. Non-isothermal test results

As described in the experimental methodology chapter earlier, uniaxial compression experiments under non-isothermal conditions were carried out by rapidly heating the specimen by passing large currents over a very short time period between the top and bottom surface of the specimens using compression platens which also acted as anodic and cathodic electrodes. The heating of the specimen occurred by a process referred to as electrical resistance heating or ‘joule’ heating. The heated specimens were immediately compressed to large strains at speeds higher than those utilized in the earlier isothermal tests due to experimental limitations. Under such short periods of rapid heating, the temperature uniformity of the specimen was not achieved. This is often a characteristic of real high temperature deformation processes utilized in industry such as in hot forging and upsetting. The scientific interest was to see how the temperature non-uniformity will affect the material flow and fracture characteristics of AA7075-T6 alloy. The specimen preparation and temperature measurement procedure were described earlier in Chapter 3. This sub-section presents the results of non-isothermal tests in a manner similar to that of isothermal results of the previous sub-section.

5.2.1. Temperature versus time curves

The temperature versus time curves from separate electric resistance heating experiments on an un-deformed cylindrical specimen for 3 different applied currents are shown in Figure 5.16. As shown, in the first 5 seconds or so, the temperature increases rapidly and linearly to a peak value depending on the applied current and then decreases non-linearly to a steady

state close to room temperature in about 125 seconds. The peak temperature from application of 5 kA, 7.5 kA and 10 kA currents are about 230 °C, 330 °C and 450 °C respectively, all of the temperature are below the eutectic melting temperature of 480 °C for AA7075 alloy. It is to be noted that eutectic melting leads to the formation of brittle phases which are detrimental to the formability of the alloy. Since the compression test was finished in 3 seconds, and instantly after the peak temperature was reached, it is assumed that the temperature at the symmetric centre of the specimen (i.e., location of the thermocouple) was close to the above temperatures during the non-isothermal compression experiments. The curves in Figure 5.16 indicate that the rate of heating was rather similar for the different applied currents but the rate of cooling of the specimen due to conduction within specimen, and convection and radiation via ambient air after the peak temperature was reached, was slower at higher applied currents (and peak temperatures) compared to the lower applied currents (and peak temperatures).

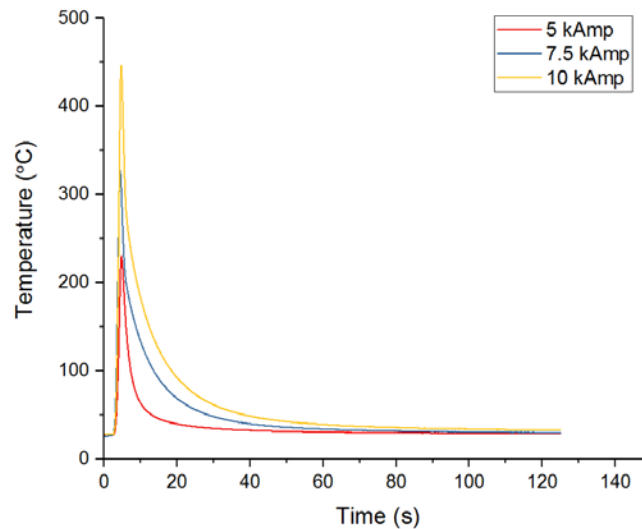
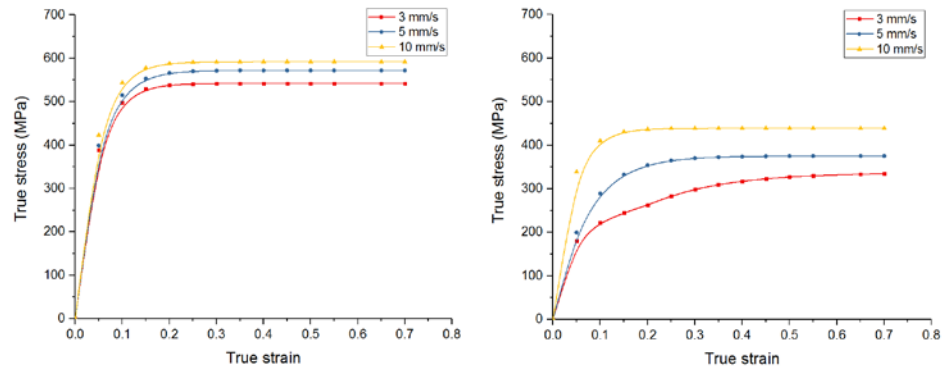


Figure 5.16. Temperature versus time for different applied currents.

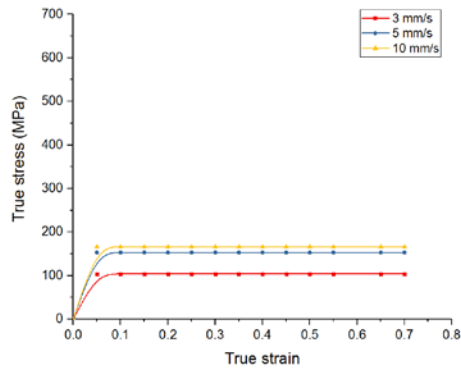
5.2.2. Effect of test speed

The true stress-strain curves from compression tests on AA7075-T6 cylindrical specimens in the transverse orientation conducted at 3 different applied currents and test speeds are presented in Figure 5.17 (a-c). While the results of isothermal and non-isothermal tests cannot be directly compared due to differences in the specimen test conditions (temperature and test speeds), some similarities can still be noted. For example, both sets of stress-strain curves exhibit low work hardening rates and early stress saturation at elevated temperatures and could be deformed to large plastic strains without fracture (compare earlier Figure 5.2 with Figure 5.17 below). As the applied current is increased, the peak temperature of the specimen is increased which leads to a reduction in the flow stress of the material. It is to be noted that the non-isothermal tests were stopped at larger plastic strains, typically of the order of 0.7, whereas isothermal tests specimens were stopped at a strain of about 0.6. Also, for non-isothermal specimens, the test speed effect is more pronounced at intermediate applied currents (and thus intermediate peak temperatures) compared to the lower or higher applied currents. In general, the results suggest that rapid electrical resistance heating could be a viable method for attaining large strains to form complex geometries at higher manufacturing process speeds and more efficiently in transient hot upsetting and forging processes.



(a)

(b)



(c)

Figure 5.17. Effect of test speed on true stress versus true strain curves, (a) 5 kA, (b) 7.5 kA and (c) 10 kA (Temper: T6, orientation: TD, geometry: cylinder).

5.2.3. Effect of applied current

The earlier true stress – strain curves are replotted as Figure 5.18 (a-c) to separately show the effect of test speed at the 3 applied currents. The effect of test speed appears to be most pronounced at the intermediate applied current of 7.5 kA.

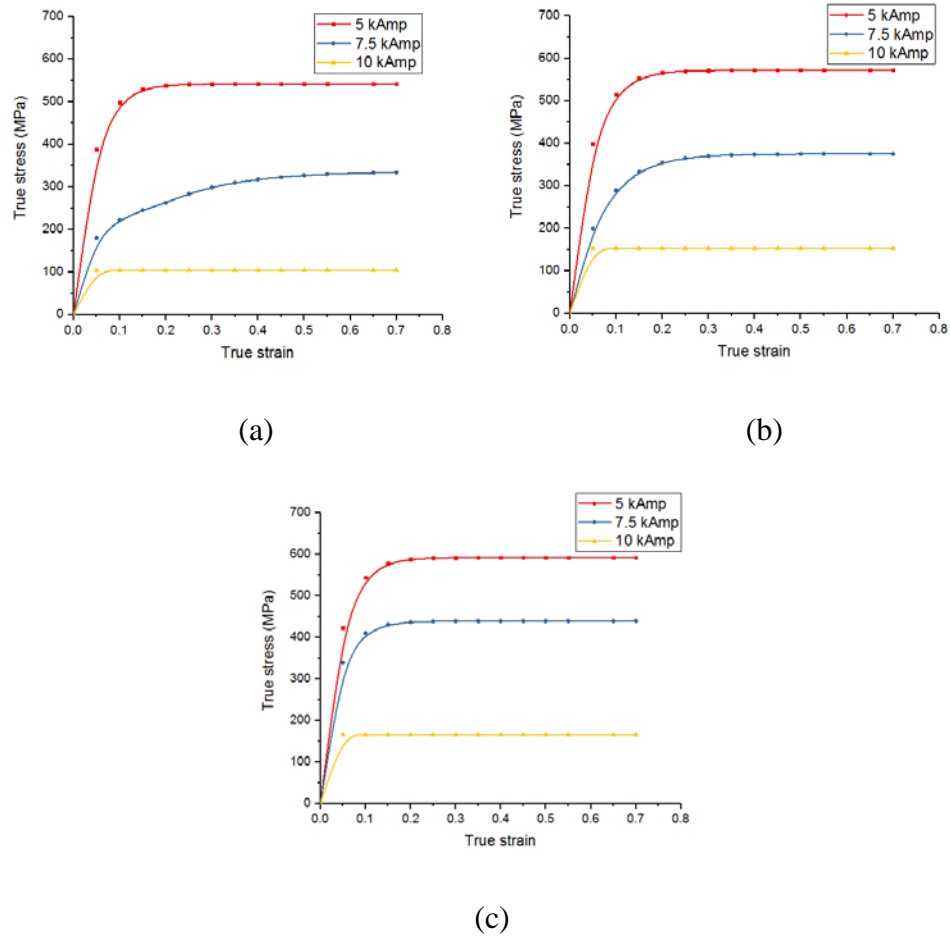


Figure 5.18. Effect of applied current on true stress and true strain curves; (a) 3 mm/s, (b) 5 mm/s and (c) 10 mm/s (Temper: T6, orientation: TD, geometry: cylinder).

5.2.4. Effect of specimen geometry

The effect of specimen geometry in the non-isothermal test conditions is illustrated in Figure 5.19 (a-c) for the three applied currents and test speeds. The cubic specimens were tested in T6 temper condition and in the TD orientation only. As shown, the cubic specimens exhibited higher flow curves compared to the cylindrical specimens under all of the test conditions, and in agreement with the earlier isothermal tests. The magnitude of the difference in saturated flow stress also remained largely the same for all test conditions. As stated earlier, it is believed that material flow is more constrained in the case of cubic specimens compared to the cylindrical specimens due to the presence of corners in the cubic geometry. Also, the differences are likely coming from differences in strain path of the critical region, the region that becomes the site of strain localization and fracture, for the cylindrical and cubic specimens. It is well known that aspect ratio of the cylindrical specimen governs the strain path during the construction of the forming limit strains. A lower height to diameter ratio, for example, results in strain paths closer to plane strain whereas a higher height to diameter ratio shifts the strain path closer to the uniaxial compression state. It is expected that the cubic specimens with a lower aspect ratio of 1, compared to the cylindrical specimens with height to diameter ratio of 1.5, exhibit a strain path closer to the plane strain state compared to the cylindrical specimen. Such differences in strain path can manifest in not only different limit strains but also different flow stresses.

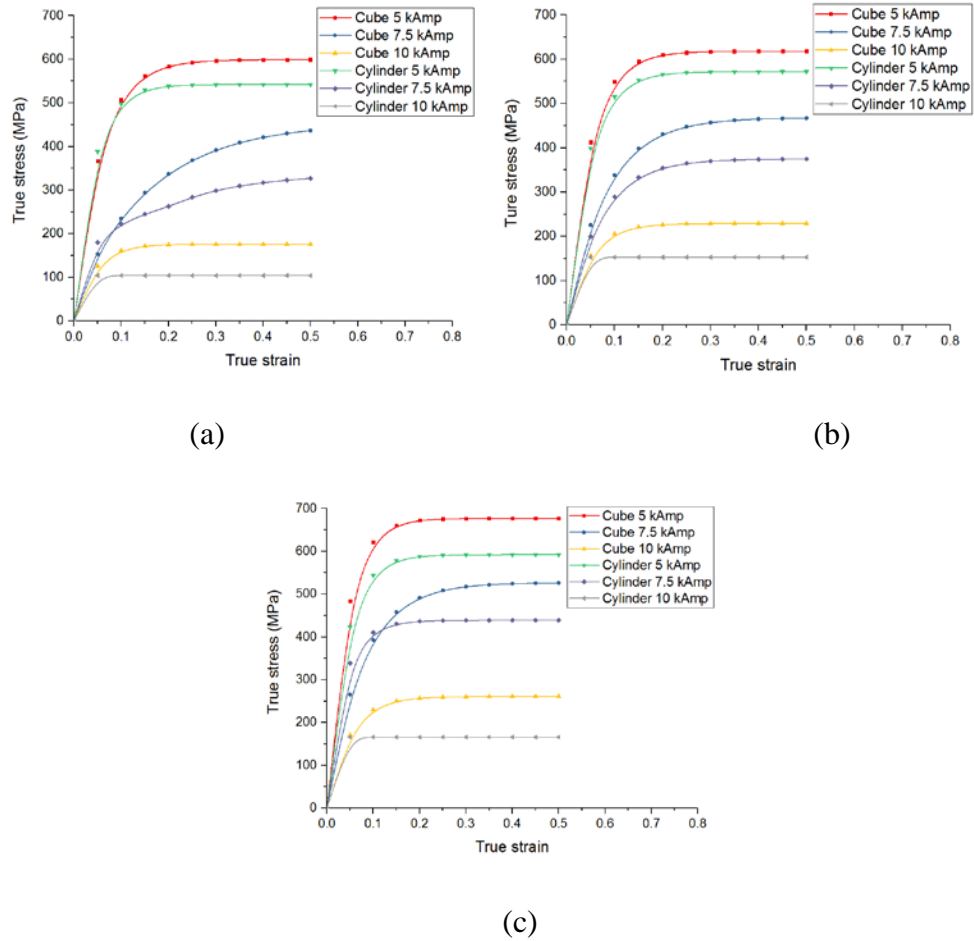


Figure 5.19. Effect of geometry on true stress and true strain curve (a) 3 mm/s, (b) 5 mm/s and (c) 10 mm/s (Temper: T6, orientation: TD).

5.2.5. Pattern of flowlines, barrelling and fracture characteristics of non-isothermal test specimens

Figure 5.20 (a-c) presents a set of photographs of cylindrical test specimens obtained under different applied currents and test speeds. The first two sets of photos, corresponding to applied currents of 5 kA and 7.5 kA, reveal rather smooth deformed surfaces typical of

well-formed components. A pattern of shallow X-shaped flowlines typical of intersecting macroscopic shear bands can be seen on the outer surface of highly barrelled specimens at these applied currents and the three test speeds. The last set corresponding to the applied current of 10 kA and the 3 test speeds exhibits multiple fracture sites located circumferentially at the mid-height of the specimen where circumferential strains and hydrostatic tension from barrelling have the largest value. This is also the location where the local temperature is highest in value at the symmetric centre of the specimen and lowest at the outer periphery of specimen at mid-height location. A large thermal gradient implies that the inner core of the specimen tries to expand while the outer periphery being cold restrains the expansion of the core and thus undergoes a rapid circumferential tension at the mid-height resulting in a catastrophic failure during compression. The failures observed under isothermal uniaxial compression were typically singular and planar with a faceted appearance, and at an angle close to 45° with respect to the loading axis (slant failures). Ductile fracture under uniaxial compression is discussed later in the FE modeling results sub-section.



(a) 5 kA at 3 mm/s, 5 mm/s and 10 mm/s.



(b) 7.5 kA at 3 mm/s, 5 mm/s and 10 mm/s.



(c) 10 kA at 3 mm/s, 5 mm/s and 10 mm/s.

Figure 5.20. Deformed cylindrical specimens after non-isothermal compression tests for 3 different applied currents, (a) 5 kA, (b) 7.5 kA and (c) 10 kA.

Similar results for cubic specimens at three applied currents and test speeds are shown in Figure 5.21. The deformed shapes are complex but generally similar to the earlier isothermal deformed cubes. Unlike the cylindrical specimens, no fracture of the specimen was observed in cubic specimens at the applied current of 10 kA. Some sparking, however, in these specimens at higher currents possibly due to the curvature development in the top and bottom faces of the cubic specimen in contact with the compression platens.



(a) 5 kA at 3 mm/s, 5 mm/s and 10 mm/s.



(b) 7.5 kA at 3 mm/s, 5 mm/s and 10 mm/s.



(c) 10 kA at 3 mm/s, 5 mm/s and 10 mm/s.

Figure 5.21. Deformed cubic specimens after non-isothermal compression tests for 3 different applied currents, (a) 5 kA, (b) 7.5 kA and (c) 10 kA.

Figures 5.22 and 5.23 show the top and side views of the deformed cylindrical and cubic specimens respectively for the entire range of test conditions. In general, the cylindrical specimens are smoother and the curvature development on the outer surface is more uniform. The cubic specimen exhibit less uniform curvature where the mid-section tends to deform considerably more compared to the two ends of the specimen. There is a lack of symmetry of the top and bottom surfaces of deformed cylindrical and cubic specimens. As mentioned earlier, this is likely caused by variation in friction conditions at the two surfaces. Also, it is noted that the material in the corner region, in the case of cubic specimens, deforms in a different manner compared to the flat side surface, and this confirms the constrained nature of deformation of the cubic specimen compared to cylindrical specimens. This is more clearly evident in the top views of the various cubic specimens in Figure 5.23. More on this aspect of deformation is presented in the subsequent FE modeling section.



(a) 5 kA at 3 mm/s, 5 mm/s and 10 mm/s.

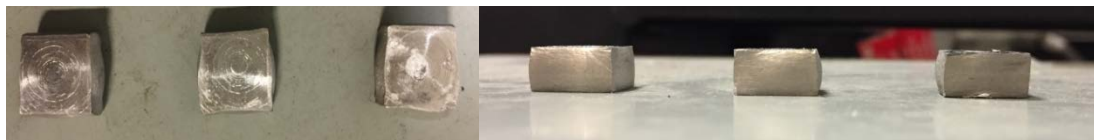


(b) 7.5 kA at 3 mm/s, 5 mm/s and 10 mm/s.



(c) 10 kA at 3 mm/s, 5 mm/s and 10 mm/s.

Figure 5.22. Top and side views of cylinder after compression test (a) 5 kA at 3 mm/s, 5 mm/s and 10 mm/s, (b) 7.5 kA at 3 mm/s, 5 mm/s and 10 mm/s and (c) 10 kA at 3 mm/s, 5 mm/s and 10 mm/s.



(a) 5 kA at 3 mm/s, 5 mm/s and 10 mm/s.



(b) 7.5 kA at 3 mm/s, 5 mm/s and 10 mm/s.



(c) 10 kA at 3 mm/s, 5 mm/s and 10 mm/s.

Figure 5.23. Top view and side view of cube after compression test (a) 5 kA at 3 mm/s, 5 mm/s and 10 mm/s, (b) 7.5 kA at 3 mm/s, 5 mm/s and 10 mm/s and (c) 10 kA at 3 mm/s, 5 mm/s and 10 mm/s.

5.3. Microstructures of deformed isothermal and non-isothermal compression test specimens

This section presents the results of microstructural examination of cut, polished and etched cross-sections of the deformed cylindrical and cubic specimens from uniaxial compression tests under isothermal and non-isothermal test conditions using digital optical microscopy (OM) method. The details of the specimen preparation and optical microscopy method were provided earlier in Chapter 3. The micrographs consist of relatively low magnification images of the test specimens to analyze the general nature of the material flow as a function of test conditions. The images were taken from the vertical plane that divides the entire specimen into two half cylinders along the loading axis, as explained earlier. In the figures presented below, the micrographs have been arranged as a row of 3 micrographs from the same vertical plane for ease of understanding. The leftmost image in the row of images is from the entire vertical plane at a lower magnification, and the other two images to the right are from the central and top left regions of the vertical plane respectively but at a higher

magnification of $200\times$, as illustrated in Figure 5.24. This placement of optical micrographs applies to Figures 5.25 – 5.28.

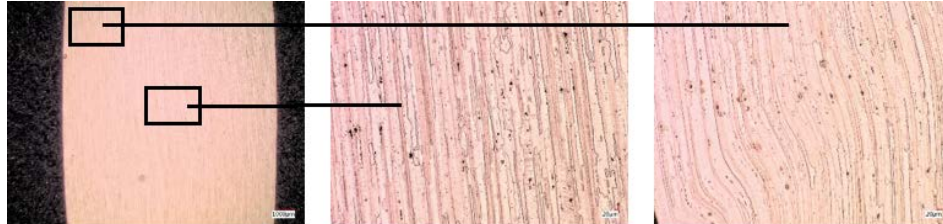
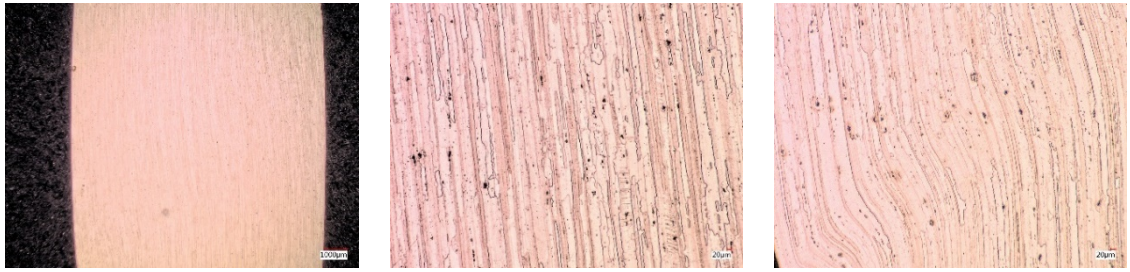


Figure 5.24. A schematic illustration of where in the vertical plane the micrographs have come from in Figure 5.25-5.28.

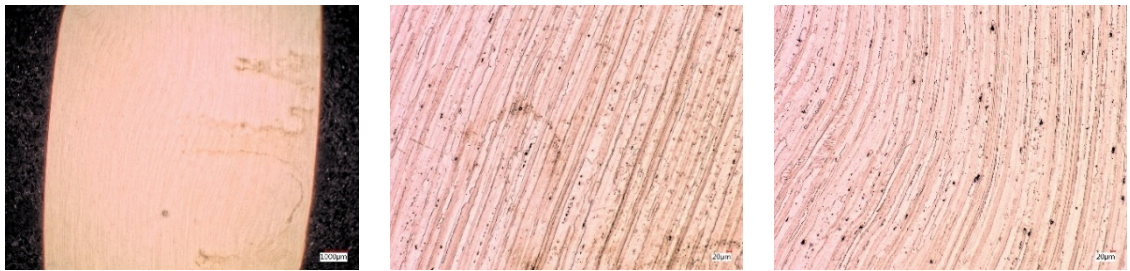
5.3.1. Effect of temperature

Figure 5.25 (a-d) shows 4 sets of 3 micrographs at each of the 4 test temperatures from AA7075-T6 cylindrical specimens tested along RD at 0.005 inch/s (0.127 mm/s) and at room temperature, 100 °C, 200 °C and 300 °C respectively. The room temperature and 100 °C specimens (Figure 5-25 (a, b)) were deformed to a low strain of about 0.3. Therefore, these specimens did not show much evidence of curvature development (or barrelling). At higher temperatures of 200 °C and 300 °C (Figure 5-18 (c, d)), the strains to fracture were much larger and the specimen height was significantly smaller. A region of intense shear can be observed diagonally across the specimen where the flowlines bend considerably due to shear (see Figure 5-25 c(i) and d(i)). The flowlines show minor undulations as well as highly elongated grain structure between the flowlines in the higher magnification images to the right. The darker spots in the image are intermetallic particles that form during the casting process.



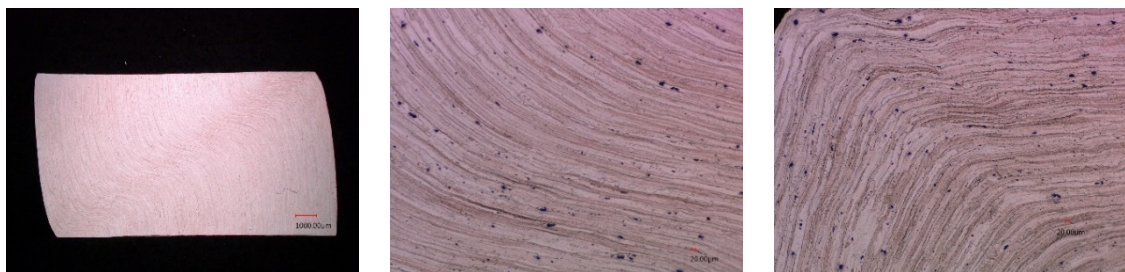
(i) (ii) (iii)

(a). Three views of the vertical plane, (i) entire plane, (ii), central region, and (iii) top left region for a specimen tested at room temperature.



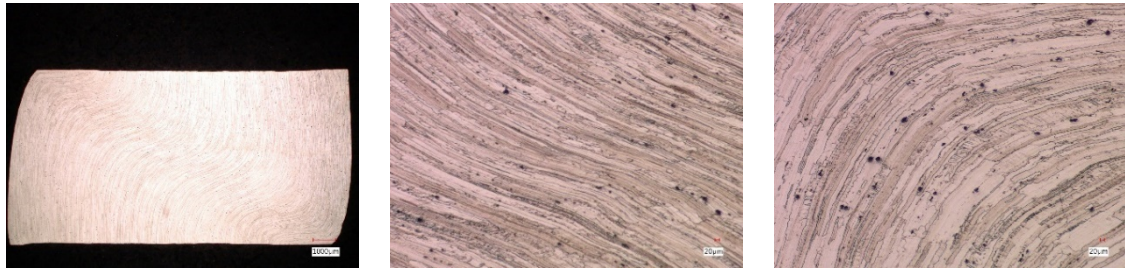
(i) (ii) (iii)

(b). Three views of the vertical plane, (i) entire plane, (ii), central region, and (iii) top left region for a specimen tested at 100 °C.



(i) (ii) (iii)

(c). Three views of the vertical plane, (i) entire plane, (ii), central region, and (iii) top left region for a specimen tested at 200 °C.



(i)

(ii)

(iii)

(d). Three views of the vertical plane, (i) entire plane, (ii), central region, and (iii) top left region for a specimen tested at 300 °C.

Figure 5.25. Optical micrographs of deformed cylindrical specimens tested at different temperatures (Temper: T6, orientation: RD, test speed: 0.005 inch/s (0.127 mm/s).

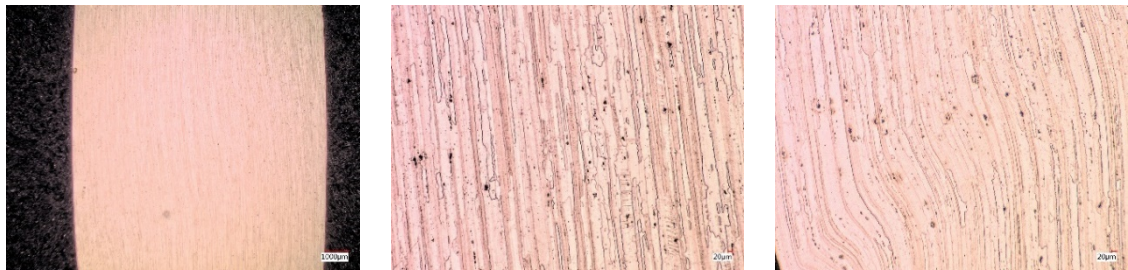
5.3.2. Effect of speed

Figure 5.26 (a-f) presents the effect of test speed at lower (room temperature) and higher (300 °C) temperature conditions. At room temperature, 5.26 (a-c), the microstructures are nearly identical at the 3 different test speeds, the flow of the grain is almost perpendicular to the horizontal line which indicates that the specimen is hard to deform and the test speeds do not affect the compression process. At higher temperature of 300 °C, the grains are highly elongated, and more so than for RT earlier, but the specific effect of test speeds is still not discernible in the images 5.26 (d-f).



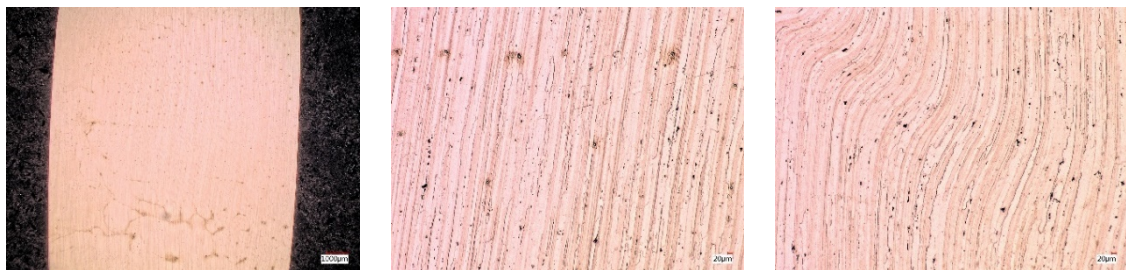
(i) (ii) (iii)

(a) Three views of the vertical plane, (i) entire plane, (ii), central region, and (iii) top left region for a specimen tested at 0.00066 inch/s (0.0167 mm/s) and RT.



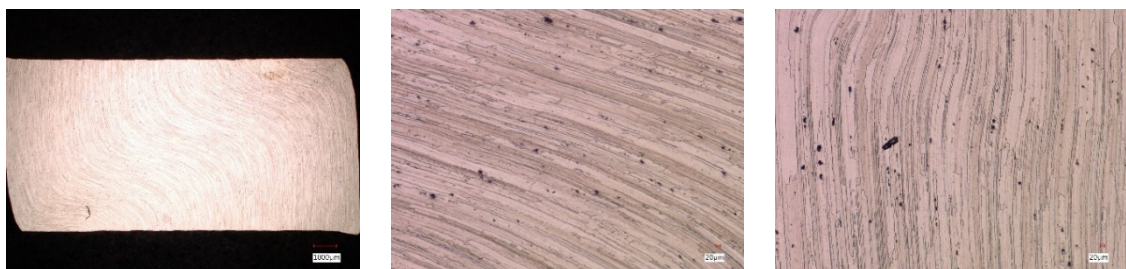
(i) (ii) (iii)

(b) Three views of the vertical plane, (i) entire plane, (ii), central region, and (iii) top left region for a specimen tested at 0.005 inch/s (0.127 mm/s) and RT.



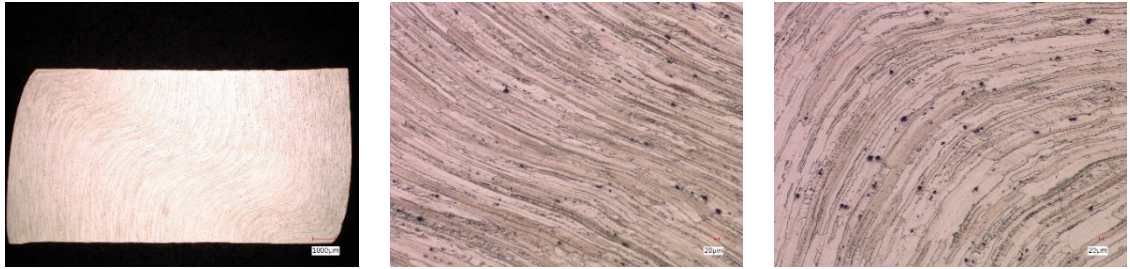
(i) (ii) (iii)

(c) Three views of the vertical plane, (i) entire plane, (ii), central region, and (iii) top left region for a specimen tested at 0.025 inch/s (0.635 mm/s) and RT.



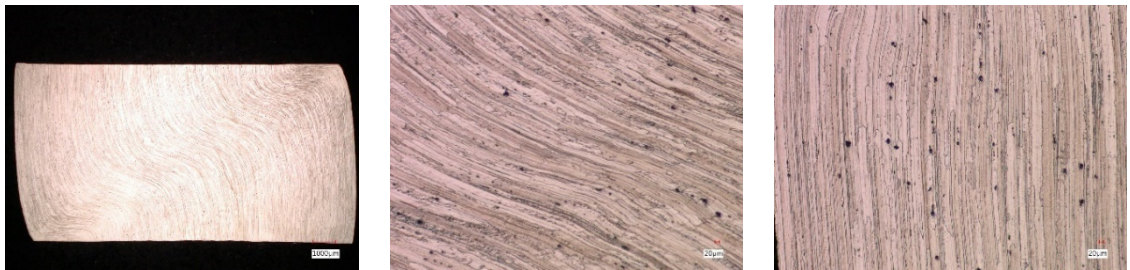
(i) (ii) (iii)

(d). Three views of the vertical plane, (i) entire plane, (ii), central region, and (iii) top left region for a specimen tested at 0.00066 inch/s (0.0167 mm/s) and 300 °C.



(i) (ii) (iii)

(e). Three views of the vertical plane, (i) entire plane, (ii), central region, and (iii) top left region for a specimen tested at 0.005 inch/s (0.127 mm/s) and 300 °C.



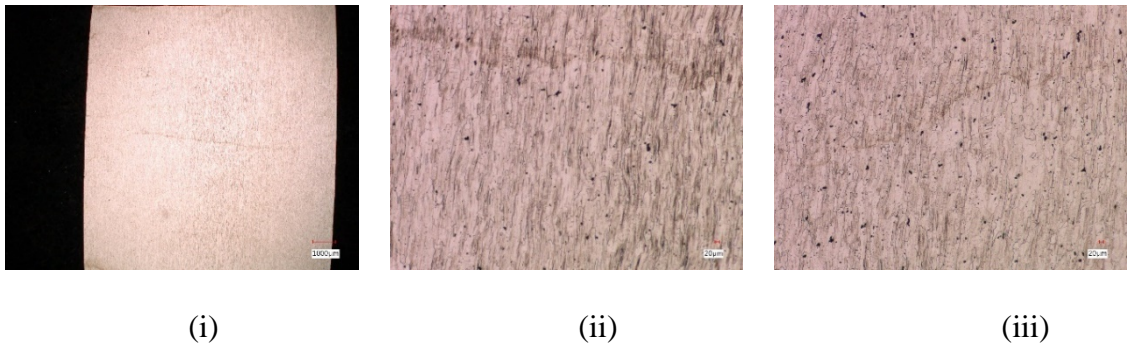
(i) (ii) (iii)

(f). Three views of the vertical plane, (i) entire plane, (ii), central region, and (iii) top left region for a specimen tested at 0.025 inch/s (0.635 mm/s) and 300 °C.

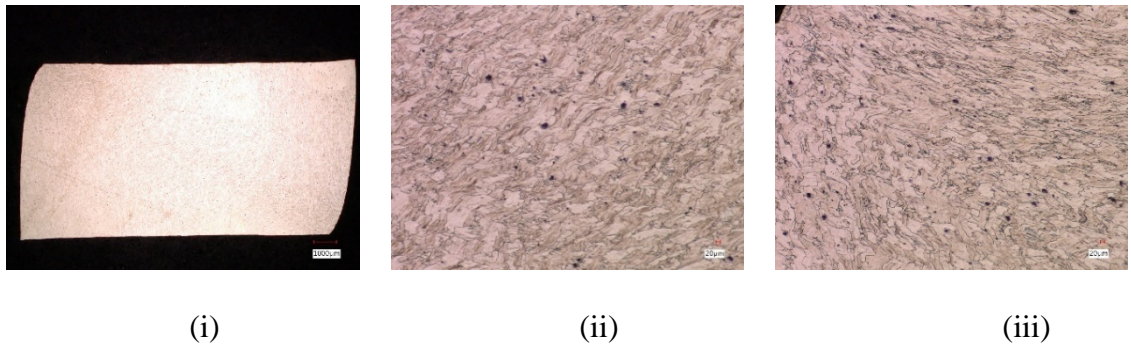
Figure 5.26. Optical micrographs from cylindrical specimens tested at 3 different speeds (Temper: T6, orientation: RD, temperature: RT and 300 °C)

5.3.3. Effect of specimen orientation

Figure 5.27 (a-b) shows the microstructures of deformed cylindrical specimens in TD orientation at room temperature (RT) and 300 °C. Unlike the RD micrographs presented earlier in Figures 5.25 and 5.26 where the grains had become highly elongated, the TD deformed grain structure was less elongated and irregular at both room temperature (low deformation state) as well as at 300 °C (highly deformed state). Also, the characteristic diagonal shear band region was highly irregular in the TD specimens at the elevated temperature. While the initial un-deformed grain structure along RD was highly elongated compared to TD directions (and similar to the long transverse and short transverse plane grain structures of the rolled AA7076-T6 plate from which the cylindrical specimens were prepared), the deformed grain characteristics are indeed quite different for the two orientations. This is likely from the different texture components that are present in the two orientations and how they evolve with the deformation process.



(a) Three views of the vertical plane, (i) entire plane, (ii), central region, and (iii) top left region for TD specimens tested at RT.

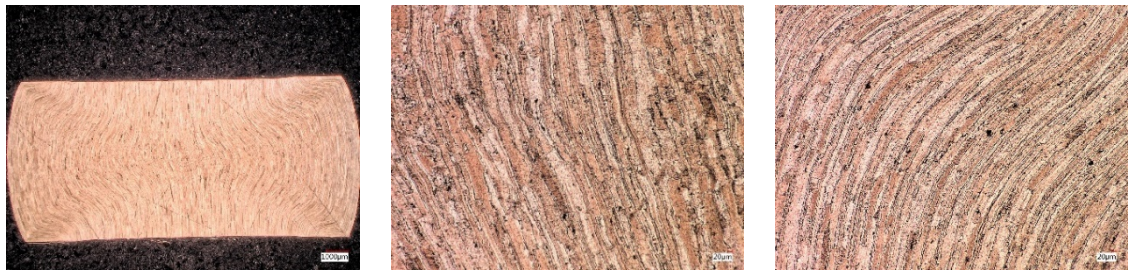


(b). Three views of the vertical plane, (i) entire plane, (ii), central region, and (iii) top left region for TD specimens tested at 300 °C.

Figure 5.27. Optical micrographs from TD cylindrical specimens tested at RT and 300 °C (Temper: T6, orientation: TD, test speed: 0.005 inch/s (0.127 mm/s)).

5.3.4. Effect of temper

Figure 5.28 (a-b) shows deformed microstructures of RD cylindrical specimens tested in the O temper state at RT and 300 °C, for a comparison with the earlier microstructures from T6 temper specimens under the identical test conditions. While the grains in the T6 temper state were highly elongated and flowlines were straight with minimal deformation at RT, the grains of O temper material exhibited significant deformation (see Figure 5.28a) at both room temperature and at 300 °C. The vertical plane of the deformed specimen exhibited the classical intersecting double shear band morphology at room temperature (see Figure 5.28 a(i)) where the conical regions at the top and bottom surfaces remained largely undeformed and the deformation was concentrated in the outer peripheral barrelled region. Similar material flow behavior but with increased barrelling was observed in the O-temper cylindrical specimen at 300 °C (see Figure 5.28 b(i)).

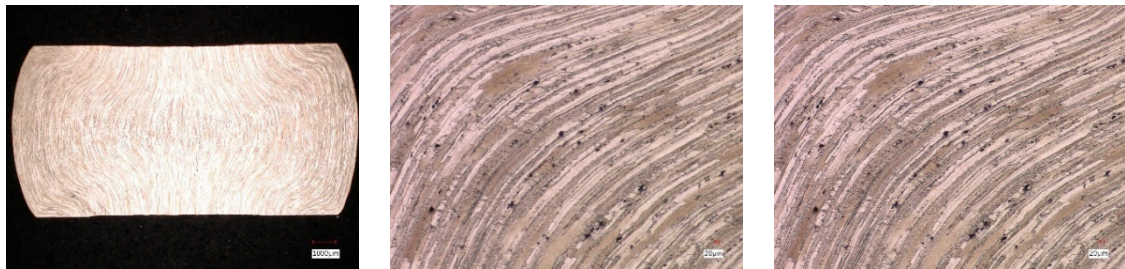


(i)

(ii)

(iii)

(a). Three views of the vertical plane, (i) entire plane, (ii), central region, and (iii) top left region for O temper specimens tested at RT.



(i)

(ii)

(iii)

(b). Three views of the vertical plane, (i) entire plane, (ii), central region, and (iii) top left region for O temper specimens tested at 300 °C.

Figure 5.28. The microstructures of O temper cylindrical specimens (Temper: O, orientation: RD, test speed: 0.005 inch/s (0.127 mm/s).

A set of interrupted tests were also conducted using T6 RD cylindrical specimens corresponding to 3 discrete values of vertical displacements of 1.09 mm, 2.18 mm and 4.36 mm. The specimens were cut, mounted, etched and observed with digital optical microscope, similar to the preceding specimens. Figures 5.29 and 5.30 show increased barrelling and grain elongation of the specimen with increasing compression distance as

well as shear band formation at the largest compression distance at RT and 300 °C respectively. The barrelling is more conspicuous at 300 °C.



(a)

(b)

(c)

Figure 5.29. Three views of the vertical plane at three different compression distances; (a) 1.09 mm, (b), 2.18 mm and (c) 4.36 mm for a specimen tested at 0.005 inch/s (0.127 mm/s) and RT.



(a)

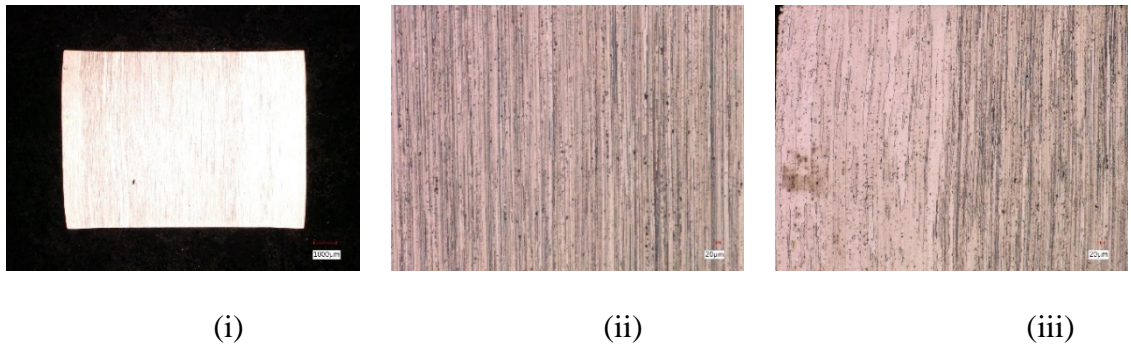
(b)

(c)

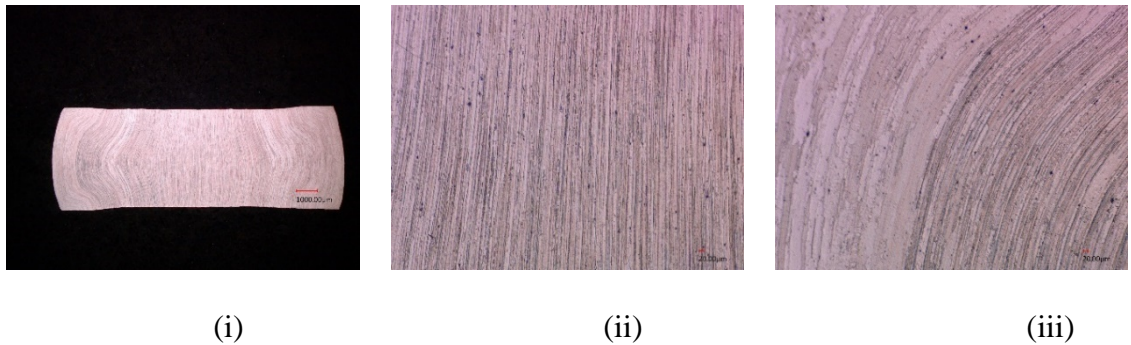
Figure 5.30. Three views of the vertical plane at three different compression distances; (a) 1.88 mm, (b), 3.76 mm and (c) 7.52 mm for a specimen tested at 0.005 inch/s (0.127 mm/s) and 300 °C.

5.3.5. Effect of test specimen geometry

Figure 5.31 (a-b) shows the deformed grain structures of RD cubic specimens in T6 temper and tested at RT and 300 °C. At room temperature, due to rather small deformation and very small barrelling, the elongated grain structure remained largely straight and unchanged (see Figure 5.31a). At 300 °C, with increased deformation and barrelling, the flowlines were curved specifically in the region between the centre and outer surface of the specimen, and followed an overall pattern of the barrelled specimen. It is clear that the deformation of the cubic specimen is more confined (or constrained) compared to that of the cylindrical specimen.



(a). Three views of the vertical plane, (i) entire vertical plane, (ii), central region, and (iii) top left region for cubic specimens tested at RT.



(a). Three views of the vertical plane, (i) entire plane, (ii), central region, and (iii) top left region for cubic specimens tested at 300 °C.

Figure 5.31. Microstructures of deformed cubic specimens tested at room temperature and 300 °C (Temper: T6, orientation: RD, test speed: 0.005 inch (0.127 mm/s)).

5.4. Results from FE simulations of uniaxial compression experiments

This sub-section presents the results of ABAQUS FE simulations of experimental uniaxial compression tests under isothermal test conditions. The results involve assessment of the various strain rate and temperature dependent constitutive material hardening laws as described in Chapter 4. The material parameters for many of the hardening laws were obtained from fit to the entire experimental true stress-true strain data set for the range of test conditions by non-linear least square curve fitting. In this section, the values of fit parameters are presented in Tables and the predicted curves from the fit parameters for various test conditions are compared with the experimental data for Johnson-Cook, Arrhenius model and Voce-Kocks models. The most promising model based on the

prediction, the Voce-Kocks model, was further studied via FE modeling and results related to the nature of plastic flow and strain development based on this model are also presented in this section. Results from uniaxial compressive deformation of both cylindrical and cubic specimens are presented and compared with experimental data where possible. In addition, a well-known, ductile damage development model of Gurson-Tvergaard-Needleman (GTN) model along with an element deletion algorithm is utilized within the FE simulation of cylindrical specimen, and results related to the nature of surface fractures are also presented in this sub-section. Lastly, preliminary results from Tresca fracture model showing development of shear-like fracture from FE simulations of a cylindrical specimen tested at room temperature are presented.

5.4.1. Assessment of constitutive material hardening laws for uniaxial compression of AA7075-T6 alloy

5.4.1.1. Johnson-Cook model

The Johnson-Cook (J-C) strain rate and temperature dependent hardening law was presented earlier in Chapter 4. The mathematical expressions representing the J-C hardening law are reproduced below for ease of reference.

$$\sigma = \left[A + B\varepsilon_p^n \right] \left[1 + C \ln \left(\frac{\dot{\varepsilon}}{\dot{\varepsilon}_0} \right) \right] \left[1 - T^{*m} \right] \quad (5.1)$$

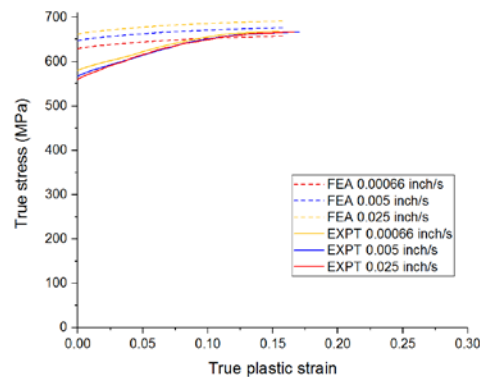
$$T^* = \frac{T - T_{room}}{T_{melt} - T_{room}} \quad (5.2)$$

where A , B , C , n and m are the main material parameters. The material parameters were obtained from non-linear regression based on the set of true stress and true plastic strain curves from the experiment. The R square value of the fitting to equation (5.1) and (5.2) for stress, strain, strain rate and temperature in different cases was 0.967. The material parameters values are shown in Table 5.1 below. These parameters were utilized in the FE model as the input parameters. A comparison of FE simulation based and experimentally obtained true stress-strain curves are shown in Figure 5.32 below. While the general trends in these predictions with respect to effect of temperature and test speed (i.e., strain rate) are in agreement, the shape of the predicted stress-strain curves and their deviation from the experimental flow stress values is not satisfactory. It is clear that J-C material model is unable to capture material softening that occurs at elevated temperatures of 200 °C and

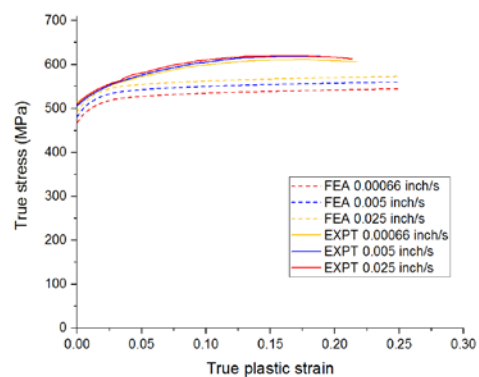
300 °C. This is perhaps because of the single valued strain hardening exponent n and strain rate hardening parameter m in the J-C model. While this model has fewer material parameters and is readily available in the material model library of ABAQUS, it has a limited ability to model a complex material system such as AA7075-T6 alloys. Therefore, no further attempt was made to analyze detailed plastic flow characteristics of the test specimens using the J-C constitutive model.

Table 5.1. Constitutive material parameters for J-C material model.

A (MPa)	B (MPa)	C	n	m	T_{melt} (°C)	T_{room} (°C)	$\dot{\epsilon}_0$
623	126	0.013	0.14	1.04	418	25	1



(a) RT



(b) 100 °C

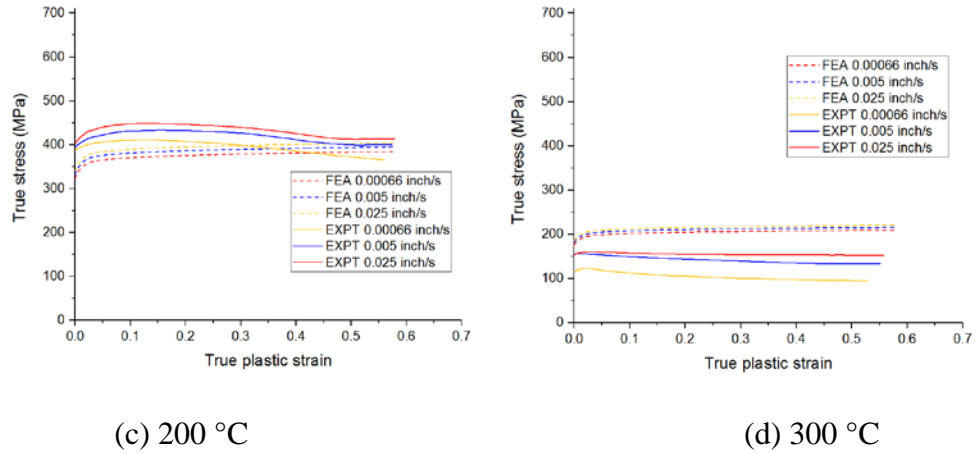


Figure 5.32. Comparisons of predicted true stress-strain curves from FE simulation of uniaxial compression tests using Johnson-Cook model and experimentally obtained curves, (a) room temperature, (b) 100 °C, (c) 200 °C and (d) 300 °C (Temper: T6, orientation: RD, specimen geometry: cylinder).

5.4.1.2. Arrhenius model

Since the Johnson-Cook model within the FE simulations failed to accurately capture the stress-strain characteristics of the test specimens under a range of test conditions, another model, called Arrhenius model from Naser and Krallics (2014) was assessed for its applicability to AA7075-T6 alloy. The Arrhenius model equations were presented earlier in Chapter 4. This equation is reproduced below for convenience.

$$\sigma = \frac{\text{arcsinh}\left(\exp\left(\frac{RT(\ln(\dot{\epsilon}) - \ln(A)) + Q}{RTn}\right)\right)}{\alpha} \quad (5.3)$$

As earlier, the model parameters were obtained via non-linear least square curve fitting. However, two cases were considered, where (i) stress-strain data from all temperatures (RT,

100 °C, 200 °C and 300 °C) and test speeds were included in the fitting, and (ii) only the higher temperatures (200 °C and 300 °C) and all test speeds were included. This choice of data set selection for curve fitting was based on the consideration that perhaps different physical mechanisms operate at low and higher deformation temperatures. The R square values from fitting the Arrhenius equation (5.3) to the first and second cases were 0.800 and 0.997 respectively. Since the parameters $\ln(A)$, Q , n and α are related to strain, a fourth-order polynomial function was applied to describe the relationship between each of the parameters and the strain. These strain dependencies, obtained from the fitting process, for the two cases, are expressed as follows:

Case 1:

$$\ln(A)=10.499+16.955\varepsilon-145.255\varepsilon^2+391.750\varepsilon^3-344.875\varepsilon^4$$

$$Q= 169.294-86.379\varepsilon-207.857\varepsilon^2+935.417\varepsilon^3-962.778\varepsilon^4$$

$$n= 0.219-2.764\varepsilon+38.407\varepsilon^2-161.844\varepsilon^3+217.804\varepsilon^4$$

$$\alpha= 0.38+6.33\varepsilon-70.438\varepsilon^2+265.821\varepsilon^3-327.977\varepsilon^4$$

Case 2:

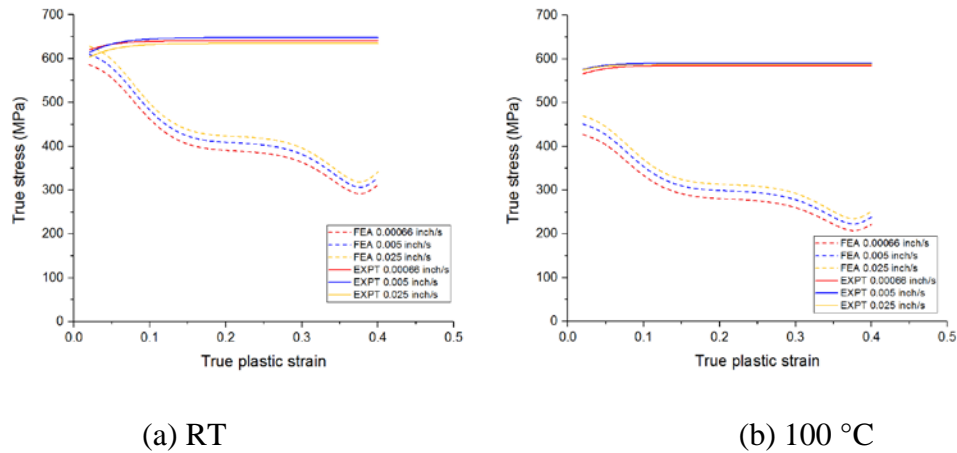
$$\ln(A)=36.053+3.877\varepsilon-118.370\varepsilon^2+236.610\varepsilon^3-140.436\varepsilon^4$$

$$Q= 216.549-50.464\varepsilon-598.298\varepsilon^2+1664.899\varepsilon^3-1510.981\varepsilon^4$$

$$n= 2.539+4.016\varepsilon+12.746\varepsilon^2-97.328\varepsilon^3+146.351\varepsilon^4$$

$$\alpha= 0.0149-0.05\varepsilon+0.11836\varepsilon^2-0.07446\varepsilon^3-0.09618\varepsilon^4$$

The Arrhenius model was implemented as a UMAT subroutine within ABAQUS, and by using the above expressions within the Arrhenius model, predicted stress-strain curves from simulations were obtained. These results are shown in Figures 5.33 and 5.34 for the two cases. Once again, the predicted stress-strain curves were not satisfactory in spite of a more physically-based Arrhenius equation and a large number of model parameters to account for the effect of strain in the analysis (see Figure 5.33). The parameters $\ln(A)$, Q , n and α each involved 5 parameters in the 4th order polynomial fit giving 20 fit parameters. However, when the fitting was restricted to the higher temperature range (case ii), the results were significantly better as shown in Figure 5.34.



(a) RT

(b) 100 °C

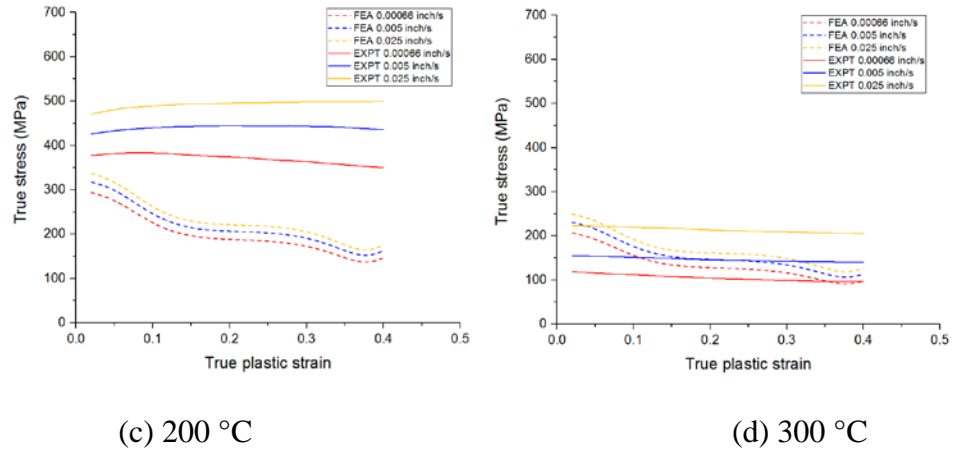


Figure 5.33. Comparison of predicted true stress-strain curves from FE simulation of uniaxial compression tests using Arrhenius model and experimentally obtained curves from case (i) fit parameters; (a) room temperature, (b) 100 °C, (c) 200 °C and (d) 300 °C (Temper: T6, orientation: RD, geometry: cylinder).

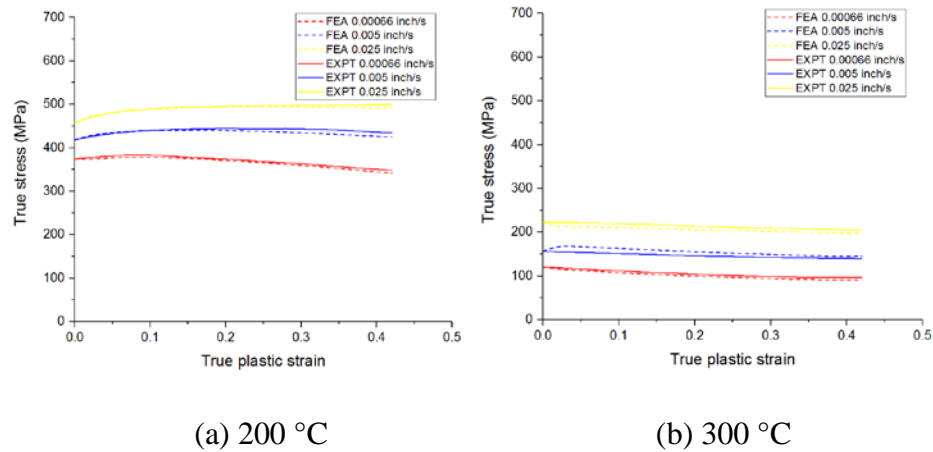


Figure 5.34. Comparison of predicted true stress-strain curves from FE simulation of uniaxial compression tests using Arrhenius model and experimentally obtained curves, case (ii) (a) 200 °C and (b) 300 °C (Temper: T6, orientation: RD, geometry: cylinder).

Based on the limited capabilities of the above two constitutive hardening laws, it was decided to explore another more suitable constitutive model, namely the modified Voce-Kocks model as shown below.

5.4.1.3. Modified V-K model

Chapter 4 presented a discussion about the original V-K model where its limitation was identified. The original V-K model was modified and its new constitutive form was presented in Chapter 4. These equations are reproduced here for convenience.

$$\sigma = \sigma_s + (\sigma_0 - \sigma_s) \exp\left(-\frac{\varepsilon}{\varepsilon_r}\right) \quad (5.3)$$

$$\sigma_s = \sigma_{s0} \left(\frac{\dot{\varepsilon}}{\varepsilon_{s0}}\right)^{\frac{kT}{C_1 \exp(C_2 T)}} \quad (5.4)$$

$$\sigma_0 = \sigma_{k0} \left(\frac{\dot{\varepsilon}}{\varepsilon_{k0}}\right)^{\frac{kT}{C_1 \exp(C_2 T)}} \quad (5.5)$$

$$\varepsilon_r = \frac{\sigma_s}{\theta} \quad (5.6)$$

As earlier, the material parameters for the modified V-K model were obtained by non-linear least square curve fitting to the entire experimental set of true stress-true strain curves. The parameter values are shown in Table 5.2.

Table 5.2. The material parameters for the modified V-K model.

σ_{s0}	ε_{s0}	k	C_1	C_2	σ_{k0}	ε_{k0}	θ
664	4.15	1.38×10^{-23}	1.58×10^6	-0.0106	464	1.54	21609

It is to be noted that the total number of fit parameters of 8 in the V-K model is substantially less than in the Arrhenius model. Figure 5.35 shows a comparison of experimental and simulation based true stress-true strain curves. The predicted stress-strain curves from the use of modified V-K model in the FE-based test simulations match the experimental curves

very well for the entire range of test conditions, and appears clearly superior to the J-C and Arrhenius models. It is to be noted that the experimental compression tests at RT and 100 °C were stopped at a strain of 0.3, but in the modified V-K model, the results were extrapolated to the strain of 0.5.

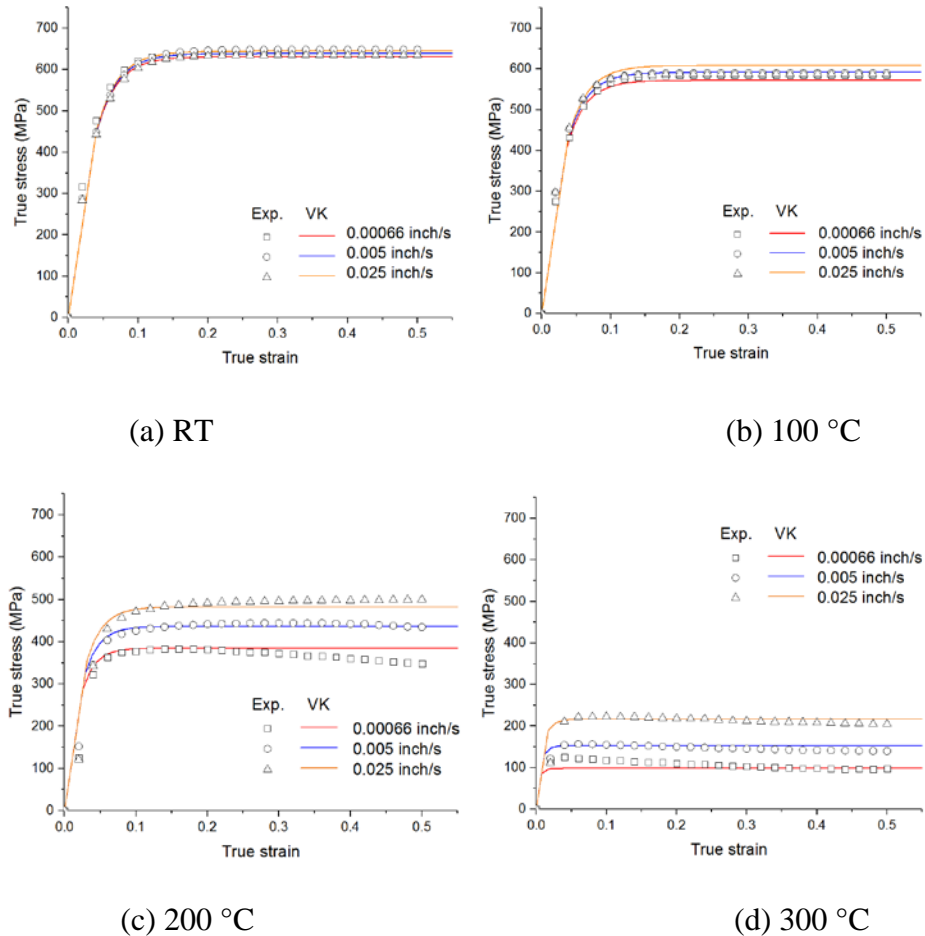
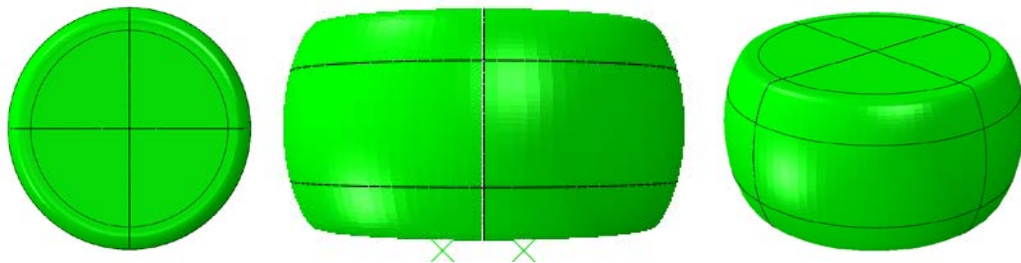


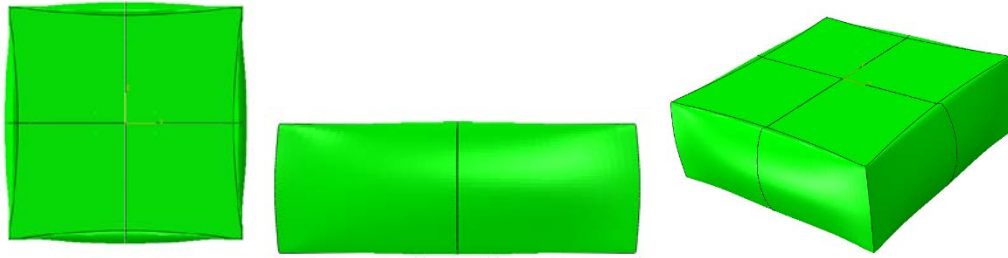
Figure 5.35. Comparison of predicted true stress-strain curves from FE simulation of uniaxial compression tests using modified V-K model and experimentally obtained curves, (a) RT, (b) 100 °C, (c) 200 °C and (d) 300 °C (Temper: T6, orientation: RD, geometry: cylinder).

It is worth noting that, in spite of the good fit to the data by the modified V-K model, it does have one limitation. The model is incapable of capturing the gradual decrease in stress that is observed after yielding at elevated temperatures of 200 °C and 300 °C. The model equations show stress saturation at large strains. In any case, results from the modified V-K model based FE simulations were analyzed for their prediction of material flow behavior and strain localization at large strains. The model was used to simulate both the cylindrical and cubic specimens and the final specimen geometry was compared with those obtained from the experiments. The strains paths associated with the region of strain localization and fracture of the experimental specimens were also extracted from the model simulations. These results are for the isotropic case, they are presented and discussed below.

Figure 5.36 (a, b) shows the typical top, side and isometric views of deformed cylindrical and cubic specimens respectively for compression distances corresponding to half of the initial height of the specimen. As shown, the barrelled specimen shape for cylindrical specimen and a more complex bulge shape of the cubic specimens were correctly predicted by the FE models.



(a) Different views of a compressed cylindrical specimen.



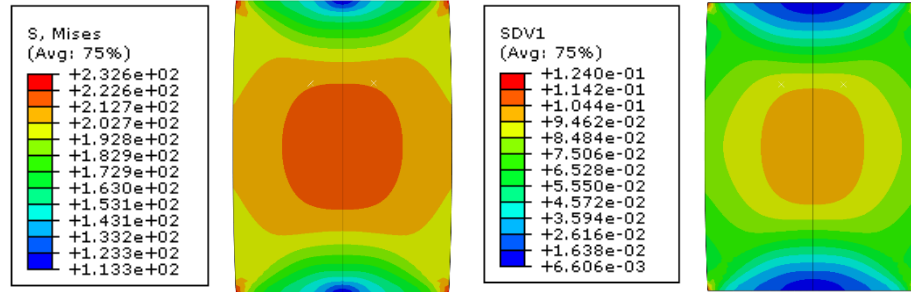
(b) Different views of a compressed cubic specimen.

Figure 5.36. Top, side and isometric views of compressed cylindrical and cubic specimens (compression distance: 7.5 mm for cylindrical specimen and 4.5 mm for cubic specimen, orientation: RD, temper: T6, temperature: 300 °C and test speed: 0.005 inch/s (0.127 mm/s)).

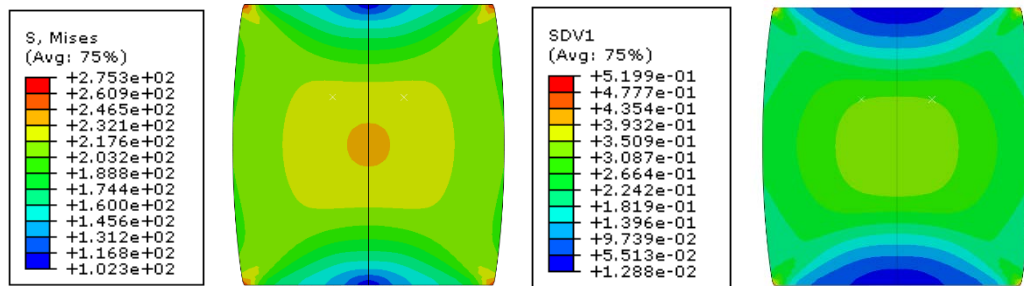
Figures 5.37 shows snapshots of the contours of Mises stress and corresponding equivalent plastic strain (PEEQ) for deforming cylindrical specimen at various compression distances from 1 mm to 7.5 mm. Results similar to cylindrical specimens for cubic specimens for compression distances from 1 mm to 4.5 mm are shown in Figure 5.38. The Mises stress values are typically larger at the top and bottom edges of the cylindrical specimens and their development appears diagonally across a pair of planes (i.e., two intersecting planes along the 45 ° orientation to the loading axis). The equivalent strain contours exhibit a similar trend to the Mises stress contours. While cylindrical and cubic specimens exhibit rather similar Mises stress and equivalent contours, some subtle differences persist in the more constrained corner region for the cubic specimen at large compression distances.

Mises Stress

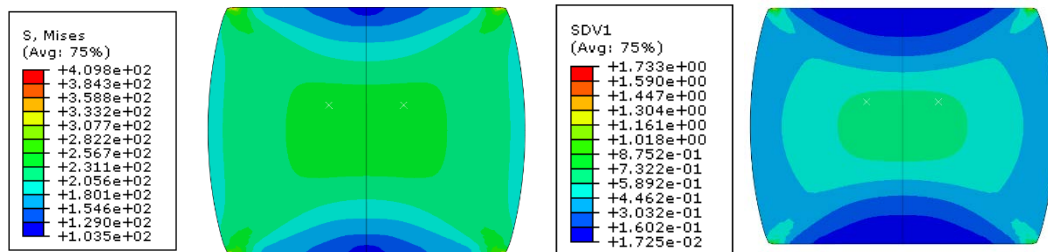
PEEQ



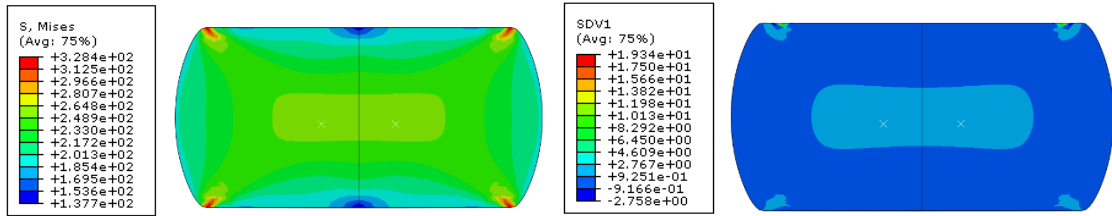
1 mm



3 mm

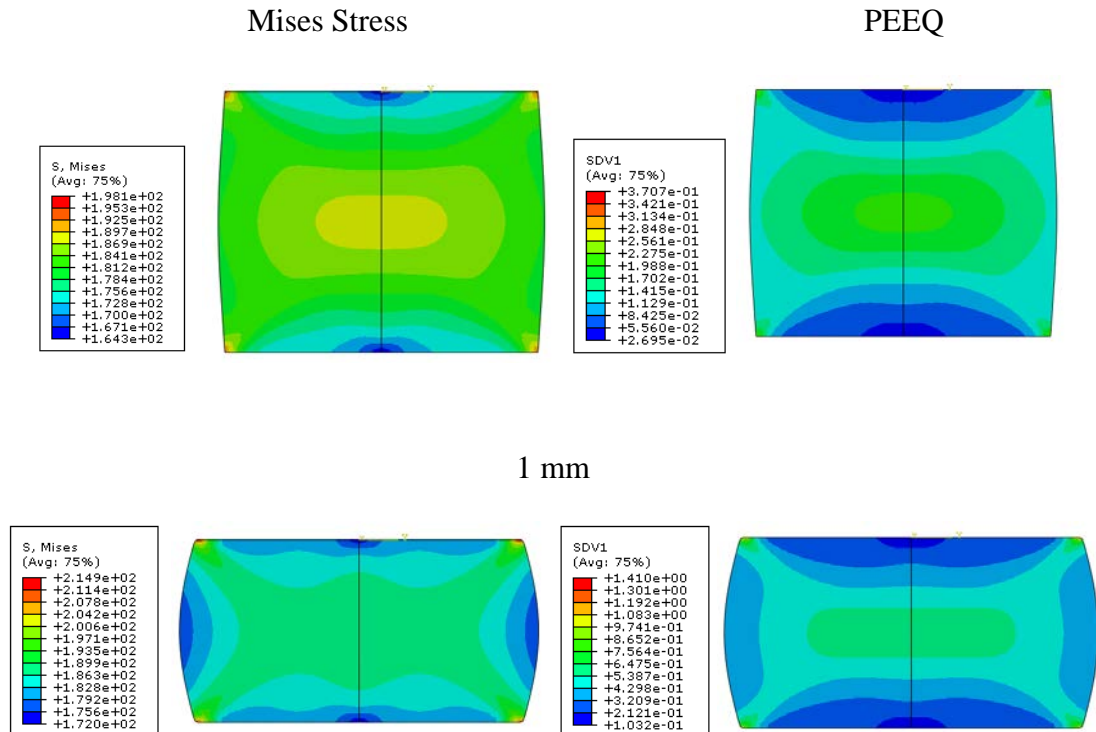


5 mm



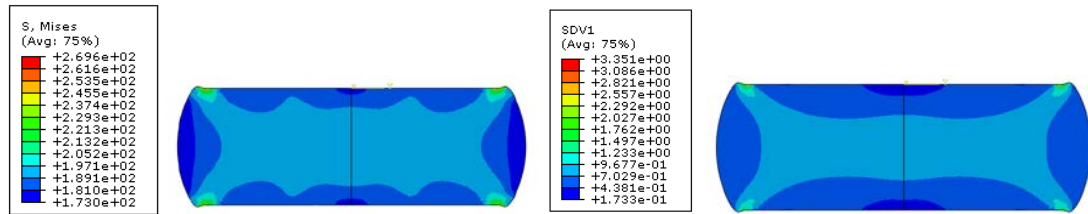
7.5 mm

Figure 5.37. The Mises stress and equivalent plastic strain contours at various compression distances for cylindrical specimens in side view (orientation: RD, temper: T6, temperature: 300 °C and test speed: 0.005 inch/s (0.127mm/s)).



1 mm

3 mm



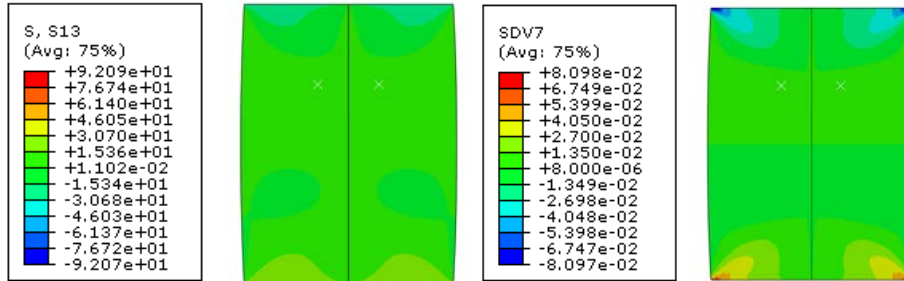
4.5 mm

Figure 5.38. The Mises stress and equivalent plastic strain contours at various compression distances for cubic specimens (orientation: RD, temper: T6, temperature: 300 °C and test speed: 0.005 inch/s (0.127 mm/s)).

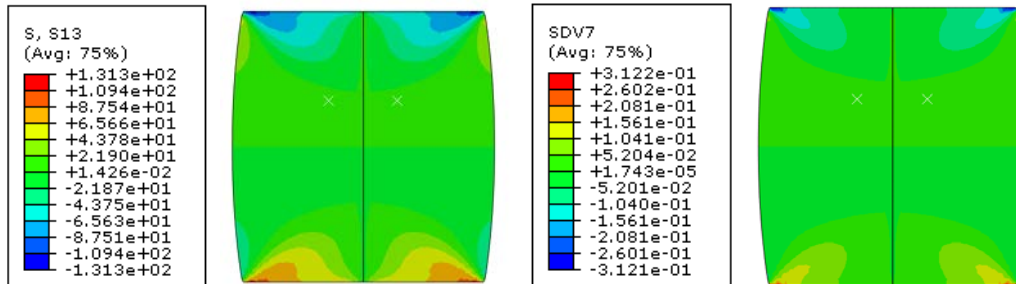
Figures 5.39 and 5.40 show the contours of shear and shear strain components along x-z plane (x and z are horizontal and vertical axes respectively) at various compression distances for cylindrical and cubic specimens respectively. The development of shear stress and strain along the two intersecting planes oriented 45° to the loading is clearly more pronounced than the Mises stress and equivalent strain contours. This result is indeed consistent with the slant failures that have been observed in fractured room temperature test specimens in T6 and O-temper conditions. Thus, the failures in room temperature uniaxial compression tests appear to be driven by the maximum shear stress and strain values.

Shear stress

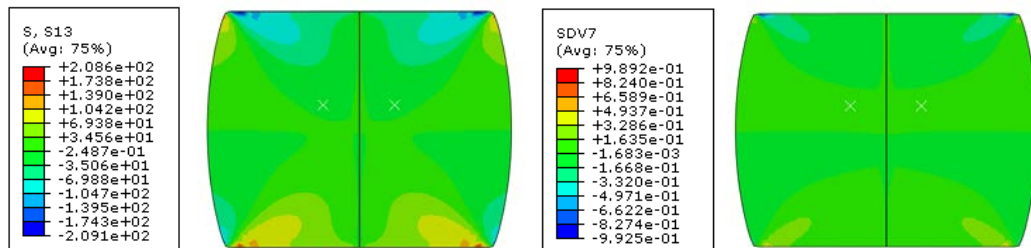
Shear strain



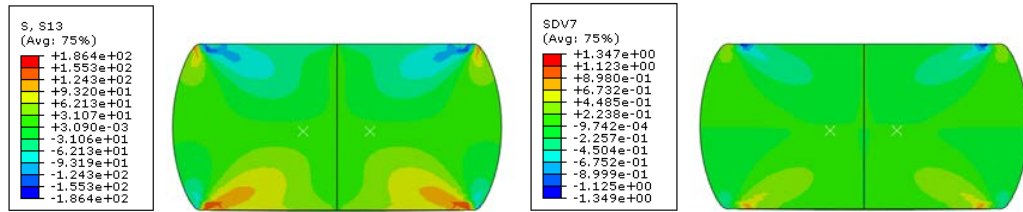
1 mm



3 mm



5 mm

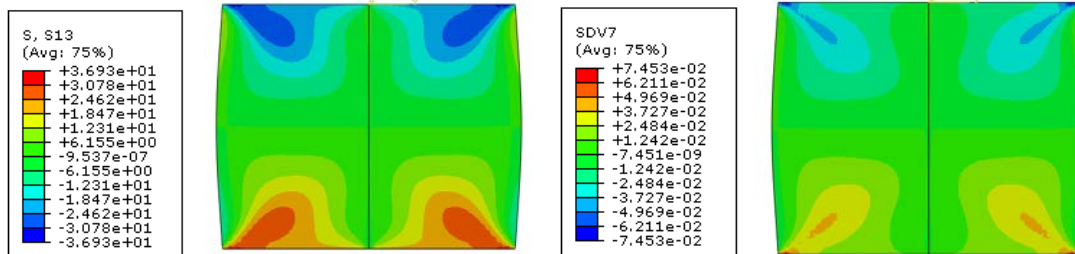


7.5 mm

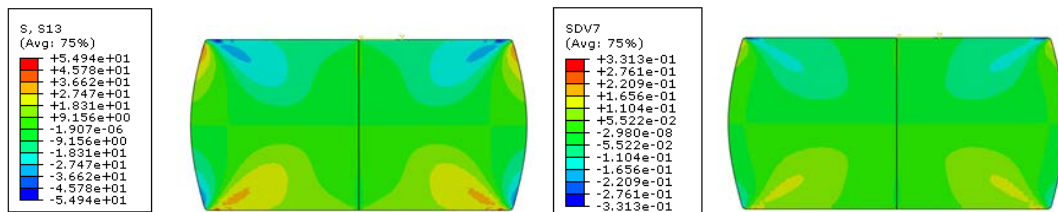
Figure 5.39. Shear stress and shear strain contours at various compression distances for cylindrical specimens (orientation: RD, temper: T6, temperature: 300 °C and test speed: 0.005 inch/s (0.127 mm/s)).

Shear stress

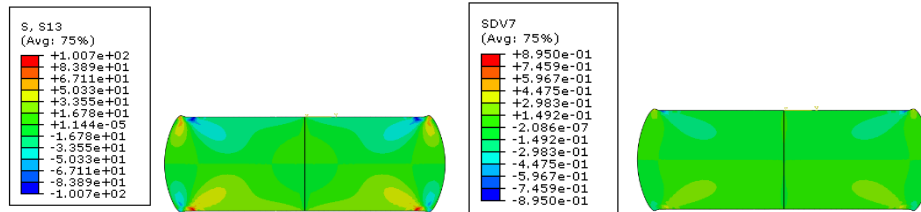
Shear strain



1 mm



3 mm



4.5 mm

Figure 5.40. Shear stress and shear strain contours at various compression distances for cubic (orientation: RD, temper: T6, temperature: 300 °C and test speed: 0.005 inch/s (0.127 mm/s)).

The strain paths from specimen critical locations in the cylindrical and cubic FE models, as described in Figures 5.41 and Figure 5.42 respectively, were extracted from the simulations to analyze the nature of each of the strain paths and their approach towards the limit strain on the tension-compression side of the forming limit diagram (FLD). The strain paths for the cylindrical and cubic specimens are shown in Figures 5.43 and 5.44 respectively. The strain path data suggests that points B and B₂, marked as SPB and SPB₂ in Figures 5.43 and 5.44 respectively, are highly non-linear closest to plane strain path. These paths are likely to approach the conventional forming limit curve (FLC) first compared to the other points within the test specimen. These results point to the plastic strain instability initiation from the outer barrelled surface location at mid-height position of the specimen. However, the strain path appears to be inconsistent with the slant failures observed in the isothermal experiments with cylinders and cubic specimens. The shear-

dominated strain paths such as the one from points C for cylindrical specimen in Figures 5.41 and 5.43, and point C₂ for cubic specimen in Figures 5.42 and 5.44 will likely meet the shear fracture line on the tension-compression side of the FLD space first and cause shear fracture. The strain path results also suggest that the critical strain path for cylindrical and cubic specimens are very similar and failure is unlikely to occur at the corner position in a cubic specimen. This latter FE result is indeed consistent with the observed results.

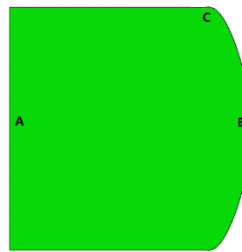
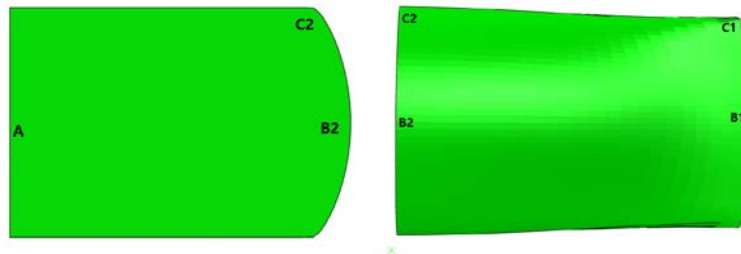


Figure 5.41. FE model geometry (1/4th model) of cylindrical specimen with specific points of interest for strain path determination.



(a) Side view

(b) Top view

Figure 5.42. FE model geometry (1/4th model) of cubic specimen with specific points of interest for strain path determination.

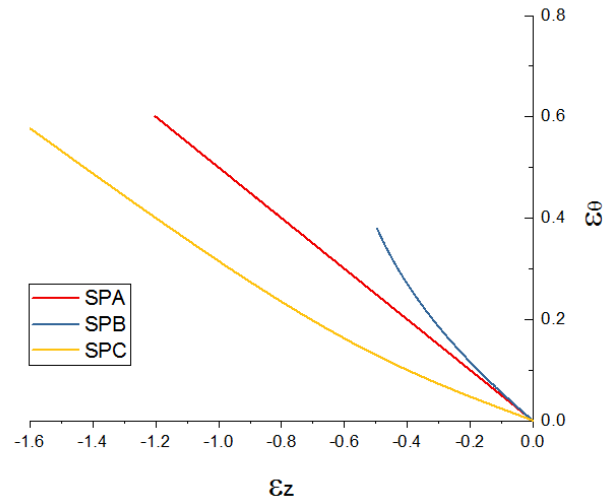


Figure 5.43. The strain paths of elements located at center (A), mid-surface (B) and top edge (C) of a cylindrical specimen.

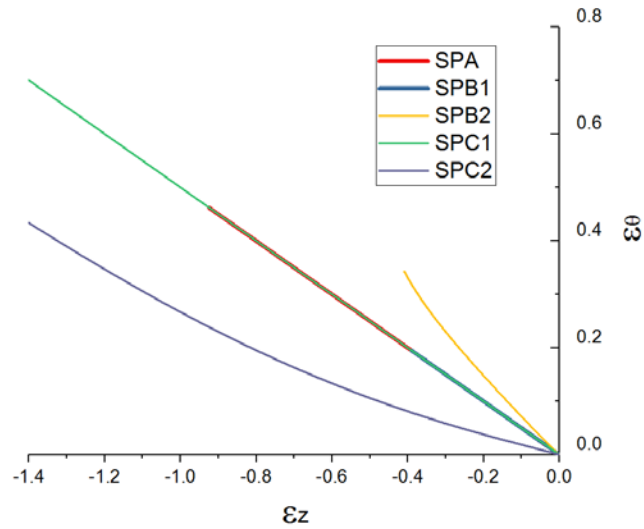


Figure 5.44. The strain paths of elements located at center (A), mid-surface (B₁ and B₂) and corner (C₁ and C₂) of a cubic specimen.

5.4.2. Material anisotropy

The experimental results presented earlier exhibited some anisotropy of flow stress in the T6 temper state, especially at lower temperatures (see Figure 5.7, for example). To capture this effect in the FE simulations, Hill quadratic transverse anisotropic yield criterion (with a single plastic anisotropy parameter r) was used in a few simulations of test samples. The r values for these simulations were obtained from the literature and presented earlier in Chapter 4. Figures 5.45 shows the top views of a cylindrical specimen from simulation and experiments at a deformed specimen height of 12 mm. Both experimental and predicted images exhibit a deformed oval shape of the specimen and similar level of ovality in terms the major and minor diameter of the oval of 10.4 mm and 10.2 mm respectively. Similar results for a cubic specimen are presented in Figure 5.46 where both the top and side views from the simulation and experiments for a specimen height of 7 mm are compared. Once again, the deformed dimensions from the model and experiment are comparable with the experiment giving the cube length of the top and side of 9.87 mm and 10.28 mm respectively and the simulation providing length of the top and side of 9.8 mm and 10.24 mm respectively. A comparison of Mises stress contours for the top surfaces of cylindrical and cubic specimens, however, reveal significant differences arising from the anisotropy of flow. The deformation is confined to a pair of opposite surfaces with minimal deformation of the other pair of surfaces leading to deformation of a square shape into a rectangle and the deformation of the corner region of the cubic specimen is significantly smaller. Therefore, it appears that material anisotropy manifest more extensively for a cubic specimen and less so for a cylindrical specimen.

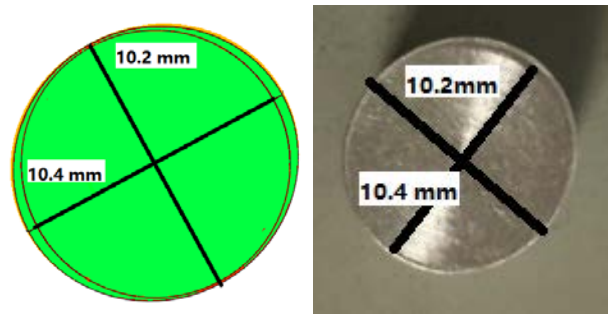
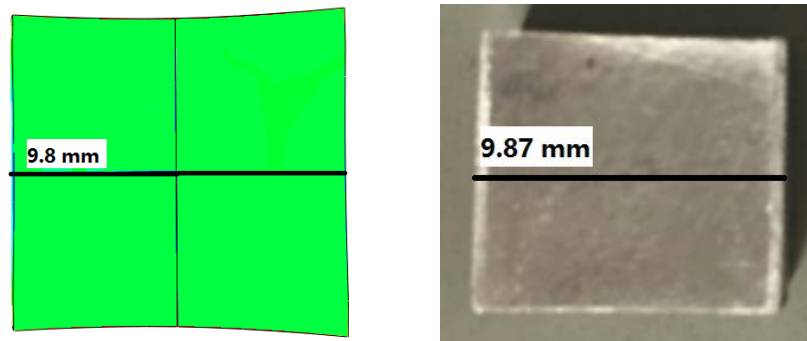
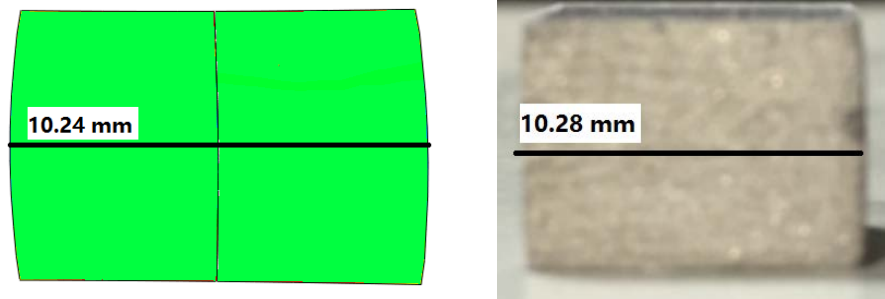


Figure 5.45. A view of the top surface of a deformed cylindrical specimen from simulation (left) and experiments (right) corresponding to the specimen height of 12 mm.

(Temper: T6, temperature: RT, test speed: 0.005 inch/s (0.127 mm/s)).



(a) Top view of cubic specimen.



(b) Side view of cubic specimen.

Figure 5.46. Deformed cubic specimen from simulation and experiment corresponding to a specimen height of 7 mm, (a) top view, and (b) side view (Temper: T6, temperature: room temperature, test speed: 0.005 inch/s (0.127 mm/s)).

5.4.3. Modeling of ductile fracture

FE simulation work as presented above did not attempt to predict the ductile fracture of the experimental test specimens for the different test conditions. However, some effort was devoted towards assessing available ductile fracture models in the literature for their capability to predict the general fracture morphology (shape and orientation) of the fractured test specimens. Due to the complexity of the fracture prediction problem and limited guidance in the literature for the role of temperature in ductile fracture prediction, effort was limited to room temperature uniaxial compression tests only. Two types of well-known ductile fracture models were considered, the first one based on implicit consideration of void initiation, and growth in the constitutive formulation in the form of Gurson-Tvergaard-Neddleman (or GTN) model, and another one based on empirical consideration of fracture in the form of a Tresca fracture criterion. Both of these models

were described in some detail in the Modeling Methodology chapter earlier. Modeling results from these two models are presented below.

5.4.3.1. GTN ductile damage model

For convenience, GTN ductile damage model equations from Chapter 4 are restated below.

$$\Phi = \left(\frac{\sigma_{eq}}{\sigma_y}\right)^2 + 2q_1 f^* \cosh\left(1.5q_2 \frac{\sigma_h}{\sigma_y}\right) - (1 + q_3 f^{*2}) = 0 \quad (5.7)$$

$$\text{where } f^* = \begin{cases} f & f \leq f_c \\ f_c + \frac{1}{q_1} \frac{f - f_c}{f_f - f_c} & f_c \leq f \leq f_f \end{cases} \quad (5.8)$$

For the GTN damage model based FE simulations, the GTN material parameters in the above equations for AA7075-T6 alloy were obtained from a recent paper (Ding et al., 2017).

These are shown below in Table 5.3.

Table 5.3. Parameters of GTN damage model for AA7075 alloy (Ding et al., 2017).

q_1	q_2	q_3	f_n	ε_n	s_n	f_f	f_c
1.5	1	2.25	0.01	0.3	0.1	0.25	0.15

An element deletion feature within ABAQUS FE code to explicitly remove elements from the mesh, upon meeting the damage criterion, was utilized in the simulations. Figure 5.47 presents a FE simulation result using GTN ductile fracture model within ABAQUS for a

cylindrical specimen compressed at room temperature where the colours represent the void volume fraction. In the simulation the compression distance was set to 7.5 mm, half of the original height. This value turned out to be larger than the compression distance to fracture of 3-4 mm in the RT experiments. As shown, multiple fractures initiate at the outer surface of the specimen at the location of maximum circumferential tensile stress with fracture orientations perpendicular to the circumferential tensile stress direction. Such fracture morphological features were indeed observed in the non-isothermal experiments as shown earlier in Figure 5.20 (c). However, room temperature and other isothermal experiments typically revealed a slant fracture planes as shown in Figure 5.48 below and consistent with the direction of flowlines observed on the surface and interior optical micrographs of the test specimen. It is perhaps possible that classical GTN model in its current form in ABAQUS FE code is incapable of predicting shear dominated fracture. This model is often used to predict fracture when the fracture is driven by a large hydrostatic tensile stress component which is highest in the neck region of a uniaxial or biaxial tensile specimen and not along the maximum shear stress planes of a uniaxial compression test specimen.

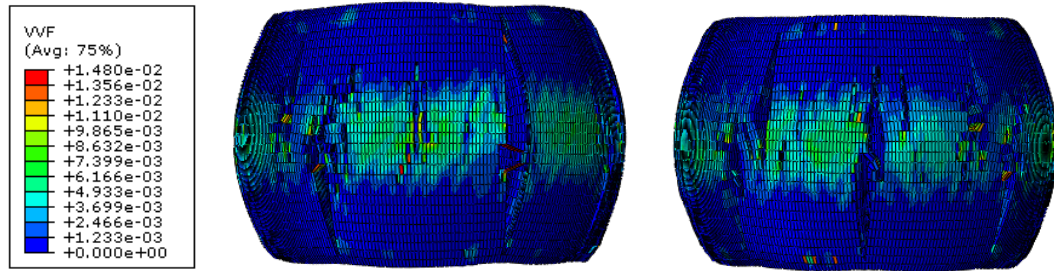


Figure 5.47. Prediction of fracture from GTN damage model for a cylindrical specimen uniaxially compressed at room temperature.



Figure 5.48. The slant failure of a T6 temper cylindrical specimen tested at room temperature.

5.4.3.2 Tresca fracture model

The stress-based Tresca fracture criterion assumes that fracture occurs when τ_{max} reaches a constant value. Based on compression distance data to fracture of about 3-4 mm in RT compression test of a cylindrical specimen, and corresponding to a maximum shear stress is of 372 MPa, a constant for Tresca fracture model of 372 MPa was assumed. The FE simulation result employing Tresca fracture criterion for a cylindrical specimens compressed at room temperature is shown in Figure 5.49 below where the model does

exhibit fracture along a slant orientation which is similar to the slant failure of experimental specimen in Figure 5.48. Thus, Tresca fracture criterion appears to be capable of predicting fracture characteristics of cylindrical test specimen tested in uniaxial compression at room temperature. However, a more dedicated and in-depth effort will be needed to fully assess the potential of Tresca fracture criterion in predicting failure in uniaxial compression under a broader range of experimental conditions and for different specimen geometries.

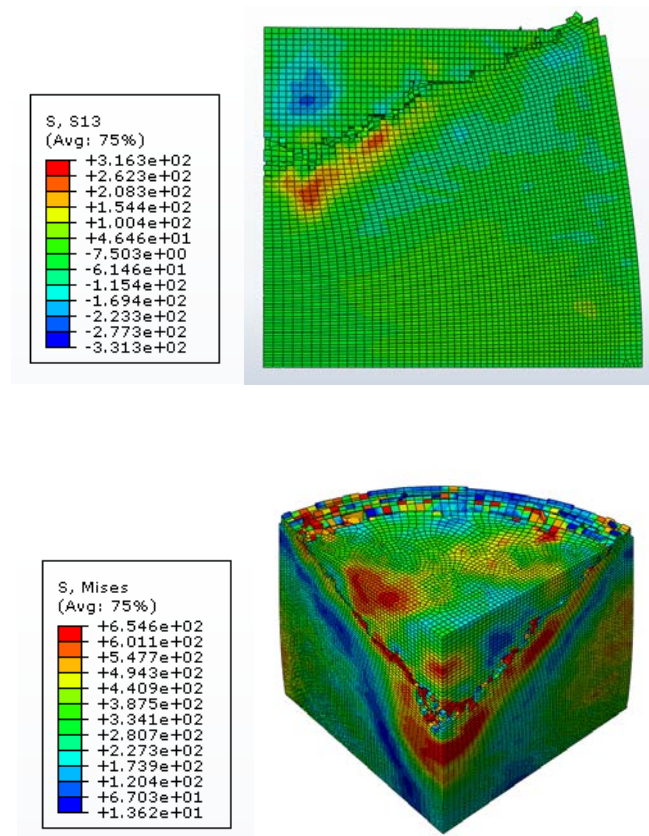


Figure 5.49. Side and isometric views of a 1/8th geometry compressed cylindrical test specimen showing deleted elements along an inclined shear plane from FE simulations with Tresca fracture criterion.

5.5. Summary

This chapter presented a large body of experimental and numerical results pertaining to isothermal room and elevated temperature uniaxial compression of AA7075 cylindrical and cubic specimens tested in T6 and O tempers and RD and TD orientations. The experimental investigation consisted of uniaxial compression tests to obtain true stress- true strain curves at different speeds as well as surface and interior, microscopic, observations of surface and interior flowlines and changes in the grain morphology under different test conditions. The isothermal uniaxial compression experiments were combined with FE simulations of compression experiments based on modified Voce-Kocks model. The model was implemented as a UMAT sub-routine in ABAQUS and useful complementary information and understanding was sought from the experimental and computational approaches. A rather novel non-isothermal (i.e., transient) hot compression experiments was also performed using a high current electrical resistance heating system and the experimental trends with regard to material flow behavior under isothermal and non-isothermal conditions were compared.

There have been very few experiments on hot uniaxial compressions experiments on cubic specimens, and none to our knowledge on AA7075 alloy, so some of the results are quite new and useful. For example, the corner region of the cube does not undergo large deformation and significantly constrains the flow of the material. Also, the effect of material anisotropy is significantly lower at elevated temperatures of about 200 °C and higher. Deformed grain morphological features are quite different in hot compression

specimens tested at elevated temperatures in RD and TD directions to large strains. This may have ramification in the fracture characteristics of specimens deformed in the two different orientations at elevated temperature.

Voce-Kocks model has been identified as a suitable model for representing the compressive flow behavior of AA7075-T6 alloy at a range of temperatures and strain rates. Good success was achieved in the prediction of experimental deformed shapes of cylindrical and cubic specimens and material flow behavior from the isotropic and anisotropic Hill criterion based FE models. Reasonable success was achieved in slant failure prediction at room temperature based on Tresca fracture criterion which is essentially a maximum shear stress criterion. It was learned that the strain path analysis approach coupled with a conventional forming limit diagram region is unlikely to help predict the onset of shear-type plastic instability or shear fracture. However, the shear fracture line that meets the shear strain paths in the tension-compression region of the FLD may be a good predictor of plastic instability and shear fracture. The non-isothermal tests revealed that good bulk formability equivalent to isothermal conditions is possible with rapid resistance heating minimizing cost and increasing manufacturing efficiency hot upsetting and hot forging applications of possibly small hard-to-form components.

In terms of limitations of the present work, the original plan of work was to utilize Aramis on-line strain measurement system to obtain strain field data from the test specimens at room and elevated temperatures. Although room temperature tests were successfully

completed, all data was lost due to a major computer crash. On-line strain field measurement at elevated temperature through a small observation window of the environmental chamber turned out to be too challenging and unreliable due to image quality issues. Such a data would have provided a useful additional avenue for FE model validation and for better understanding of the strain localization process at large strains in hot uniaxial compression. Clearly, the modeling of ductile fracture at elevated temperature was outside the scope of the work as well as the FE modeling of the non-isothermal electric resistance heating based uniaxial compression experiments.

Chapter 6. Conclusions

Uniaxial compressive deformation of AA7075-T6 and O-temper materials at room and elevated temperatures was studied by conducting lab-based experiments and corresponding FE simulations. The following conclusions were drawn from the study.

[1]. From isothermal compression experiments on cylindrical specimens, T6 temper material exhibited strain hardening at room temperature and 100 °C but stress saturation and softening at 200 °C and 300 °C, in the test speed range of 0.0167 mm/s-0.635 mm/s. The general trends in stress-strain curves for cubic specimens were similar to the cylindrical specimens under the above test conditions.

[2]. The O-temper material stress-strain curves were similar to the T6 temper material under the above test conditions but no strain softening was observed at higher temperatures. The results can be explained on the basis of dynamic recovery and dynamic recrystallization mechanisms that are observed in T6 temper material and their absence in the O-temper material, as reported in the literature.

[3]. From isothermal compression experiments on cylindrical and cubic specimens, T6 temper material exhibited largest strain rate hardening at 200 °C in the test speed range of 0.0167 mm/s-0.635 mm/s. The results are consistent with variation in strain rate sensitivity with temperature reported in the literature.

[4]. From isothermal compression experiments on cylindrical and cubic specimens, T6 temper material exhibited anisotropy of true stress – true strain curves at room temperature and 100 °C, with tests in TD direction yielding slightly higher flow stress curves in the test speed range of 0.0167 mm/s-0.635 mm/s. The anisotropy of flow stress was absent at 200 °C and 300 °C. The anisotropy of flow stress at lower temperatures was attributed to different grain structure and crystallographic texture and slip systems available in RD and TD orientations.

[5]. From isothermal compression experiments on cylindrical and cubic specimens, the latter geometry exhibited slightly higher flow stress curves. This was attributed to the presence of corners in the cubic specimen, which tended to constrain the flow of the material. Consequently, the cubic specimen geometry also led to a more complex curvature in the deformed specimens compared to the cylindrical geometry.

[6]. From isothermal compression experiments, a characteristic smooth curvilinear pattern of flowlines was observed on the surface and in the interior of the isothermally deformed cylindrical and cubic compression specimens at a range of test conditions. The flowlines, observed with optical microscope in the interior of the test specimen, corresponded with the changes in the grain morphology caused predominantly by shear-type deformation of the grains. The fracture characteristics of room temperature test specimens coincided with the shape of the flowlines.

[7]. Non-isothermal hot compression tests on cylindrical and cubic specimens utilizing an electrical resistance heating system that yielded flow curves very similar to those from isothermal tests at lower applied currents, and thus lower peak temperatures at the symmetric core of the test specimens. However, at higher applied current, a large thermal gradient occurred between the specimen core and the outer periphery which led to the formation of longitudinal cracks (perpendicular to the circumferential stress direction). So, the magnitude of applied current and part size may be important in electrical resistance heating based hot deformation process to minimize the thermal gradient and avoid failure.

[8]. Non-isothermal hot compression technology by employing rapid electrical resistance heating method appears cost-effective (short cycle time) and higher surface quality for forming smaller-scale components from AA7075-T6 alloy via hot upsetting and forging processes.

[9]. Voce-Kocks strain rate and temperature dependent constitutive hardening model was found to represent the isothermal true stress-true strain curves of AA7075-T6 alloy accurately in the range of test temperatures, strain rates and applied strains. The extrapolations to larger strains from the model fit parameters were also found to be reasonable. On the other hand, two other constitutive material models, Johnson-Cook and Arrhenius-type, were unable to represent the isothermal true stress-true strain curves of AA7075-T6 alloy accurately over the range of test temperatures, strain rates and applied strains.

[10]. Voce-Kocks model, on implementation into ABAQUS FE simulation code, yielded good agreement between the experimental and simulated cylindrical and cubic deformed specimen geometries.

[11]. FE simulations of compression experiments with cylindrical and cubic specimen geometries revealed presence of large shear stress, and corresponding shear strain, components along two intersecting diagonal planes within the specimen. These results were consistent with the pattern of grain morphological changes observed using optical microscopy.

[12]. FE simulations of compression experiments with cylindrical and cubic specimen geometries revealed two different strain paths in the tension-compression strain space used to represent bulk formability of the material. A non-linear strain path was observed from a point on the outer barrelled surface which becomes the site of the maximum circumferential tensile stress. This strain path moved towards the conventional tension-compression FLC curve. Additionally, a linear strain path from the top and bottom edge regions of cylindrical and cubic specimens was observed. This path was located well below the conventional tension-compression FLC curve. It is concluded that the linear path corresponds to pure shear mode of deformation in the two diagonal planes within the cylindrical and cubic specimens. This strain path is responsible for the observed shear failure of the specimens in uniaxial compression of AA7075-T6 sheet.

[13]. Tresca fracture criterion, on implementation into ABAQUS FE code, and by employing an element deletion criterion, was found to capture the slant (diagonal) fracture characteristics of cylindrical compression test specimens. On the other hand, the well-known Gurson-Tvergaard-Needleman (GTN) ductile fracture criterion was unable to capture the slant (diagonal) fracture characteristics. The GTN model based fracture prediction corresponded to the highest circumferential stress and strain region on the outer barrelled surface. This limitation of the GTN model for cylindrical compression fracture shape prediction was attributed to its strong dependence on hydrostatic tension component that is often present in tensile necking of bars and under sheet forming conditions. The hydrostatic tension component is not expected to be dominant in the uniaxial compression mode.

Chapter 7. Suggestions for Future Work

[1]. Uniaxial compression experiments in the present study did not involve any full-field strain measurements from the outer surface of the deformed compression specimens. This very useful experimental technique should be utilized in the future experiments to develop a more comprehensive understanding of the deformation and strain localization processes in uniaxial compression. The pattern formation of flowlines observed on the surface and strain associated with them could be potentially captured with on-line speckle-based, to-camera, digital image correlation (DIC) system. Its use with the elevated temperature tests, if possible, would be especially useful in determining the local limit strains at failure at different temperatures. Also, the full-field strain measurement will offer another means of validating the FE models of compressed cylinders and cubes, and to characterize the strain state of the corner regions versus the sides of the cubes.

[2]. In the present work, only a few specimens were taken to fracture. In fact, all fractured specimens were tested at room temperature. It would be useful to study the fracture characteristics of elevated temperature specimens to determine if the fracture mode is temperature dependent.

[3]. Non-isothermal compression tests are new area of research that was initiated in the present work. However, the knowledge base so far is very limited. A wider range of experiments should be conducted in the laboratory to explore the potential of this type of transient temperature deformation for some real industrial applications such as hot

upsetting. Also, the transient temperature field within the specimen arising from rapid electrical resistance heating should be better characterized, perhaps using multiple thermocouples at different locations within the specimen and/or via a reliable infrared temperature sensor system to obtain temperature field measurements over the cylindrical surface. This will help develop a suitable thermo-mechanical model of the heating and subsequent large strain compression of the cylindrical and cubic specimens, to further expand on the current understanding. Also, fracture prediction under non-isothermal conditions, such as the one observed at higher applied current, would be an interesting area of research.

[4]. In the present work, the fracture criterion such as Tresca has been applied to room temperature compression tests on cylindrical specimens only. Its use to predict elevated temperature fracture modes will be a useful future investigation. Also, Tresca fracture criterion should be assessed for fracture prediction of cubic specimens at room and elevated temperatures.

[5]. The FE model developed in the present work did not utilize the friction coefficient from a separate experimental study. Appropriate, but rather arbitrary, values were chosen from the data reported in the literature for friction at room and elevated temperatures. This should be corrected by performing separate room and elevated temperature friction tests. Also, the experiments indirectly revealed that the frictional conditions at the top and bottom platens were not always identical leading to perhaps un-symmetric loading of the specimen in some

cases. Therefore, more attention should be paid to ensuring identical surface conditions and cleaning of the platens and standardized lubrication of the platens prior to each test.

[6]. In the present work, substantial effort was made to arrive at a suitable constitutive hardening law for AA7075-T6 alloy. The strain rate and temperature dependent hardening law of Voce-Kocks yielded good results in the present work but was still unable to capture strain softening at elevated temperatures. Therefore, there is an opportunity to explore other more suitable strain rate and temperature dependent hardening laws for representing the behavior of AA7075-T6 alloy at a larger range of strain rates, temperatures and strains. In choosing or developing a new hardening law it is important to strive for fewer fitted material parameters to achieve a broader range of experimental conditions. However, this is not always possible considering that AA7075 alloys is a complex precipitation hardenable alloy with many deformation mechanisms that operate at elevated temperatures.

References

Bai, Y., Wierzbicki, T., (2008). "A new model of metal plasticity and fracture with pressure and Lode dependence." International journal of plasticity **24**(6): 1071-1096.

Bao, Y., Wierzbicki, T., (2004). "A comparative study on various ductile crack formation criteria." Transactions-american society of mechanical engineers journal of engineering materials and technology **126**: 314-324.

Bao, Y., Wierzbicki, T., (2004). "On fracture locus in the equivalent strain and stress triaxiality space." International Journal of Mechanical Sciences **46**(1): 81-98.

Brar, N., Josh, V., Harris, B., (2009). "Constitutive Model Constants for Al7075-t651 and Al7075-t6". Aip conference proceedings, AIP.

Chen, K., Liu, H., Zhang, Z., Li, S., Todd, R., (2003). "The improvement of constituent dissolution and mechanical properties of 7055 aluminum alloy by stepped heat treatments." Journal of Materials Processing Technology **142**(1): 190-196.

Chen, S., Chen, K., Peng, G., Chen, X., Ceng, Q., (2012). "Effect of heat treatment on hot deformation behavior and microstructure evolution of 7085 aluminum alloy." Journal of Alloys and Compounds **537**: 338-345.

Deng, Y., Yin, Z., Huang, J., (2011). "Hot deformation behavior and microstructural evolution of homogenized 7050 aluminum alloy during compression at elevated temperature." Materials Science and Engineering: A **528**(3): 1780-1786.

Ding, H., Zhu, C., Song, C., Qian, D., (2017). "Effect of the quenching residual stress on ductile fracture behavior of pre-stretched aluminum alloy plates." Journal of the Brazilian Society of Mechanical Sciences and Engineering **39**(6): 2259-2267.

Gao, X., Kim, J., (2006). "*Modeling of ductile fracture: significance of void coalescence.*" International Journal of Solids and Structures **43**(20): 6277-6293.

Hall, I., Guden, M., (2003). "*Split Hopkinson Pressure Bar compression testing of an aluminum alloy: Effect of lubricant type.*" Journal of materials science letters **22**(21): 1533-1535.

<http://nptel.ac.in/courses/112107146/12>.

https://en.wikipedia.org/wiki/7075_aluminium_alloy#cite_note-4.

Hu, P., Ma, N., Liu, L., Zhu, Y., (2012). *Theories, methods and numerical technology of sheet metal cold and hot forming: Analysis, simulation and engineering applications*, Springer Science & Business Media.

Jain, M., Allin, J., Lloyd, D., (1999). "*Fracture limit prediction using ductile fracture criteria for forming of an automotive aluminum sheet.*" International Journal of Mechanical Sciences **41**(10): 1273-1288.

Jenab, A., Taheri A., (2014). "*Experimental investigation of the hot deformation behavior of AA7075: Development and comparison of flow localization parameter and dynamic material model processing maps.*" International Journal of Mechanical Sciences **78**: 97-105.

Jiang, F., Zhang, H., Su, J., Sun, Y., (2015). "*Constitutive characteristics and microstructure evolution of 7150 aluminum alloy during isothermal and non-isothermal multistage hot compression.*" Materials Science and Engineering: A **636**: 459-469.

Jin, N., Zhang, H., Han, Y., Wu, W., Chen, J., (2009). "*Hot deformation behavior of 7150 aluminum alloy during compression at elevated temperature.*" Materials Characterization **60**(6): 530-536.

Khan, A. S., Baig, M., (2011). "*Anisotropic responses, constitutive modeling and the effects of strain-rate and temperature on the formability of an aluminum alloy.*" International journal of plasticity **27**(4): 522-538.

Kitamura, K., Terano, M., (2014). "*Determination of local properties of plastic anisotropy in thick plate by small-cube compression test for precise simulation of plate forging.*" CIRP Annals-Manufacturing Technology **63**(1): 293-296.

Kobayashi, S., (1970). "*Deformation characteristics and ductile fracture of 1040 steel in simple upsetting of solid cylinders and rings.*" Journal of Engineering for Industry **92**(2): 391-398.

Kocks, U., (1976). "*Laws for work-hardening and low-temperature creep.*" Journal of engineering materials and technology **98**(1): 76-85.

Lee, W., Sue, W., Lin, C., Wu, C., (2000). "*The strain rate and temperature dependence of the dynamic impact properties of 7075 aluminum alloy.*" Journal of Materials Processing Technology **100**(1): 116-122.

Li, H., Fu, M., Lu, J., Yang, H., (2011). "*Ductile fracture: experiments and computations.*" International journal of plasticity **27**(2): 147-180.

Li, P., Siviour, C., Petrinic, N., (2009). "*The effect of strain rate, specimen geometry and lubrication on responses of aluminium AA2024 in uniaxial compression experiments.*" Experimental Mechanics **49**(4): 587-593.

Lin, Y., Chen, M., Zhong, J., (2008). "*Effect of temperature and strain rate on the compressive deformation behavior of 42CrMo steel.*" Journal of Materials Processing Technology **205**(1): 308-315.

Lin, Y., Xia, Y., Chen, X., Chen, M., (2010). "*Constitutive descriptions for hot compressed 2124-T851 aluminum alloy over a wide range of temperature and strain rate.*" Computational Materials Science **50**(1): 227-233.

May, J., Hoppel, H., Goken, M., (2005). "*Strain rate sensitivity of ultrafine-grained aluminium processed by severe plastic deformation.*" Scripta Materialia **53**(2): 189-194.

Naser, T., Krallics, G., (2014). "*Mechanical behavior of multiple-forged Al 7075 aluminum alloy.*" Acta Polytech. Hung **11**: 103.

Park, J., Ardell, A., (1983). "*Microstructures of the commercial 7075 Al alloy in the T651 and T7 tempers.*" Metallurgical and Materials Transactions A **14**(10): 1957-1965.

Paul, A., Ramamurty U., (2000). "*Strain rate sensitivity of a closed-cell aluminum foam.*" Materials Science and Engineering: A **281**(1): 1-7.

Pedersen, K. O., Borvik, T., Hopperstad, O., (2011). "*Fracture mechanisms of aluminium alloy AA7075-T651 under various loading conditions.*" Materials & Design **32**(1): 97-107.

Rokni, M., et al. (2011). "*An investigation into the hot deformation characteristics of 7075 aluminum alloy.*" Materials & Design **32**(4): 2339-2344.

Rokni, M., Zeri-Hanzaki, A., Roostaei, A., Abedi, H., (2011). "*Constitutive base analysis of a 7075 aluminum alloy during hot compression testing.*" Materials & Design **32**(10): 4955-4960.

Sciammarella, C., Considine, J., Gloeckner, P., (2016). "*Erratum: Experimental and Applied Mechanics, Volume 4.*" Experimental and Applied Mechanics, Volume 4, Springer: E1-E1.

Smerd, R., (2005). "*Constitutive behavior of aluminum alloy sheet at high strain rates.*" University of Waterloo.

Sofuoglu, H., Rasty, J., (1999). "*On the measurement of friction coefficient utilizing the ring compression test.*" Tribology International **32**(6): 327-335.

Thomason, P., (1990). "*Ductile fracture of metals.*" Pergamon Press plc, Ductile Fracture of Metals(UK), 1990: 219.

Wang, H., Luo, Y., Friedman, P., Chen, M., Gao, L., (2012). "*Warm forming behavior of high strength aluminum alloy AA7075.*" Transactions of Nonferrous Metals Society of China **22**(1): 1-7.

Wang, M., Wang, W., Zhou, J., Dong, X., Jia, Y., (2012). "*Strain effects on microstructure behavior of 7050-H112 aluminum alloy during hot compression.*" Journal of Materials Science **47**(7): 3131-3139.

Wang, X., Li, H., Chandrashekhara, K., Rummel, S., Lekakh, S., Van Aken, D., O'Malley, R., (2017). "*Inverse finite element modeling of the barreling effect on experimental stress-strain curve for high temperature steel compression test.*" Journal of Materials Processing Technology **243**(Supplement C): 465-473.

Zhang, H., Li L., Yuan, D., Peng, D., (2007). "*Hot deformation behavior of the new Al–Mg–Si–Cu aluminum alloy during compression at elevated temperatures.*" Materials Characterization **58**(2): 168-173.